A Comprehensive Investigation of the Influence of Vacuum Conditions on the Drying Characteristics of Textiles

by

Amir Naderian Jahromi

A Dissertation Submitted to the
Graduate School of Sciences and Engineering
in Partial Fulfillment of the Requirements for
the Degree of

Master of Science

in

Mechanical Engineering

KOÇ ÜNİVERSİTESİ

December 1, 2023

A Comprehensive Investigation of the Influence of Vacuum Conditions on the Drying Characteristics of Textiles

Koç University
Graduate School of Sciences and Engineering
This is to certify that I have examined this copy of a master's thesis by

Amir Naderian Jahromi

and have found that it is complete and satisfactory in all respects,
and that any and all revisions required by the final
examining committee have been made.

Committee Members:

Prof. Ismail Lazoglu (Advisor)

Prof. Metin Muradoğlu

Prof. Seyhan Onbaşıoğlu

Date:

ABSTRACT

A Comprehensive Investigation of the Influence of Vacuum Conditions on the Drying Characteristics of Textiles
Amir Naderian Jahromi
Master of Science in Mechanical Engineering
December 1, 2023

Pulsed vacuum drying (PVD) is a novel drying technique that has gained attention in recent years. It is one of the techniques that has emerged to address the limitations of conventional drying methods. This study proposes a comprehensive investigation into the influence of vacuum conditions on the textile drying process. The research focuses on the utilization of both centrifugal vacuum pumps and pneumatic vacuum generators to create a controlled vacuum environment within a custom-designed vacuum drum. It also aims to examine the influence of PVD on textile drying characteristics. This is achieved through a series of steps: first, a thorough analysis of the impact of the constant vacuum and pulsed vacuum process on the drying kinetics of textiles in a vacuum environment; second, identification and evaluation of optimal drying parameters, such as temperature, duration of the vacuum phase, and period of the atmospheric phase; and finally, development of a practical framework for simulating thermal and mass transfer during vacuum-assisted drying. The accuracy of the simulations is confirmed through experimental results.

The comparative study extends to conventional dryers, with the aim of demonstrating the advantages and limitations of vacuum-assisted drying in terms of drying rate and total drying time. Through this investigation, the thesis aims to contribute valuable insights into the potential advancements in textile drying technology, with a focus on vacuum-assisted methods.

ÖZETÇE

Yüksek Lisans Tez Başlığı
Amir Naderian Jahromi
Makine Mühendisliği, Yüksek Lisans
1 Aralık 2023

Pulsed vacuum drying (PVD), son yıllarda dikkat çeken yeni bir kurulama tekniğidir. Bu, geleneksel kurulama yöntemlerinin sınırlarını aşmak amacıyla ortaya çıkan tekniklerden biridir. Bu çalışma, vakum koşullarının tekstil kurulama sürecine olan etkisi üzerine kapsamlı bir araştırma önermektedir. Araştırma, özel tasarlanmış bir vakum tamburu içinde kontrol edilebilir bir vakum ortamı oluşturmak için hem santrifüj vakum pompalarının hem de pnömatik vakum jeneratörlerinin kullanımına odaklanmaktadır. Ayrıca, PVD'nin tekstil kurulama özellikleri üzerindeki etkisini incelemeyi amaçlamaktadır.

Bu, bir dizi adımda başarıya ulaşılacaktır: İlk olarak, PVD sürecinin tekstillerin vakum ortamında kuruma kinetiği üzerindeki etkisinin detaylı bir analizi; ikinci olarak, sıcaklık, vakum aşamasının süresi ve atmosfer aşamasının süresi gibi optimal kurulama parametrelerinin belirlenmesi ve değerlendirilmesi; ve son olarak, PVD süreçlerinde termal ve kütle transferini simüle etmek için pratik bir çerçevenin geliştirilmesi. Simülasyonların doğruluğu deneysel sonuçlar aracılığıyla onaylanmıştır. Karşılaştırmalı çalışma, kurulama hızı ve toplam kurulama süresi açısından vakum destekli kurulamanın avantajlarını ve sınırlamalarını göstermeyi amaçlayarak geleneksel kurutuculara kadar uzanacaktır. Bu araştırma, tezin vakum destekli yöntemlere odaklanarak tekstil kurulama teknolojisindeki potansiyel ilerlemelere değerli görüşler katmayı amaçlamaktadır.

ACKNOWLEDGMENTS

I would like to express my gratitude to my advisor, Prof. Dr. Ismail Lazoğlu, for giving me the chance to work at the well-established laboratory of the University of Koç, the Manufacturing and Automation Research Center (MARC). This thesis would not have been possible without his guidance, advice and support.

I am also very grateful to the Cleaning & Textile Technologies Department of Arçelik A.Ş Central R&D for starting this project and giving me the opportunity to work in their research laboratory. I am thankful to Ömer Ensar Durmuş, Meryem Atila, Onur Ercan,and Songül Bayraktar for their technical and instrumental support. I would also appreciate Koç University and Arçelik A.Ş. for funding the research project.

I would sincerely thank my family for supporting and giving me courage during my master's studies. I am grateful to my wife for her patience and support during difficult times. I am also very thankful to the MARC members and my friends, especially Hamed Rahmatavar, Samaneh Arman, Omer Subasi, Hammad Ur Rahman, Pooya Pashak, and Munam Arshad.

TABLE OF CONTENTS

LIST OF TABLES

LIST OF FIGURES

Chapter 1

INTRODUCTION

Every production and laundry operation is faced with the challenge of moisture at some time. The causes of moisture can vary greatly, and the effects of moisture are also extremely varied. However, the treatment is always drying, which seeks to eliminate as much moisture as possible.

Drying is a process involving the removal of moisture or water content from a substance, either in the form of a solid or a liquid. The purpose of drying can vary widely depending on the material being dried and the desired final result. This method is employed to preserve, transform, or enhance materials by reducing their water content, thereby extending life, reducing weight and volume, and achieving specific material conditions, textures, or concentrations [4, 5, 6, 7].

In the modern context, drying finds widespread applications across various industries. In the food industry, it is crucial to preserve fruits, vegetables, and meats, prevent microbial growth, and extend product shelf life. In pharmaceuticals, drying is employed to produce powdered medications, ensuring stability and ease of storage. Additionally, drying plays a pivotal role in materials processing, such as the production of chemicals and ceramics, where removing water is essential for maintaining product quality and characteristics [8, 9, 10].

In residential settings, drying is commonly employed in the context of laundry. Homeowners use clothes dryers to remove moisture from freshly washed clothes, allowing for quick and convenient drying. This application not only saves time but also ensures that clothes remain free from mold and mildew that can develop in damp conditions. The use of drying in homes contributes to maintaining hygiene and comfort, providing a practical solution for individuals and families in their daily lives.

Correspondingly to drying applications, drying methods include a spectrum from industrial applications to everyday residential practices, each developed to meet specific needs. In industries, advanced techniques such as freeze drying, spray drying, and drum drying are employed for precision in removing moisture from various materials [11, 12]. On the residential front, the most common method is the use of electric or gas-powered clothes dryers, providing a convenient and rapid solution for drying laundry. The diversity in drying methods reflects a balance between technological sophistication in industries and practical simplicity in everyday homes. Figure 1.1 summarizes different techniques of moisture removal. Drying methods are classified as either thermal or mechanical. Particular emphasis is placed on convective methods that have heat sources since these are the most common.

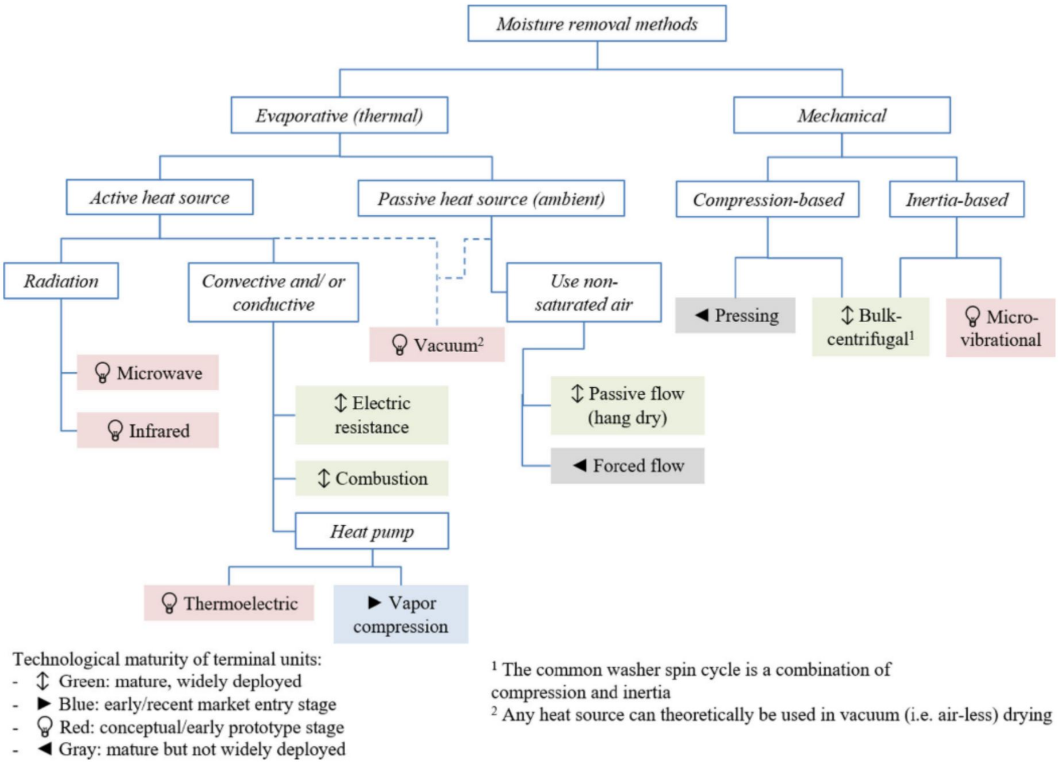

Figure 1.1: Moisture removal different techniques [1].

1.1 The Problem Definition

Cloth drying poses a set of unique challenges, with uniform drying standing out as a key consideration. Ensuring that clothes dry uniformly is critical to prevent damp spots or uneven textures that may compromise the fabric's integrity and comfort. Achieving uniformity is particularly challenging in larger loads, where certain sections of the laundry may dry more quickly than others. Efficient air circulation and the careful arrangement of garments become essential strategies to address this challenge, contributing to a satisfying outcome where every piece emerges consistently dry. Drying time is another pivotal factor in the realm of cloth drying challenges. Balancing the need for a quick turnaround with the desire to maintain fabric quality demands a careful approach. Rapid drying can sometimes subject clothes to higher temperatures, potentially affecting their longevity and texture. Conversely, extended drying times may lead to energy inefficiency and increased operational costs. Striking the right balance involves leveraging advanced drying technologies that offer faster drying cycles while incorporating features to protect fabrics from excessive heat. Additionally, innovations such as moisture-sensing technologies contribute to optimized drying times by gauging the exact moisture content and adjusting the drying duration accordingly, promoting both efficiency and fabric care.

Drying, while indispensable, has long been recognized as a resource-intensive phase in textile processing. The overarching challenge lies in the inherent time and energy demands posed by traditional drying methods. This challenge spans across diverse sectors, impacting both residential dryers commonly found in households and the larger-scale industrial dryers employed in manufacturing settings [13, 14]. Time, a finite resource in any production cycle, emerges as a critical factor in textile drying. The extended duration of drying cycles not only hampers operational efficiency but also contributes to increased production costs.

While our primary focus remains on time, it is imperative to acknowledge the intertwined issue of energy consumption. Traditional drying methods, whether in residential or industrial settings, often incur significant energy costs. While the current research primarily centers on time reduction, the implications for energy efficiency remain implicit, paving the way for future investigations in energy optimization.

In the area of household appliances, drying textiles has become an integral part of daily life. Prolonged drying times not only inconvenience individuals but also elevate energy bills, underscoring the need for more efficient residential drying solutions. In industrial contexts, where large-scale textile processing is the norm, the impact of extended drying times is amplified. The productivity of these facilities is inherently tied to the efficiency of their drying processes. Time reduction, therefore, directly translates to increased throughput and reduced operational costs.

1.2 Literature review

The current generation of textile tumble dryers is plagued by issues such as low energy efficiency, uneven drying, extended drying periods, and notable loss of textile quality. In tumble dryers, regulated discontinuation methods don't save enough energy, leading to under-drying or over-drying of textiles [15]. In convective drying operations, heat recovery from exhaust air is a frequently employed energy-saving technique. Energy efficiency can be increased by making changes to the primary cycle operation, such as switching from open-cycle, air-vented dryers to closed-cycle heat pump dryers. Heat pump dryers show promise in terms of energy efficiency, but their long drying times need to be reduced for widespread adoption. Gluesenkamp et al. [16] examined the boundaries of performance for several textile drying techniques. They state that efficiency and drying time are directly dependent on each other. This means that the efficiency of the drying process is influenced by the time it takes to dry the fabric. This finding suggests that any discussions about efficiency need to take into account the drying time as well. The article mentions that the current best-performing Electric Resistance Dryers (ERDs) are able to achieve 65-75% of the maximum possible efficiency for a specific drying time. On the other hand, they state that the current best-performing Heat Pump Dryer (HPD) technology is able to achieve only 2-20% of its maximum possible efficiency.

For non-conventional food drying technologies, Menon et al. [17] mentioned that vacuum-based microwave drying is a drying method that combines the use of microwaves and vacuum conditions. In this process, food materials are exposed to microwave radiation in a low-pressure environment, which helps to remove moisture more efficiently. This technology has been shown to be energy efficient and can result in shorter drying times compared to conventional drying methods.

It has been demonstrated in Momen et al. [18] investigation that mechanical drying techniques, such as press drying, centrifugal drying, and vibrational drying, exhibit a significantly higher level of efficiency compared to the traditional thermal evaporative drying methods, with differences spanning multiple orders of magnitude. Additionally, this research has also demonstrated through experimentation that press drying achieves the greatest levels of effectiveness, with spin drying and vibrational drying following closely behind. Nonetheless, it is crucial to acknowledge that each of these methods does possess practical constraints. In real-world situations, these limitations may impede the implementation of a specific mechanical drying technique.

Convective thermal dryers are commonly used methods to dry materials. This method involves using heated air to transfer the energy required for drying and to evaporate liquid water from the surface of the fabric. The direct application of hot air is often used in this method, but it has some drawbacks [5]. One drawback is the low thermal efficiency, which means that a significant amount of energy is wasted during the drying process. Another drawback is extended processing times, which means that it takes a long time for the material to dry completely. High operating temperatures and thermal cycling can also lead to a potential degradation of the quality of the material. Material shrinkage is another issue that can occur when using the convective thermal dryer. The drying rate can be limited by several factors, including the surface area of the material, its properties, the airflow rate, and the initial moisture content [19].

Vacuum drying is one of the innovative techniques that have emerged to address the limitations of conventional drying methods. Other alternatives include compressed air and freeze drying [20], which are commonly used for heat-sensitive products.

1.2.1 Vacuum Assisted Drying

Vacuum drying works under a low-pressure condition, which leads to a reduction in water boiling temperature. This lower boiling point allows vacuum drying methods to significantly reduce drying time while maintaining low operating temperatures. Vacuum drying offers several benefits for materials that are sensitive to heat, such as pharmaceutical products. It allows for a faster drying process in a vacuum environment. Moreover, vacuum drying has the advantage of reducing oxidation rates, making it a viable choice for products that are prone to changes in their physical properties, organic compounds, and vitamins [21, 22].

The total power consumption of vacuum dryers is composed of the energy consumption of the vacuum generator and the heat source. The temperature of both the sample and the chamber is the main factor that affects the power usage of vacuum dryers. The heat source is responsible for providing the required energy to raise the temperature of the moist product and the surrounding environment to a specific level. In vacuum drying techniques, conduction is commonly used to transfer thermal energy [23, 24, 25]. From an energy efficiency perspective, vacuum-assisted drying is not a suitable option [26]. Nonetheless, Large-scale product plants can achieve greater efficiency by employing a combination of vacuum drying and other drying techniques. [27], especially when it comes to preserving the quality of the products.

1.2.2 Pulsed vacuum drying (PVD)

In recent years, there has been an increasing interest in conducting research on innovative drying techniques. These studies aim to explore new methods that can improve the drying process and its efficiency [12]. Pulsed vacuum drying (PVD) has emerged as a novel drying method that has attracted significant interest in recent times. PVD is designed to enhance the removal of moisture. This technique achieves this by utilizing pressure pulsations that occur continuously in the vacuum chamber. [28] In PVD, the pressure inside the drying chamber fluctuates in a pulsating manner. These pressure fluctuations create a dynamic environment that promotes the efficient removal of moisture from the textile being dried. The continuous and uninterrupted nature of these pressure fluctuations ensures that the drying process is optimized. Pulsed vacuum drying (PVD) is a novel drying technique that has gained popularity in recent years. It enhances moisture evacuation during the drying process by utilizing pressure fluctuations in the drying chamber. The continuous and uninterrupted nature of these pressure fluctuations improves the efficiency of the drying process.

The PVD method, which stands for pulsed vacuum drying, is considered novel because it offers significant advantages in terms of reducing drying time and improving product quality. This means that compared to traditional drying methods, PVD can dry textiles more quickly and produce higher quality results. Rakotozafy et al. [29] and Rezzoug et al. [30] conducted research on a drying method called dehydration by successive pressure drops (DDS). DDS is a technique where the drying process involves a series of pressure drops that occur one after another without interruption. The French term for this method is ”Déshydratation par Détentes Successives.” According to the studies conducted by Rakotozafy et al. and Rezzoug et al., the utilization of the DDS technique can lead to a reduction in drying time. However, it is important to consider the system parameters and operating conditions when implementing the DDS technique for optimal results. The research conducted by them suggests that the DDS technique, when used correctly, can effectively shorten the drying time. By understanding and optimizing the system parameters and operating conditions, it is possible to achieve faster drying rates using the DDS technique. This is significant because reducing the drying time can lead to increased efficiency and productivity in textile drying processes. The authors, Sanya et al. [31], conducted a thorough evaluation of two things: cyclical pressure drops and traditional approaches. The evaluation was likely done to compare the effectiveness or efficiency of these two methods in the context of the research topic. Cyclical pressure drops refer to the fluctuation or variation in pressure levels during the drying process. Traditional approaches, on the other hand, could refer to conventional drying methods that have been used in the past. The evaluation conducted by Sanya et al. likely involved analyzing the impact of cyclical pressure drops and traditional approaches on the drying rates and other properties of the textiles.

The researchers found that under certain conditions, using the PVD technique resulted in a shorter drying time and a reduced color gradient in the potato slices. [32] The shorter drying time implies that the PVD method is more efficient compared to conventional drying methods, as it can accelerate the drying process. The reduced color gradient suggests that the PVD technique helps to maintain the quality and appearance of the dried potato slices, as it minimizes the color changes that can occur during drying. The research results presented by Chua and Chou [32] demonstrate the potential benefits of using PVD in the drying of agricultural products, such as herbs and fruits, by improving drying efficiency and preserving product quality. Scholars have conducted studies to understand the relationship between the drying process and the quality of the final product.[33, 34] These studies aim to determine how different drying techniques and parameters affect the characteristics and properties of the dried product. In the context of pulsed vacuum drying (PVD), Xie et al. [13] conducted research on grapes and noted that this technique resulted in better color characteristics of the dried grapes. The drying process was also faster when PVD was used, indicating that PVD can accelerate the drying kinetics. Xie et al. also evaluated the effect of various phase durations during PVD on Chinese barriers [35]. The researchers discovered that the application of PVD enhanced the quality of the products' microstructure., suggesting that this drying technique can enhance the overall quality of the dried food items. The use of PVD leads to a higher drying rate, indicating that the drying kinetics were improved compared to traditional drying methods.

1.3 Research Objectives

To the best of our understanding, no comprehensive investigation has been conducted thus far to explore the impact of the PVD technique on the metrics of drying and the overall quality of textiles and fabrics. The central aim of this research project was to address the time-intensive nature of textile drying cycles. By specifically focusing on vacuum-assisted dryers, we sought to identify opportunities for optimization and enhancement. It is crucial to note that, while our investigation prioritizes time efficiency in vacuum-assisted dryers, we compared the results with the current solution in the market, known as heat pump dryers. Through a targeted exploration of vacuum-assisted dryers, our goal was to contribute to the evolution of textile drying methodologies, paving the way for more streamlined and resource-efficient practices.

The primary objective of this study is to examine the influence of Pulsed Vacuum Drying (PVD) on the characteristics of textiles. This will be achieved through a series of steps: firstly, a thorough analysis of the impact of PVD on the drying rate of cotton textiles in a vacuum environment; secondly, the identification and evaluation of optimal drying parameters, such as temperature, duration of the vacuum phase, and period of the atmospheric phase; and finally, the development of a practical framework for simulating thermal and mass transfer during PVD processes, thereby reducing the overall duration of the procedure. To facilitate the examination of different scenarios, a fully adapted test setup has been constructed. Additionally, the accuracy of the simulations is confirmed through experimental results.

Chapter 2

VACUUM ASSISTED DRYER EXPERIMENTAL SETUP

2.1 Introduction

This chapter navigates the design and application of a centrifugal vacuum pump, addressing key aspects such as background research, design objectives, and assumptions. It shows the current heat pump dryer system, examining components like blowers and heat pumps. Commercial vacuum cleaner motors, exemplified by AMETEK vacuum pumps, are explored alongside their flow curves and power consumption. The chapter transitions into the conceptual design of the pump, utilizing CAD models and advanced tools. Practical aspects are then introduced with the experimental setup, covering objectives, prototype challenges, and essential components like pneumatic vacuum generators. The exploration extends to vacuum-resistant drum design and the development of a vacuum dryer setup. Culminating in initial tests, the chapter provides insights into the functionality of components and considerations related to vacuum control and heat transfer mechanisms [36].

2.2 Centrifugal Vacuum Pump

The first goal and stage of the design process have been set to design and manufacture a vacuum pump that can create up to 0.1 bar vacuum inside a chamber. The overall goal of the research is to fabricate a vacuum pump to dry clothes under reduced pressure conditions. The results should be summarized in the form of CAD models that can be used to manufacture the pump and design full-scale devices capable of drying under the considered conditions [37]. After investigating the background of vacuum pumps and choosing the right type of pumps, the initial calculations were done. Secondly, constraints of the design were investigated, and according to the available commercial products, the conceptual design process started. The Vista CPD module of ANSYS software has been utilized through the conceptual design procedure to achieve higher efficiencies [36].

2.3 Vacuum pump design objectives

The objective and the goal of the design is to create vacuum up to 0.1 bar. In other words the pressure drop between inlet and outlet of the pump must be 0.9 bar.

2.4 Assumptions

To facilitate the initial estimation of parameters for the vacuum pump design, several key factors and values have been considered:

- Vacuum Cleaner Motor Assembly: Power: 1200W, Pressure: 20 kPa, Flow Rate: 3 m^3/min Vacuum Cleaner Motor Assembly: Power: 1200W, Pressure: 20 kPa, Flow Rate: 3 m^3/min
- Gradient Pressure or Pump Head: The pump head or gradient pressure required to achieve the desired vacuum level of 0.9 bar can be estimated based on the pressure drop goal.
- Inlet and Outlet Pressure: The inlet pressure should be atmospheric pressure (1 bar), and the outlet pressure should be 0.1 bar (or 0.9 bar lower than the inlet).
- Flow Rate: The required flow rate, as previously calculated, is approximately 96.3 liters per second (or 5.78 m^3/min).
- Speed of the Impeller: The speed of the impeller can be determined through surveys or selection of an appropriate pump model.
- Number of Stages: The number of stages in the pump may vary depending on the specific pump design chosen. This parameter can be determined based on the selected pump's characteristics.

- Impeller Blade Configuration: Whether the impeller blades are curved or twisted can impact the pump's efficiency and performance. This aspect can be evaluated based on surveys or specific pump design considerations.

- Impeller Geometry Parameters: Detailed impeller geometry parameters, such as blade shape, size, and curvature, can be determined through surveys or provided by the pump manufacturer.

- Air Vapor Fraction: Information regarding the air vapor fraction, which influences the behavior of water vapor in the system, can be obtained from relevant meetings or consultations, such as those with Arçelik.

2.5 Requirements

In the initial calculations for the conceptual design of the vacuum pump, several key parameters were considered to estimate the required flowrate. Here's a breakdown of the calculations:

- Initially, there are 10 kg of wet clothes with 60% moisture content, which equates to 6 kg of water in liquid form.

- These clothes are at a temperature of 40°C and a total pressure of 0.1 bar. Partial vapor pressure at this temperature and 100% relative humidity is 0.0729 bar.

- Using the ideal gas law ($PV = nRT$), it is determined that this 6 kg of water vapor or steam occupies approximately 80 m^3 (40°C and 100% RH).

- The desired drying time is set at 15 minutes.

- To achieve the required vacuum for drying, an evacuation rate of 5.78 m^3/min is necessary.

- This evacuation rate translates to 96.3 liters per second.

These calculations serve as a foundational step in the design process, helping to determine the flowrate required for efficient drying within the vacuum chamber [38]. The identified evacuation rate of 96.3 liters per second serves as a crucial benchmark for selecting an appropriate vacuum pump capable of meeting the demands of the drying process [39].

2.6 Current Heat pump dryer system

In order to get familiar with the current dryer, visits were arranged for both R&D center and the Manufacturing site of Arcelik dryer's department. The meetings were very useful in discussing the current system and assumptions for the design procedure. Figure 2.1 shows the dimensions of available space in the current dryers. These dimensions are used as assumptions for the design procedure.

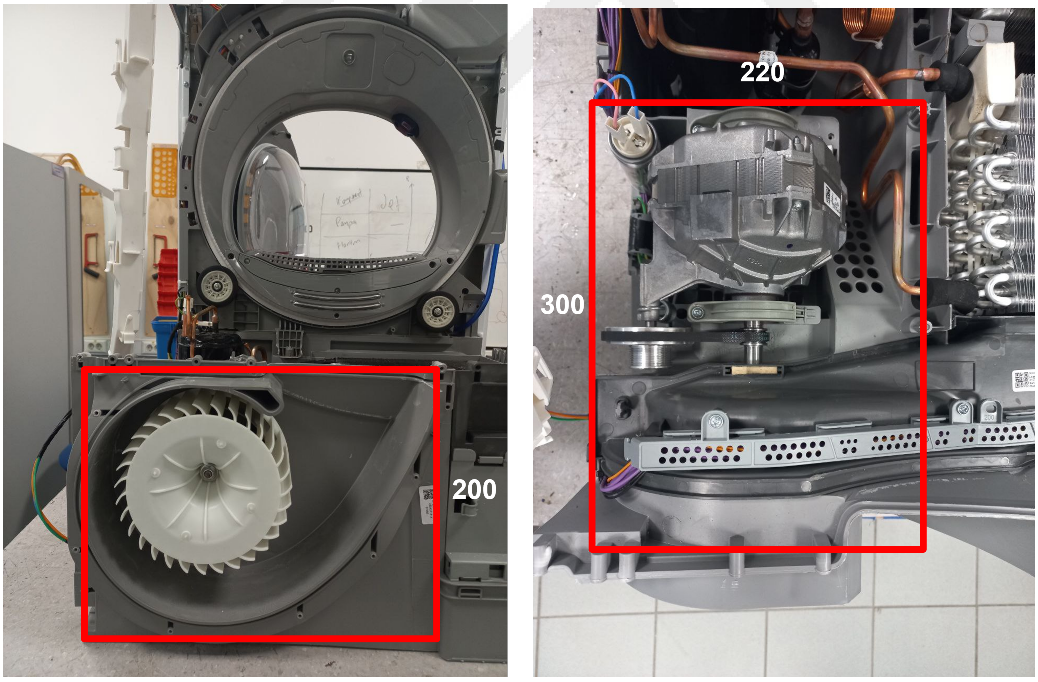

(a) (b)

Figure 2.1: Dimensions of available space in the current dryers

2.6.1 Blower

Forced air convection drying is a widely adopted drying technique characterized by the use of blowers or fans within dryers to accelerate the drying process. These blowers play a pivotal role in enhancing drying efficiency by promoting the circulation of heated air throughout the drying chamber. By continuously circulating warm air over and around the wet materials, forced air convection dryers ensure even and rapid moisture removal. The blowers inside these dryers are responsible for creating a consistent and controlled airflow pattern, which helps maintain a uniform temperature and humidity level within the drying chamber. This uniformity is crucial, particularly when drying sensitive materials like textiles or food products, as it ensures that drying occurs evenly and prevents overheating or over-drying in localized areas. Furthermore, forced air convection drying with blowers is known for its versatility, making it suitable for a wide range of applications, from industrial processes to household appliances. The ability to precisely control airflow and temperature settings allows users to tailor the drying process to specific materials and requirements, optimizing both drying speed and quality. In essence, the presence of blowers in forced air convection dryers not only expedites the drying process but also contributes to the consistency and effectiveness of the overall drying operation.

2.6.2 Heat pump

Heat pumps play a pivotal role in enhancing the energy efficiency of hybrid dryers, making them an integral component of modern drying technology. In hybrid dryers, heat pumps operate by leveraging the principles of thermodynamics to efficiently transfer heat from one medium to another. Unlike conventional dryers that primarily rely on electric or gas heating elements, heat pumps extract heat energy from the surrounding air or exhaust air stream, intensify it, and then deliver it to the drying process. This innovative approach allows hybrid dryers to achieve significant energy savings. One of the key advantages of heat pumps in hybrid dryers is their ability to recycle and reuse heat. By capturing and reusing the heat generated during the drying process, these systems minimize energy wastage and reduce overall energy consumption. Moreover, heat pumps enable hybrid dryers to operate at lower temperatures compared to conventional dryers, which not only conserves energy but also helps protect delicate fabrics by subjecting them to gentler drying conditions. Additionally, the use of heat pumps can lead to a substantial reduction in greenhouse gas emissions, contributing to more environmentally friendly drying processes. Overall, heat pumps serve as an essential technology in the quest for energy-efficient drying solutions, making hybrid dryers a promising option for those seeking to minimize energy consumption and reduce the environmental footprint of their drying operation.

2.7 Commercial vacuum cleaner motors

2.7.1 AMETEK vacuum pumps

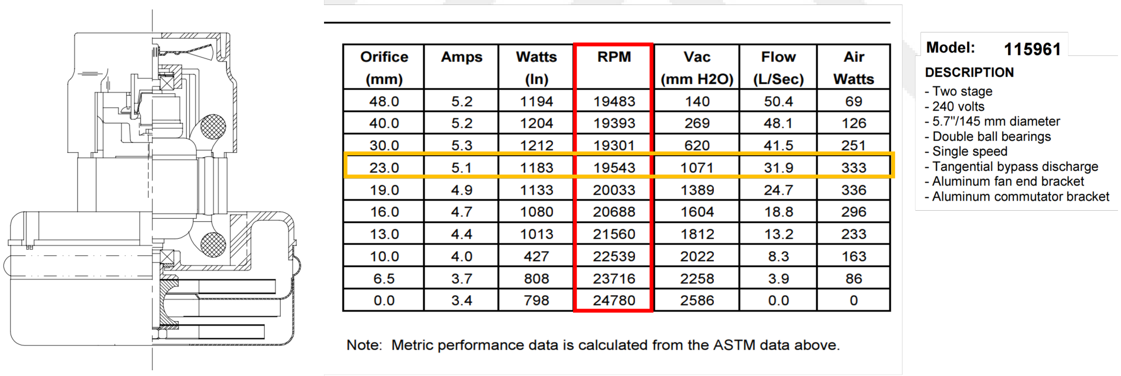

Orifice (mm)	Amps	Watts (In)	RPM	Vac (mm H2O)	Flow (L/Sec)	Air Watts
48.0	5.2	1194	19483	140	50.4	69
40.0	5.2	1204	19393	269	48.1	126
30.0	5.3	1212	19301	620	41.5	251
23.0	5.1	1183	19543	1071	31.9	333
19.0	4.9	1133	20033	1389	24.7	336
16.0	4.7	1080	20688	1604	18.8	296
13.0	4.4	1013	21560	1812	13.2	233
10.0	4.0	427	22539	2022	8.3	163
6.5	3.7	808	23716	2258	3.9	86
0.0	3.4	798	24780	2586	0.0	0

Note: Metric performance data is calculated from the ASTM data above.

Model: 115961

DESCRIPTION

- Two stage
- 240 volts
- 5.7"/145 mm diameter
- Double ball bearings
- Single speed
- Tangential bypass discharge
- Aluminum fan end bracket
- Aluminum commutator bracket

Figure 2.2: AMETEK Lamb Brushed Bypass Motors- Model 115961

AMETEK produces a diverse selection of Bypass motors suitable for various applications such as commercial floor care, central vacuum systems, and commercial and industrial uses. Bypass motors operate by keeping the working air separate from the cooling air. This is achieved by utilizing a separate fan to direct cooling air specifically towards the armature and field, Figure 2.2. It is important for manufacturers to make sure that the cooling air does not mix with the vacuum or blower air. Typically, the cooling air is provided through an opening in the equipment housing. There are two types of bypass motors: Peripheral Bypass and Tangential

Bypass. Bypass motors can be single-stage or multi-stage, Figure 2.3. The purpose of the stages is to increase pressure when used as a blower or increase lifespan when used as a vacuum. Single stage motors generally have the highest air flow/air watts but the lowest vacuum levels. By adding fan stages, the vacuum capability of the unit is enhanced but the airflow is reduced. This reduction is due to the increased resistance to airflow caused by the additional rotating and stationary fans that the air must pass through.

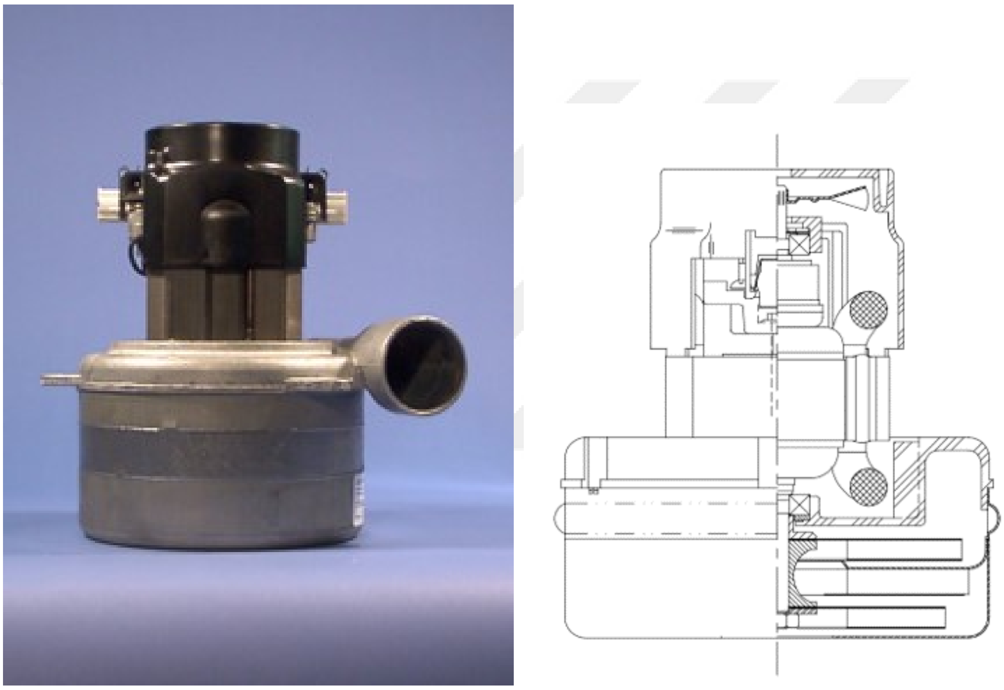

(a) (b)

Figure 2.3: 3-stage and 2-stage AMETEK vacuum pumps

As we can see in figures 2.5 and 2.4, these vacuum motors can create vacuum up to 100mm water, which is almost equal to 0.1 bar. The point is that in this state of vacuum, the flowrate is 30 L/sec maximum. Another important factor that we should be aware is the speed of rotation. These models of AMETEK have such behavior in speeds near 20000 rpm. The evaluation of such commercial products helped us to have better sight during the design and its calculations.

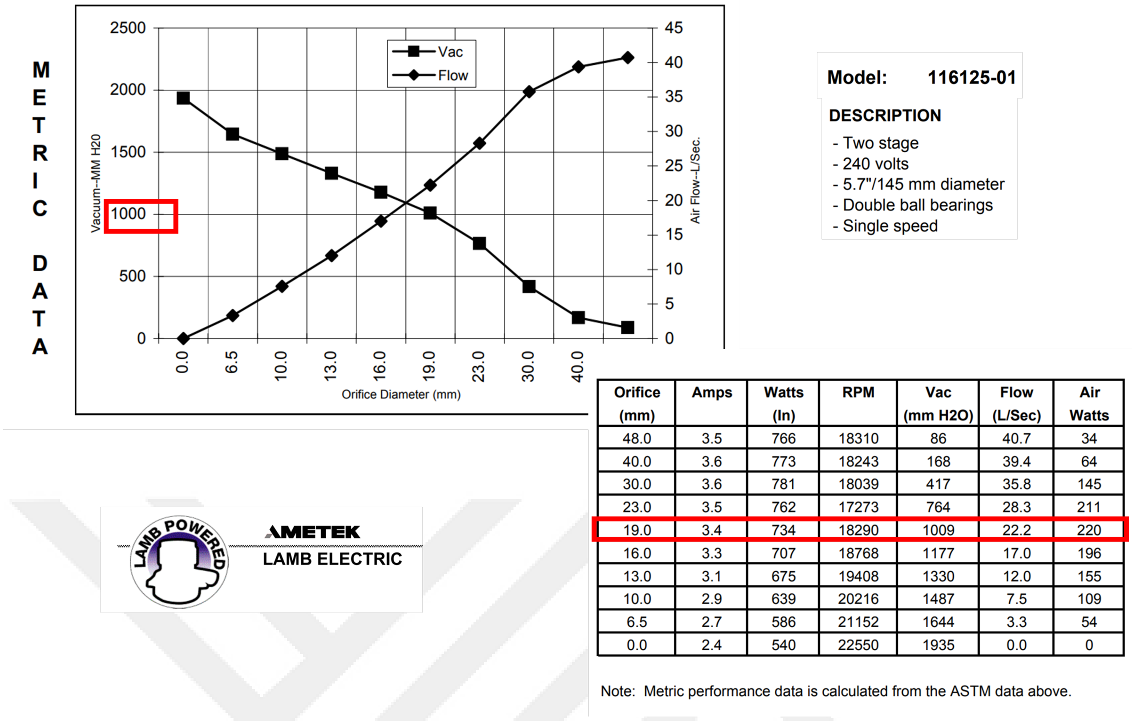

Model: 116125-01

DESCRIPTION

- Two stage
- 240 volts
- 5.7"/145 mm diameter
- Double ball bearings
- Single speed

Orifice (mm)	Amps	Watts (In)	RPM	Vac (mm H2O)	Flow (L/Sec)	Air Watts
48.0	3.5	766	18310	86	40.7	34
40.0	3.6	773	18243	168	39.4	64
30.0	3.6	781	18039	417	35.8	145
23.0	3.5	762	17273	764	28.3	211
19.0	3.4	734	18290	1009	22.2	220
16.0	3.3	707	18768	1177	17.0	196
13.0	3.1	675	19408	1330	12.0	155
10.0	2.9	639	20216	1487	7.5	109
6.5	2.7	586	21152	1644	3.3	54
0.0	2.4	540	22550	1935	0.0	0

Note: Metric performance data is calculated from the ASTM data above.

Figure 2.4: AMETEK Lamb Brushed Bypass Motors- Model 116125

2.7.2 *Wet and dry conditions*

There are some concerns about the condition in which the vacuum pump will work. The moister or humidity of the air fluid must be considered for the material selection or derivation of the design equations. In case we have compression according to the geometry of the blades, we must pay attention to the vapor ratio of the flow passing through the impeller and pump.

2.8 *The conceptual design of the pump*

2.8.1 *Preparing the CAD model of conceptual design*

A volute pump, which is the most common type of centrifugal pump, operates by converting input power into kinetic energy. This is achieved by using an impeller, a revolving device, to accelerate the liquid. The fluid enters the pump through the impeller's eye and the impeller rotates at a high speed. As a result, the fluid is propelled radially outward from the pump, creating a vacuum at the impeller's

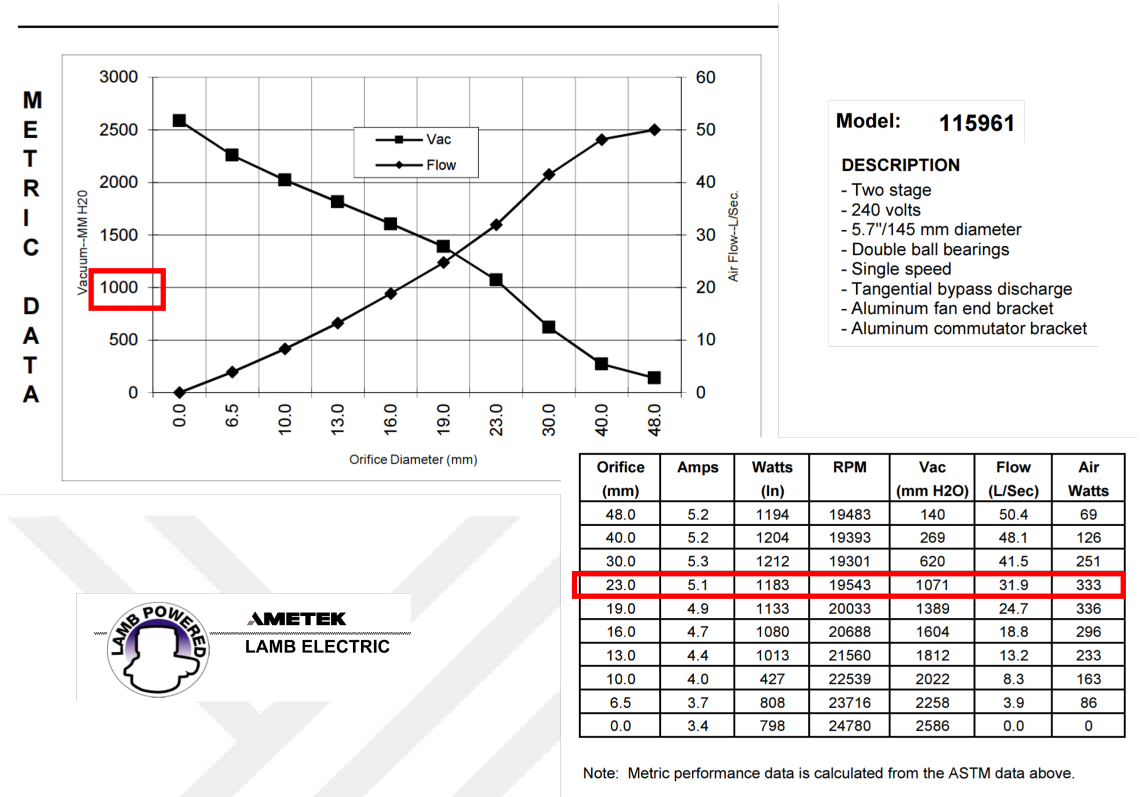

Model: 115961

DESCRIPTION
- Two stage
- 240 volts
- 5.7"/145 mm diameter
- Double ball bearings
- Single speed
- Tangential bypass discharge
- Aluminum fan end bracket
- Aluminum commutator bracket

Orifice (mm)	Amps	Watts (In)	RPM	Vac (mm H2O)	Flow (L/Sec)	Air Watts
48.0	5.2	1194	19483	140	50.4	69
40.0	5.2	1204	19393	269	48.1	126
30.0	5.3	1212	19301	620	41.5	251
23.0	5.1	1183	19543	1071	31.9	333
19.0	4.9	1133	20033	1389	24.7	336
16.0	4.7	1080	20688	1604	18.8	296
13.0	4.4	1013	21560	1812	13.2	233
10.0	4.0	427	22539	2022	8.3	163
6.5	3.7	808	23716	2258	3.9	86
0.0	3.4	798	24780	2586	0.0	0

Note: Metric performance data is calculated from the ASTM data above.

Figure 2.5: AMETEK Lamb Brushed Bypass Motors- Model 115961

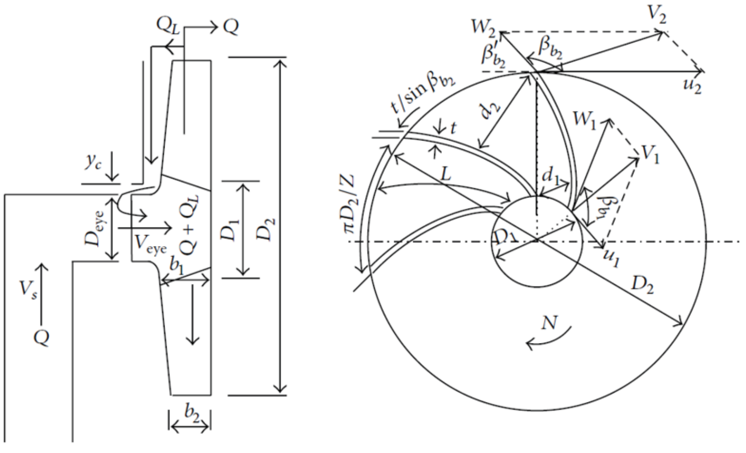

FIGURE 1: Pump impeller notations.

Figure 2.6: Pump impeller notations [2]

eye. This vacuum continuously draws more fluid into the pump. The kinetic energy in the pump is derived from the prime mover's energy, as stated by the Bernoulli

Equation. The liquid's energy is transferred based on the velocity at the impeller's edge or vane tip. The velocity of the liquid energy transferred to the liquid increases with a higher impeller speed or a larger impeller size.

2.8.2 Parameters

The main parameters are the angle of the input blade, the angle of the exit blade and the angle of wrap of the blade. The choice of 6 blades was made due to extensive research conducted by numerous scholars on the impact of the number of blades on the flow field and characteristics of a centrifugal pump, [40] [41] [42]. The researchers reached the conclusion that the number of blades had a notable impact on the size of the low-pressure area behind the blade inlet. As the blade number increased, the head also increased, but it was observed that there existed an optimal number of blades for each case. The complete list of parameters are (see figure 2.6 for more details): (a) Suction Diameter (b) Impeller Diameter (c) Outlet width (d) Inlet blade angle (e) Outlet blade angle (f) Blade wrap angle (g) Blade Height (h) Blade numbers (i) Blade Thickness (Constant Or Variable)

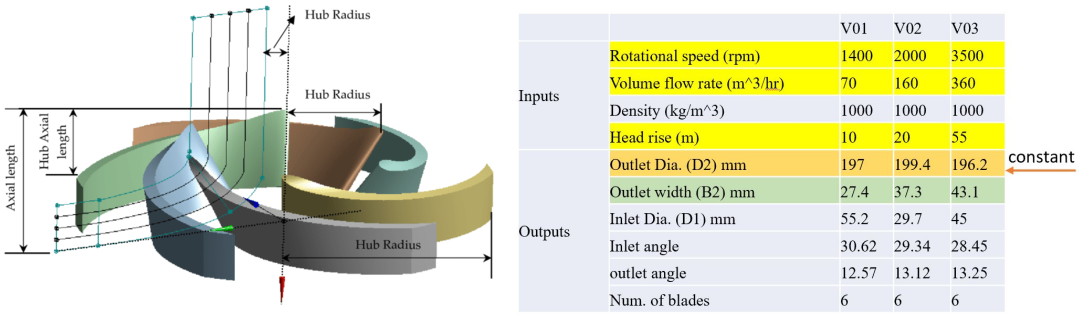

(a)

		V01	V02	V03
Inputs	Rotational speed (rpm)	1400	2000	3500
	Volume flow rate (m^3/hr)	70	160	360
	Density (kg/m^3)	1000	1000	1000
	Head rise (m)	10	20	55
Outputs	Outlet Dia. (D2) mm	197	199.4	196.2
	Outlet width (B2) mm	27.4	37.3	43.1
	Inlet Dia. (D1) mm	55.2	29.7	45
	Inlet angle	30.62	29.34	28.45
	outlet angle	12.57	13.12	13.25
	Num. of blades	6	6	6

constant

(b)

Figure 2.7: Vista CPD results; (a) Explanation of parameters, (b) Final 3 versions results

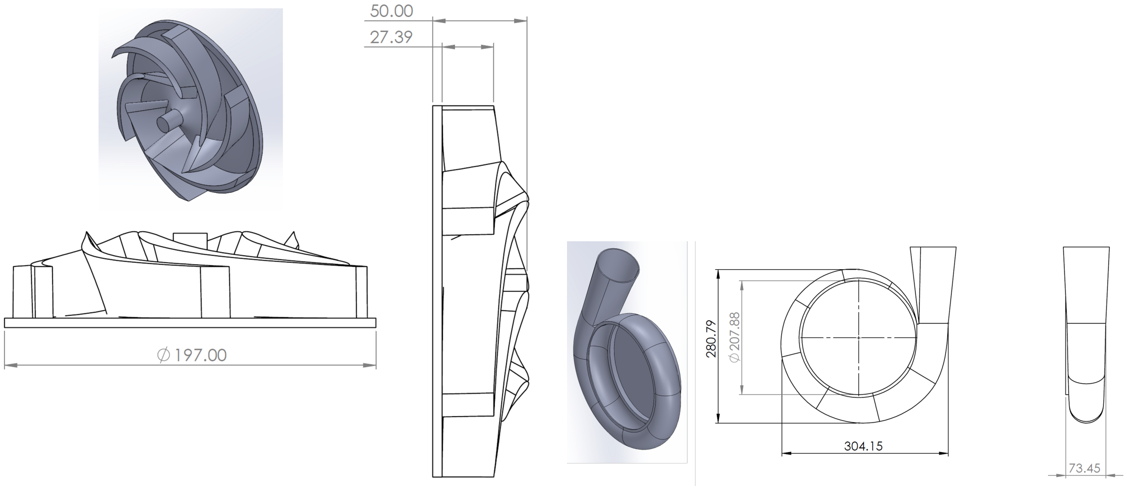

(a) (b)

Figure 2.8: The first version of vacuum pump design; (a) Impeller model, (b) Impeller model

2.8.3 Vista CPD and Blade Gen. ANSYS

Impeller and volute design: The initial step taken by Vista CPD involves creating a design for the impeller. Subsequently, the dimensions of the impeller and the fluid conditions at the impeller exit are utilized to begin the design process for the volute. This results in the development of a preliminary 3D volute shape, which can be easily converted into a complete 3D solid model using a CAD system.

The Figure 2.7 indicates that we tried to have higher flow rates, and the outlet width of the blades has increased as a result. The critical point is that according to the physical constraints in the dryer machine, the outlet diameter of the impeller was kept constant. In Figures 2.8 and 2.9 we can see the results of our investigation for impeller and volute design using Vista CPD.

2.9 Centrifugal vacuum pump experimental setup

In this section of the project, our primary objective is to evaluate the design and simulation outcomes of the centrifugal vacuum pump. To achieve this, we have taken a significant step by fabricating a scaled-down model of the centrifugal vacuum pump through 3D printing, Figure 2.10. It' is essential to emphasize that this prototyping

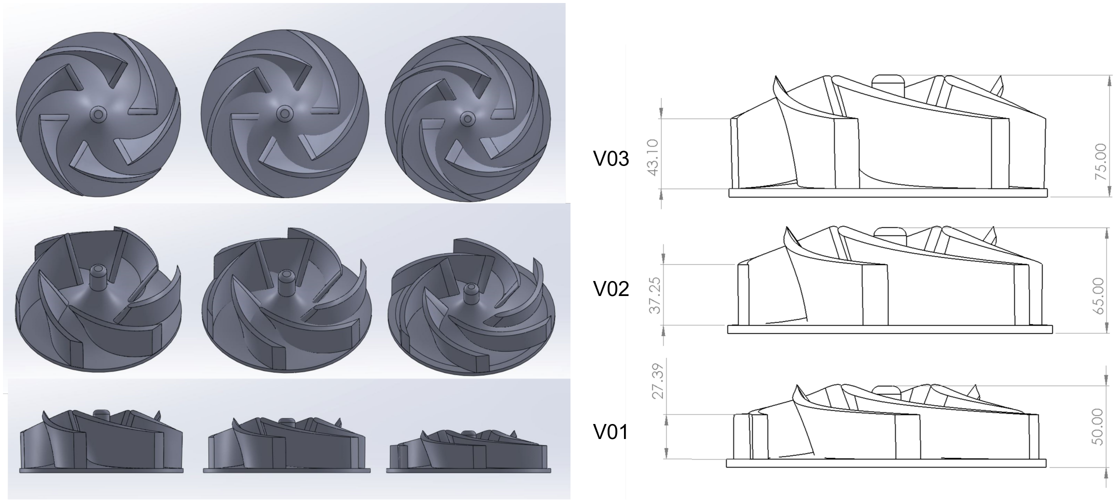

(a) (b)

Figure 2.9: Final 3 different versions; (a) Views, (b) Dimensions

effort serves a dual purpose: not only does it allow us to validate the simulation results, but it also serves as a crucial tool for assessing the proof of concept.

Through an exhaustive review of schematic diagrams and prior studies, we unearthed essential insights into the required components of an experimental setup. Key elements encompass the centrifugal vacuum pump itself, integral piping systems, data acquisition sensors, power provisions, and control mechanisms. These components serve as the foundational framework for our experimental configuration. Analyzing fluid flow pathways within earlier setups shed light on the intricate interactions between the centrifugal vacuum pump and associated components. These pathways, elucidated through schematics, contributed to our understanding of flow dynamics and potential pressure variations. The instrumentation and data acquisition methods employed in previous studies proved invaluable. Pressure gauges, flow meters, temperature sensors, and other instruments guided our selection of sensors necessary for precise performance monitoring. Safety precautions and control systems, evident in past setups, underscored the significance of integrating safety measures such as emergency shutdown systems and pressure relief valves into our design. Additionally, some previous research seamlessly integrated computational tools and software for real-time data analysis and system control. This highlighted the potential for modern technology integration in our setup, enhancing data processing and automation capabilities. By scrutinizing these schematic diagrams and past experiments, we've laid a robust foundation for our experimental configuration. These insights not only informed our component choices but also inspired innovative solutions to enhance system precision and efficiency. Armed with this knowledge, we're well-prepared for the next phase of our project.

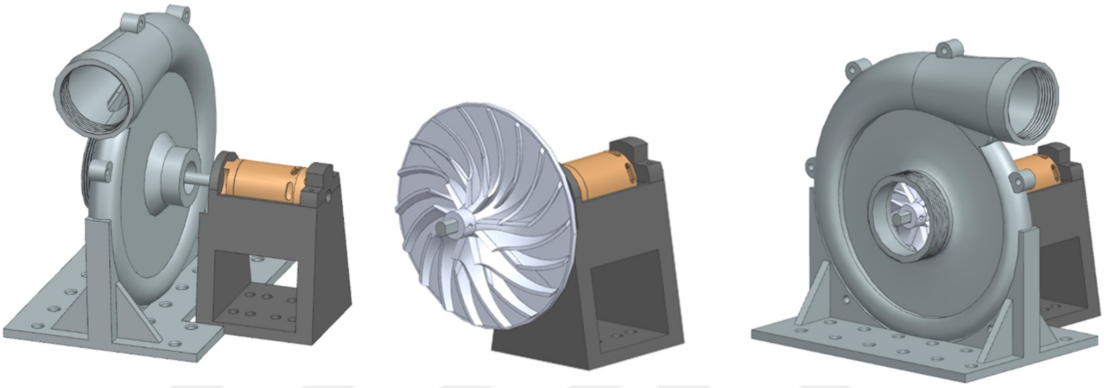

Figure 2.10: 3D CAD models of the scaled vacuum pump

2.9.1 Objective and Significance of Prototyping

One of the pivotal aspects of this project involves the design and simulation data pertaining to the centrifugal vacuum pump. This phase serves as a pivotal juncture where we transition from theoretical simulations to practical validation. To bridge this gap, we have undertaken the construction of a scaled model of the centrifugal vacuum pump using advanced 3D printing technology. This prototype holds paramount significance, as it not only serves as a means to corroborate our simulation findings but also acts as a litmus test for the overall feasibility of our concept. The 3D printing technique employed in the creation of the scaled model (shown in figure 2.10) warrants mention. Through meticulous precision and attention to detail, we have successfully replicated the pump's design in a smaller form factor. This process ensures that the prototype accurately mirrors the key features and intricacies of the actual centrifugal vacuum pump, enabling us to carry out a comprehensive evaluation.

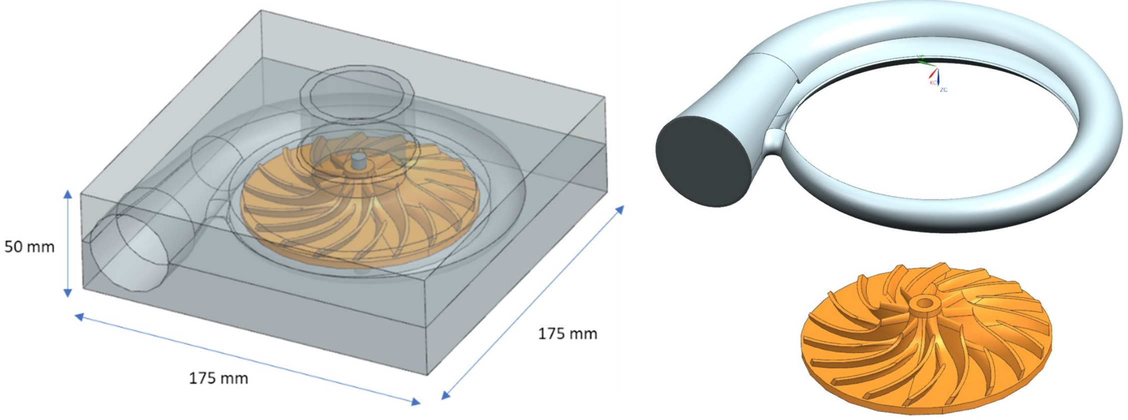

Figure 2.11: The model design for CNC machining

In our project, we had the opportunity to employ a 5-axis CNC machine for the fabrication of the volute and impeller components of the centrifugal vacuum pump, Figure 2.11. However, after careful consideration of both time constraints and budget limitations, we opted not to pursue this advanced machining method. Several factors influenced our decision, including the following:

(a) Time Efficiency: Utilizing a 5-axis CNC machine would undeniably expedite the manufacturing process and potentially yield highly precise components. However, given our project's timeline, we needed to balance speed with other critical project aspects.

(b) Budgetary Considerations: The acquisition, setup, and operation of a 5-axis CNC machine can be a significant investment. We assessed our project's financial constraints and decided to allocate resources judiciously to other project phases and requirements.

(c) Prototyping Emphasis: It is important to note that our primary objective in this phase of the project is prototyping. As such, the utmost precision achievable through CNC machining may not be essential at this stage. We prioritized cost-effective methods that would enable us to quickly produce functional prototypes for testing and validation.

(d) Resource Allocation: We directed our resources towards other critical aspects of the project, such as materials, testing equipment, and data analysis tools. These resources were deemed more crucial to the overall success of the prototype and proof-of-concept evaluation.

By not pursuing CNC machining for the volute and impeller components, we acknowledge that we may encounter slight variations in component precision. Nevertheless, this decision aligns with the pragmatic approach of optimizing our available resources to achieve our project's goals efficiently. As this phase of the project focuses on the initial development and validation of our concept, we believe that the chosen manufacturing method strikes a sensible balance between cost-effectiveness and project progress.

2.9.2 The issues of the prototype

In the development of our prototype for the centrifugal vacuum pump, several key issues have come to our attention. These issues encompass various aspects of the prototype's design and functionality, and we are actively addressing them to enhance the performance and reliability of the system. Below, we outline these issues:

1. Clearance (Impeller and Volute): One of the foremost concerns is the clearance between the impeller and the volute. Achieving the optimal clearance is essential to ensure efficient fluid flow and prevent any undesirable friction or turbulence. We are currently working on refining the design and manufacturing processes to achieve the precise clearance required for optimal pump performance.

2. Shaft and Supports (Two Bearings on One Side): The arrangement of two bearings on one side of the shaft raises concerns about stability and alignment. We are actively evaluating the support structure and shaft design to ensure

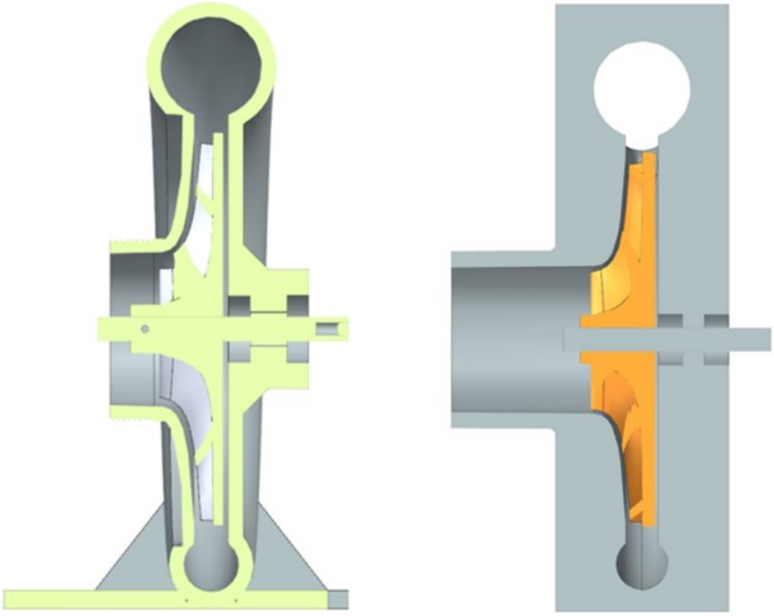

Figure 2.12: Cross section view of the model for both 3D printing and CNC

proper alignment and load distribution. This is crucial for minimizing wear and extending the operational life of the pump.

3. Motor and Impeller Coupling: The coupling between the motor and impeller is pivotal for the efficient transfer of power. We are investigating the coupling mechanism to ensure it can transmit power seamlessly while minimizing energy losses. Proper alignment and secure coupling are essential for the pump's overall functionality.

4. Sealing the Volute: Effective sealing of the volute is vital to prevent any air leakage and maintain a vacuum environment. We are exploring sealing solutions and gasket materials to ensure a tight seal and minimize the risk of air ingress, which could adversely affect pump performance.

5. Inlet and Outlet Connections: The design and integrity of the inlet and outlet connections are crucial for fluid intake and discharge. We are reviewing these connections to optimize their design, material, and sealing mechanisms to prevent any leaks or inefficiencies in the fluid flow.

6. Dynamic Balancing: Achieving dynamic balance in the impeller is essential to minimize vibrations and ensure smooth operation. We are actively conducting balancing tests and fine-tuning the impeller design to eliminate any imbalances that could lead to mechanical stress or reduced performance, Figure 2.12.

Addressing these prototype issues is pivotal to the successful development of our centrifugal vacuum pump. We are committed to refining and optimizing the design, manufacturing, and assembly processes to ensure that our prototype functions efficiently, reliably, and in accordance with the project's objectives. Each of these challenges represents an opportunity for improvement and innovation as we work towards a successful proof of concept.

2.9.3 The actuator of the prototype

The motor selected for our setup is the QX-MOTOR 2600KV Brushless Motor, which boasts several noteworthy specifications and features. Below, we provide a concise overview of the motor's details: 1. KV (rpm/v): 2600KV 2. Continuous Current: 80A 3. Peak Current: 2200mAh 4. Lipo(s): 3S (12V) 5. Length: 63.5mm 6. Size: 48.8mm 7. Shaft Diameter: 4mm 8. Special Features: Waterproof, High Temperature Resistant

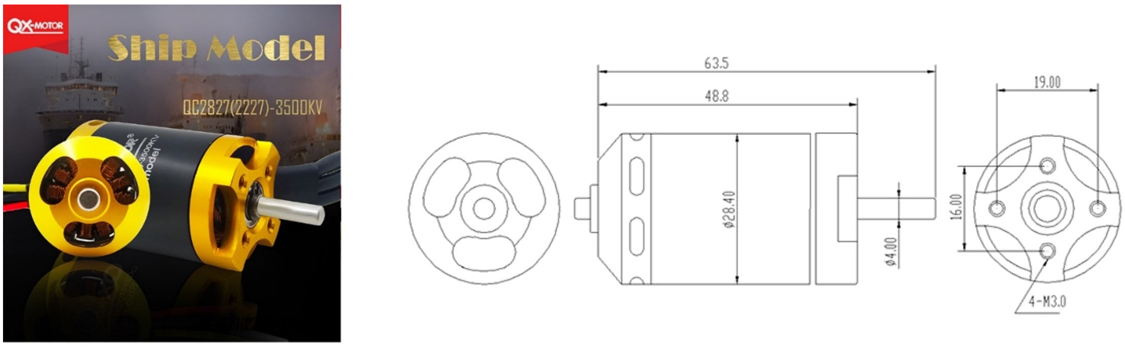

Figure 2.13: The QX-MOTOR 2600KV Brushless Motor

The motor shown in Figure 2.13 which has high KV rating of 2600KV indicates that it is well-suited for applications requiring a high rotational speed. It can operate on a 3S LiPo battery, providing a voltage of 12V. The motor is capable of continuous operation at 80A, with a peak current rating of 2200mAh, making it suitable for demanding applications. Furthermore, its compact size, with a length of 63.5mm and a diameter of 48.8mm, makes it a practical choice for our setup. The 4mm shaft diameter ensures a robust connection to the impeller or other mechanical components. The standout features of this motor include its waterproof design, which adds durability and versatility to its applications. Additionally, its resistance to high temperatures makes it suitable for operation in environments where elevated temperatures may be encountered, Figure 2.14. By incorporating the QX-MOTOR 2600KV Brushless Motor into our setup, we aim to leverage its impressive specifications and features to drive the centrifugal vacuum pump efficiently and reliably. This motor's performance characteristics align with the demands of our project, and its robust design ensures that it can withstand the conditions encountered during operation.

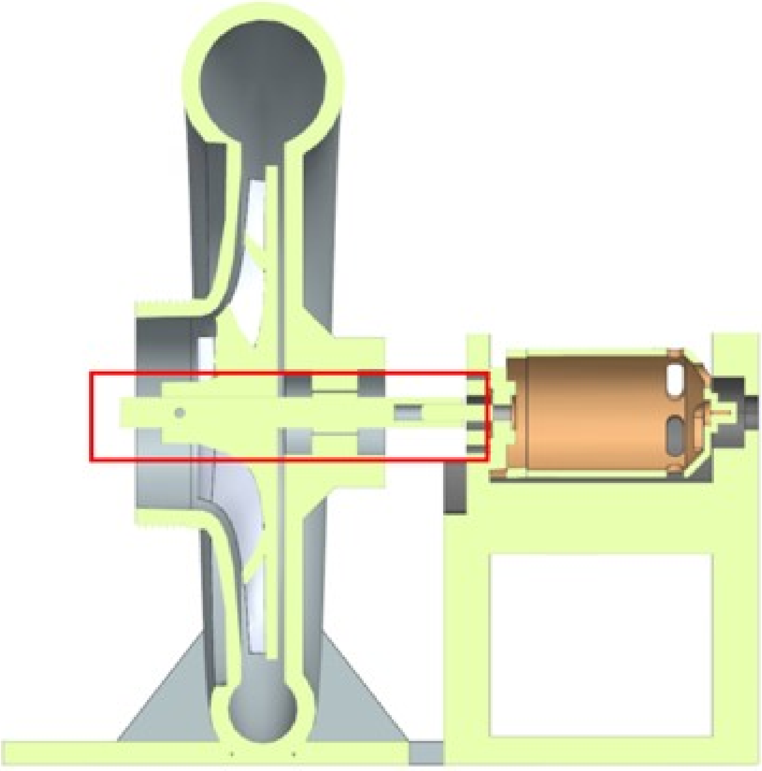

Figure 2.14: Cross section view of the model for both 3D printing and CNC

2.9.4 Design and manufacture of the shaft

Designing and manufacturing the shaft for our centrifugal vacuum pump is a critical aspect of ensuring the system's reliability and performance. Several key calculations and considerations have been made using KISSsoft software, based on design assumptions, limitations, and simulation results. Shaft Specifications 1. Shaft Material: Aluminum 2. Diameter: Two sections, 9 mm and 7 mm 3. Length: 75 mm 4. Maximum Allowable Deflection: 43 µm (micrometers) 5. Speed: 20,000 rpm 6. Axial Load: 160 N 7. Radial Load: 34 N 8. Torque: 35 mN·m 9. Bearings: Deep groove bearings (7mm diameter, 19mm outer diameter, 6mm width)

Calculations and Considerations

- Static Load: The static load on the shaft is the axial and radial load applied to it when the system is at rest. In this case, the axial load is 160 N, and the radial load is 34 N.

- Dynamic Load: The dynamic load takes into account the forces acting on the shaft due to its rotation at 20,000 rpm. This includes the centrifugal forces generated by the impeller's mass and the fluid it moves, in addition to the axial and radial loads.

- Axial and Radial Load: The axial and radial loads are the forces applied along and perpendicular to the shaft's axis, respectively. These loads must be considered when designing the shaft to prevent deformation or failure.

- Speed: The speed of the shaft, which is 20,000 rpm, is a crucial parameter as it affects the dynamic loading and stress on the shaft, Figure 2.16.

- Static Equivalent Radial Load (Pr): The static equivalent radial load (Pr) is calculated to determine the equivalent radial load that would cause the same amount of deflection as the actual combination of radial and axial loads. This is essential for assessing the shaft's deflection under real-world conditions.

- Dynamic Radial Load Rating (Cr): The dynamic radial load rating (Cr) is a key parameter in bearing selection. It represents the load, in this case, the radial load, that the bearing can withstand while maintaining a rated life of a specific number of revolutions.

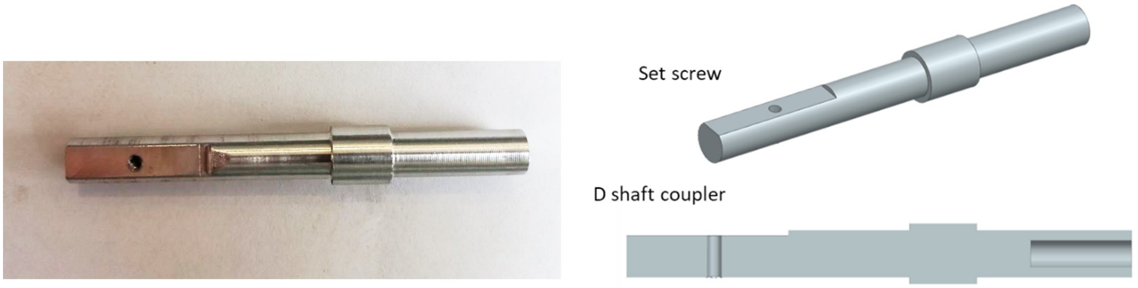

Figure 2.15: Modeled and manufactured shaft

Using KISSsoft software, these calculations and considerations have allowed us to design a shaft that can withstand the applied loads, operate at the specified speed, and maintain the necessary deflection limits. The choice of aluminum as the shaft material is suitable for this application, given the provided specifications and design constraints. Additionally, the selection of appropriate bearings is crucial to ensure the longevity and reliability of the shaft and the overall centrifugal vacuum pump system. As shown in Figure 2.15, The manufacturing of the shaft for our centrifugal vacuum pump presented several notable challenges that required careful consideration and innovative solutions. These challenges revolved around ensuring the secure fixation of the impeller, particularly the use of set screws, and achieving dynamic balance to avoid issues at the high operational speed of 20,000 rpm.

Impeller Fixation with Set Screws

Fixing the impeller securely to the shaft posed a significant challenge. The impeller is a critical component responsible for generating the vacuum and fluid flow within the pump. To ensure it remains firmly attached during operation, set screws were employed as a common method for fixation. However, the challenge here lies in

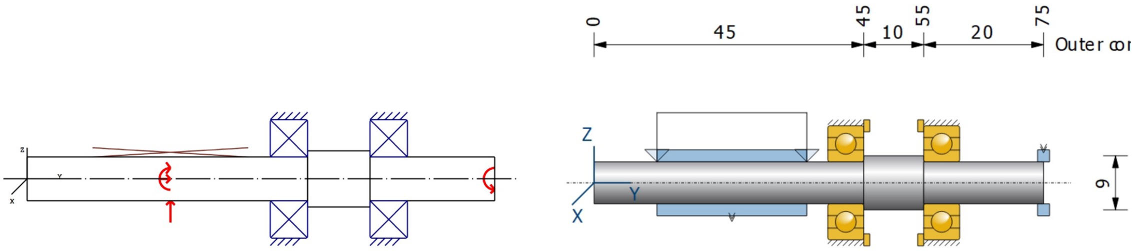

Figure 2.16: The model of the shaft in KISSsoft software- location of the bearings and forces applied.

striking the right balance between a secure connection and potential issues such as stress concentration. If the set screws are over-tightened, they can induce undue stress in the shaft material, potentially leading to failure. On the other hand, insufficient tightening may result in the impeller slipping or wobbling, adversely affecting pump efficiency and causing wear and tear. To address this challenge, meticulous engineering analysis and testing were carried out to determine the optimal torque for the set screws, ensuring a secure connection without compromising the integrity of the shaft.

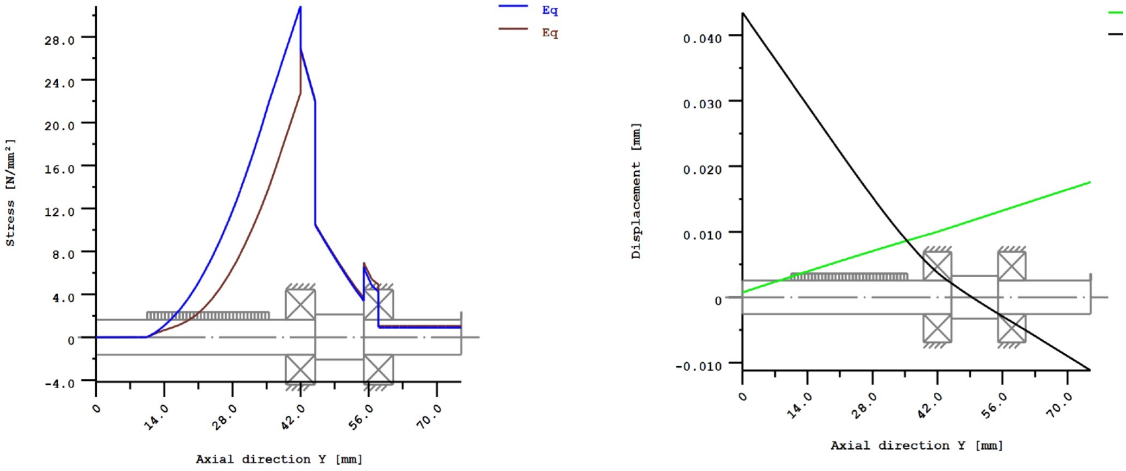

Figure 2.17: Plots of shaft's stress and displacement under the load

Dynamic Balancing for High-Speed Operation

Operating at 20,000 rpm imposes stringent requirements on the dynamic balance of the shaft. Even the slightest imbalance can lead to significant vibrations and potential mechanical failures. Dynamic balancing involves redistributing mass along the shaft to minimize eccentricity and ensure smooth, vibration-free rotation. Achieving dynamic balance at such high speeds is a formidable task. It necessitates precision in machining and the careful distribution of weights, often through the addition of counterweights or by selectively removing material. The challenge lies in striking the right balance (no pun intended) between removing enough material to achieve balance while retaining the structural integrity of the shaft. In response to this challenge, advanced balancing equipment and techniques were employed, allowing for the precise measurement of imbalance and the application of counterweights or adjustments as needed. The iterative process of balancing and testing was crucial to fine-tuning the shaft's dynamic balance, ensuring that it operates smoothly and reliably at 20,000 rpm, Figure 2.17. In conclusion, the challenges encountered in shaft manufacturing, including impeller fixation with set screws and achieving dynamic balance for high-speed operation, demanded a combination of engineering expertise, precision machining, and iterative testing. These challenges were met with careful consideration, innovative solutions, and a commitment to achieving the utmost reliability and performance in our centrifugal vacuum pump system.

The utilization of 3D printing technology in our project introduced its own set of challenges, particularly concerning the prolonged duration of printing and the installation of bearings within the printed components. 1. Long Duration of Print: The process of 3D printing, while immensely versatile and capable of producing intricate components, often entails extended printing durations. This can be attributed to factors such as layer-by-layer additive manufacturing and the intricacy of the components being fabricated. In our project, these extended print times presented both logistical and practical challenges. One primary challenge was managing the time required for printing. Long printing durations can lead to increased resource consumption and scheduling conflicts. To address this, meticulous planning and

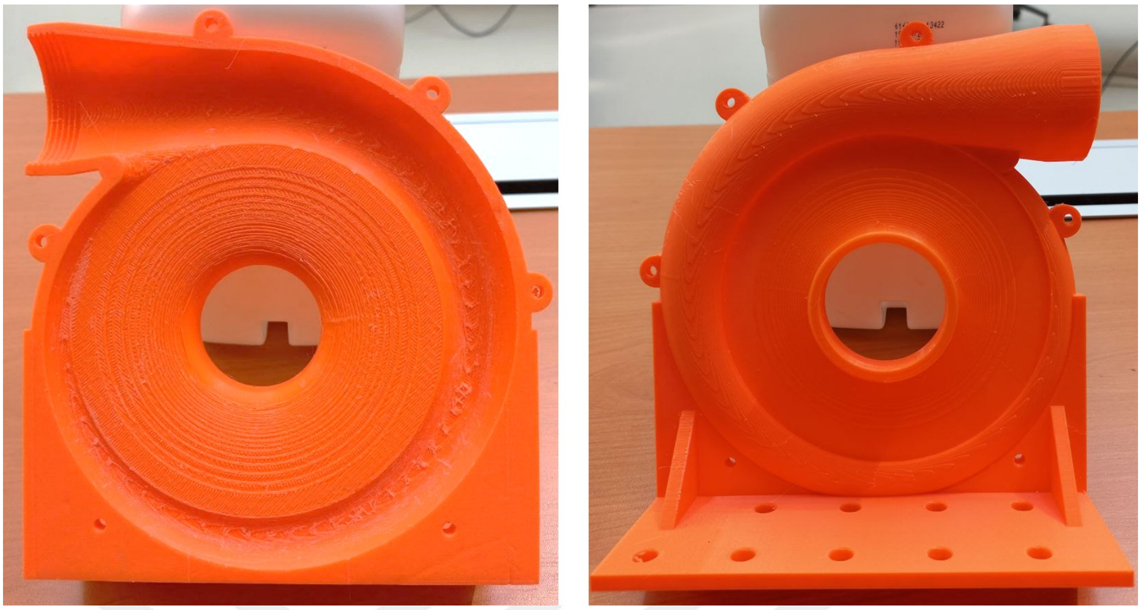

Figure 2.18: The 3D Printed parts of the vacuum pump

scheduling were crucial. Print jobs were meticulously timed to optimize resource usage and ensure that critical components were available when needed. Moreover, monitoring the 3D printer during extended runs was vital to identify any potential issues, such as layer adhesion problems or filament feed disruptions, that could compromise the quality of the printed parts. This vigilance allowed us to address issues promptly and minimize the risk of having to restart a lengthy print job.

2. Installation of Bearings: Integrating bearings into 3D-printed components can pose unique challenges. Bearings play a pivotal role in ensuring smooth and low-friction movement, particularly in rotating components like shafts and impellers. Ensuring a precise and secure fit for bearings within 3D-printed parts was essential to guarantee the functionality and longevity of the system. Challenges arose in achieving the correct dimensions for bearing housings. The 3D printing process may introduce tolerances and variations that affect the fit of the bearings. To mitigate this challenge, post-printing processes such as sanding or fine-tuning of the bearing seats were employed to ensure a proper fit. Additionally, careful measurement and selection of bearings were essential to match the printed parts' specifications. Furthermore, the choice of bearing retention methods, such as press-fitting or adhesive

bonding, required careful consideration to strike the right balance between a secure attachment and potential damage to the 3D-printed components.

In summary, the use of 3D printing in our project presented challenges related to the extended duration of printing and the installation of bearings. These challenges were met through meticulous planning, vigilant monitoring, and post-printing adjustments to ensure that the printed components met the required specifications and contributed to the overall success of our centrifugal vacuum pump prototype, Figure 2.18 and Figure 2.19.

Figure 2.19: The printed volute and impeller before complete assembly

In addition to the previously discussed issues, several more challenges have arisen in the development of our centrifugal vacuum pump prototype. Here are details about these additional issues:

1. Motor Coupling: The motor coupling mechanism, which connects the motor to the impeller, is crucial for efficient power transfer and preventing any misalignment or wobbling. Achieving a secure and reliable motor coupling, especially at high speeds, presents a challenge. The coupling must transmit the motor's rotational force seamlessly while maintaining balance and alignment. Detailed engineering analysis and testing are essential to ensure a robust motor coupling mechanism. 2.

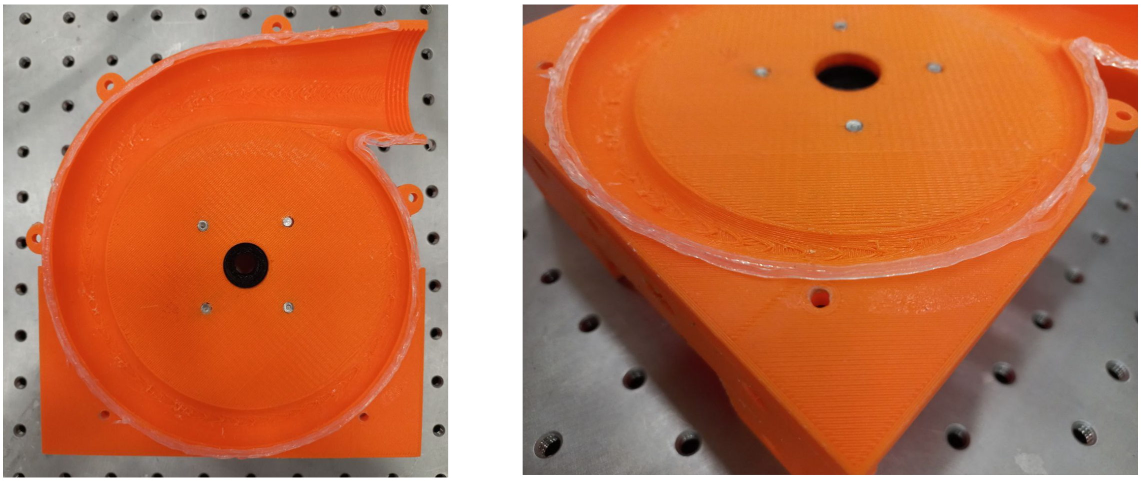

Figure 2.20: Using silicon glue as sealing material.

Sealing the Volute: The sealing of the volute, using transparent aquarium silicone (Akvaryum Silikon Şeffaf), is a notable challenge. A reliable seal is essential to maintain the vacuum environment and prevent any air leakage. As shown in Figure 2.20, ensuring a tight and durable seal, particularly in the presence of high-speed rotation and potential temperature variations, requires careful material selection and precise application techniques.

3. Inlet and Outlet Connections for Measurements: The design and integration of inlet and outlet connections for measurement purposes present challenges in terms of fluid flow dynamics and data accuracy. The connections must not interfere with the pump's performance and should facilitate accurate data acquisition. This involves optimizing the design of the connections and selecting appropriate sensors and measurement devices.

4. Bearing Thermal Issue (@ High RPMs): Operating at high RPMs can generate heat within the bearings, potentially leading to thermal issues. Excessive heat can accelerate wear and reduce the bearing's lifespan. Effective heat dissipation and temperature monitoring mechanisms are essential to mitigate this issue and ensure the bearings' long-term reliability.

5. Stroboscope Tachometer (Unable to Measure Higher than 9999 RPM): The limitation of the stroboscope tachometer in measuring speeds higher than 9999 RPM

poses a challenge in accurately monitoring the system's performance. At 20,000 RPM, a more specialized tachometer or alternative speed measurement method may be necessary to ensure precise speed monitoring and control.

Addressing these additional challenges requires a combination of engineering expertise, innovative solutions, and rigorous testing. Each challenge presents an opportunity for optimization and refinement as we work toward the successful development and validation of our centrifugal vacuum pump prototype.

RPM measurement

In the pursuit of accurate and real-time RPM (Revolutions Per Minute) measurement for our centrifugal vacuum pump prototype, we employed a precision-driven approach that leveraged advanced laser sensor technology. This innovative method was instrumental in achieving exceptional sample rate and precision, essential for monitoring the system's performance.

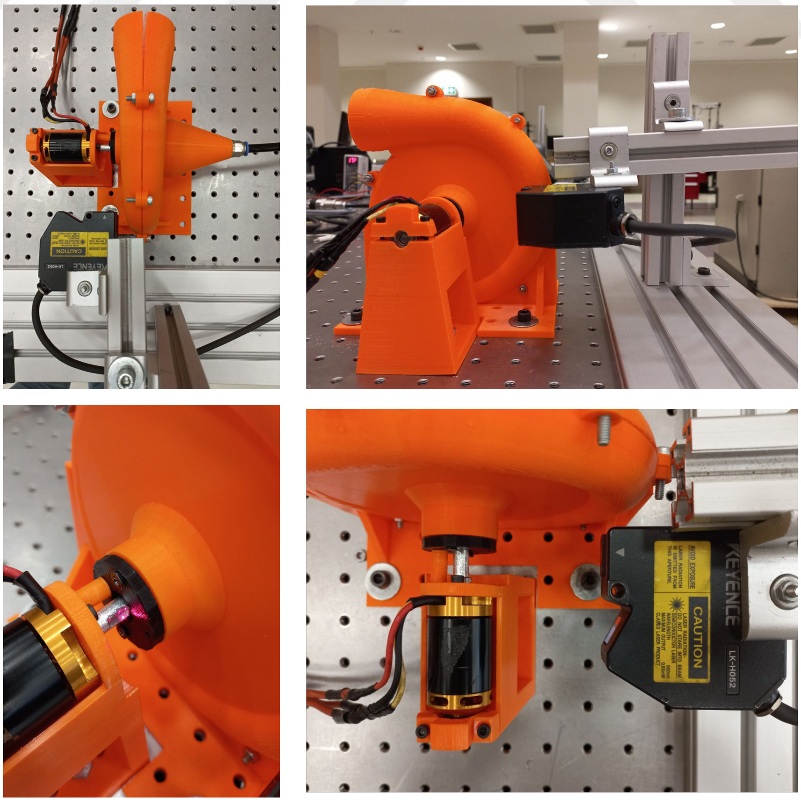

Figure 2.21: RPM measurement setup and configuration using laser sensor.

To measure the RPM of the rotating components, we employed a high-resolution laser sensor with the capability to precisely detect the motion of a reflective surfac, Figure 2.21. In this context, a segment of the aluminum shaft was utilized as the ideal reflective target due to its smooth surface finish and durability.

The laser sensor was strategically positioned adjacent to the rotating shaft, ensuring a consistent line of sight to the reflective surface. As the shaft rotated, the sensor emitted a laser beam toward the reflective segment of the shaft. The reflected laser beam was then detected by the sensor, and the system's onboard electronics processed the signals.

The choice of a laser sensor for RPM measurement was driven by its ability to provide outstanding precision and accuracy, even at high speeds. The sensor's rapid data acquisition capability allowed us to capture a significant number of data points per rotation, resulting in a high sample rate.

This high sample rate, combined with the reflective nature of the shaft segment, enabled us to obtain RPM measurements with exceptional granularity and accuracy. It ensured that even at the system's operational speed of 20,000 RPM, we could precisely monitor and control the rotational dynamics. Benefits and Implications: The utilization of the laser sensor and the aluminum shaft reflector offered several notable advantages for our project:

1. High Sample Rate: The sensor's rapid data acquisition facilitated real-time monitoring of RPM with precision.

2. Non-Intrusive: This measurement method was non-intrusive and did not interfere with the system's operation.

3. High-Speed Compatibility: The system effectively measured RPM at the challenging operational speed of 20,000 RPM.

4. Data Accuracy: The reflective nature of the shaft segment ensured minimal measurement error, resulting in highly accurate RPM data.

Incorporating the laser sensor and aluminum shaft reflector into our project's RPM measurement system has proven to be a pivotal decision. This approach provided us with an exceptional level of precision, enabling us to monitor the centrifugal vacuum pump's performance with the utmost accuracy. The robust and non-intrusive nature of this measurement method ensures its applicability in high-speed rotational systems, underlining its significance in achieving our project objectives.

Prototype Results

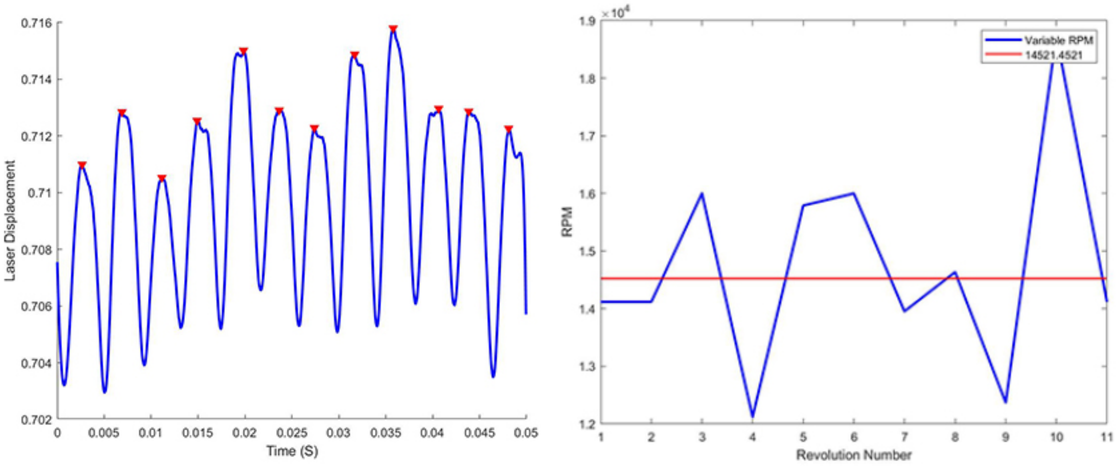

Figure 2.22: plots of the RPM measurement

In our pursuit of precise RPM measurement using laser sensor data, we adopted a systematic data processing approach. The initial step involved filtering the raw data meticulously to eliminate any noise or minor fluctuations that might introduce inaccuracies into our RPM calculations. This noise reduction process ensured that only relevant and consistent information contributed to the final result, shown in Figure 2.22. With the filtered data in hand, we represented it in its cyclic form. As the shaft rotated, the laser sensor's measurements exhibited periodic patterns corresponding to each revolution. This cyclic representation allowed us to accurately identify key characteristics of each revolution. Within these cyclic representations, we employed peak detection algorithms to identify specific points in the data that corresponded to the highest displacement values. These peaks marked the completion of each revolution and served as crucial reference points for RPM calculation.

Once the peaks were identified, we measured the time intervals between them. This interval represented the time taken for one complete revolution and was a fundamental parameter for calculating RPM. By determining the time required for a single revolution, we could accurately calculate how many revolutions occurred in one minute, thereby yielding the RPM value. This meticulous data processing approach ensured that our RPM calculations were not only accurate but also highly reliable. By converting laser displacement data into RPM values through this systematic process, we obtained real-time insights into the centrifugal vacuum pump's rotational dynamics, enabling precise monitoring and control of the system's performance. Our centrifugal vacuum pump prototype demonstrated impressive performance, with key achievements in terms of speed and vacuum generation. During testing, we achieved a maximum rotational speed of 14,000 RPM, showcasing the pump's ability to operate efficiently at high speeds, shown in Figure 2.23. Furthermore, the prototype exhibited remarkable vacuum generation capabilities, reaching a vacuum level of 4 percent. This achievement underscores the pump's effectiveness in creating a substantial pressure differential, which is essential for various vacuum applications. Utilization of Vacuum Pressure Sensor: To accurately measure and validate the vacuum levels achieved during testing, we employed a vacuum pressure sensor. This sensor provided precise and real-time data regarding the vacuum conditions within the pump, ensuring that our experimental results were both reliable and consistent.

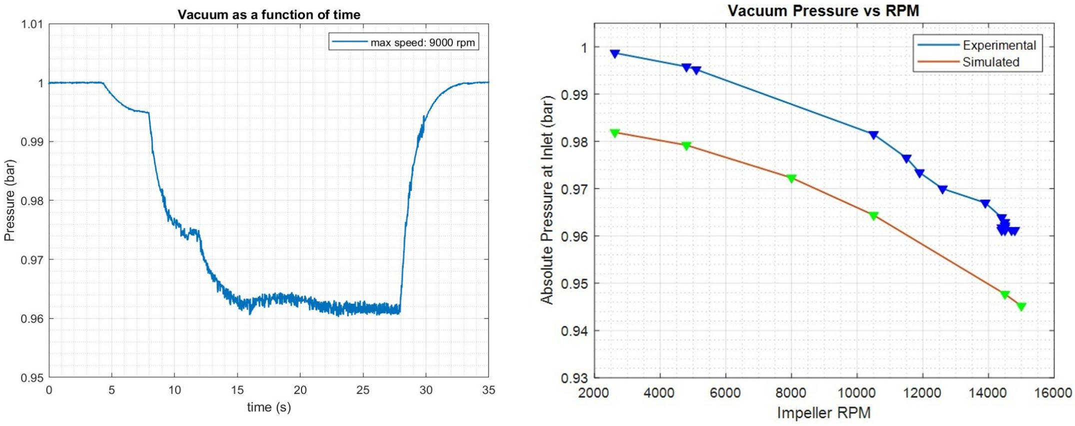

Figure 2.23: Vacuum results of the prototype model

To assess the performance of our prototype comprehensively, we conducted a comparative analysis between the experimental results and the outcomes predicted by our simulation models, shown in Figure 2.23. The plotted data vividly illustrates this comparison, allowing us to evaluate the accuracy of our simulations and identify any variations or discrepancies between the predicted and observed performance metrics. This side-by-side analysis between simulation and experimentation forms a critical component of our project's validation process, affirming the capabilities and limitations of our centrifugal vacuum pump prototype. The results obtained not only underscore our achievements but also provide valuable insights about the feasibility of utilizing the centrifugal vacuum pump for this specific purpose.

2.10 Pneumatic vacuum generator

As we assessed the performance and capabilities of the centrifugal vacuum pump, it became evident that it might not be the ideal solution for our vacuum generation needs. In response to this realization, our project direction shifted towards exploring alternative options, particularly the utilization of vacuum generators.

Vacuum generators offer a distinct approach to creating vacuum conditions and can often provide unique advantages over traditional vacuum pumps. Through research and evaluation, we aim to identify the most suitable vacuum generator technology that aligns perfectly with our project's demands, ensuring that we achieve the desired vacuum levels and operational efficiency. This transition in our approach highlights our dedication to adapting and refining our strategies to deliver the best possible outcomes in our vacuum-related applications.

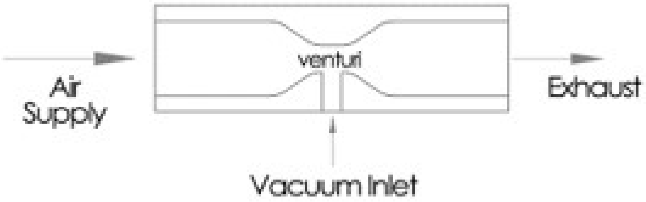

Figure 2.24: Vacuum generator and venturi principle

2.10.1 The theory of pneumatic vacuum generators

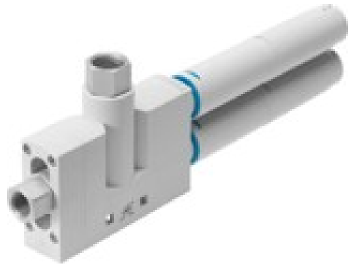

Figure 2.25: Festo vacuum generator- VN-30-H-T6

The concept of the Venturi principle lies at the heart of vacuum generators, providing an ingenious mechanism for creating vacuum conditions. According to this principle, as a fluid (often air or a gas) flows through a constricted region of a tube or nozzle, its velocity increases, while its pressure decreases. This decrease in pressure creates a suction effect, drawing in nearby fluids or gases, including those from the surrounding environment, Figure 2.24. In the context of vacuum generators, this principle is harnessed to generate vacuum by exploiting the pressure differential between the high-velocity, low-pressure region within the constricted area and the comparatively higher pressure in the surroundings. By controlling the flow of the fluid and the geometry of the Venturi tube or nozzle, vacuum generators can efficiently create and maintain vacuum levels for various applications, making them a versatile and highly effective choice in industries such as manufacturing, automation, and material handling.

In our pursuit of an efficient vacuum generation solution, we conducted extensive research and found that Festo offers a wide range of vacuum generators that cater to diverse vacuum requirements. Within Festo's extensive lineup, we identified two primary categories that align with our project needs: high vacuum models and high suction models. The high vacuum models offered by Festo, shown in Figure 2.25, are engineered to achieve exceptional vacuum levels, reaching up to an impressive 93%. These vacuum generators are equipped with Laval nozzles in various nominal sizes, including 0.45 mm, 0.7 mm, 0.95 mm, 1.4 mm, 2.0 mm, and 3.0 mm. This variety of nozzle sizes allows for precise customization, enabling us to tailor the vacuum generation to our specific application requirements.

On the other hand, Festo's high-suction models prioritize rapid evacuation times, making them an excellent choice for applications where quick vacuum creation is essential. These models feature a compact and sturdy design, optimizing space utilization while ensuring reliable performance. Furthermore, they are known for their wear-resistant and maintenance-free operation, enhancing the durability and longevity of the vacuum generation system. The modular system offered by Festo provides a broad selection of components, allowing us to configure a vacuum solution that perfectly aligns with our project's needs. After careful consideration of the vacuum level and suction vacuum flow requirements, we have selected the high vacuum models from Festo. This choice reflects our commitment to achieving the desired vacuum conditions efficiently and effectively, leveraging Festo's renowned expertise in vacuum generation technology. In the Figure 2.26, we have presented some details about the high vacuum models from Festo. The plots are Air consumption q_n as a function of operating pressure p_1, Suction rate q_n (with respect to atmosphere)

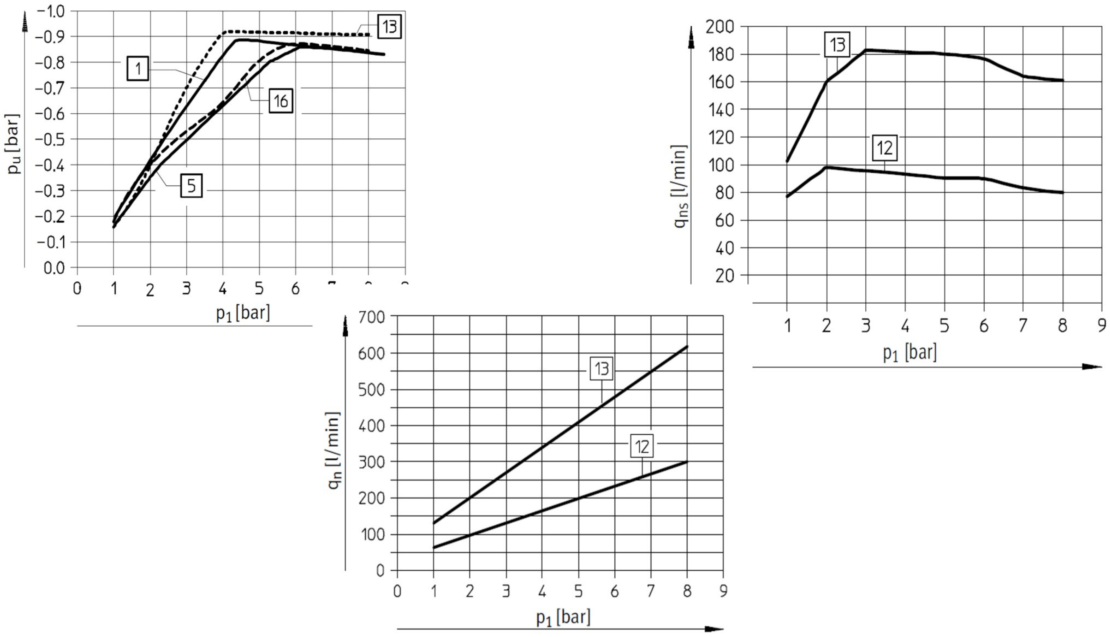

Figure 2.26: Functionality plots Festo vacuum generator- VN-30-H-T6 (lines with label 13)

as a function of operating pressure p_1, and Vacuum p_u as a function of operating pressure p_1.

2.11 Vacuum-Resistant Drum Design

Arçelik previous chamber

We were able to access to a report from Arçelik R&D team that contains pictures of the previous experimental setup, shown in Figure 2.27. The details of these pictures gave us some ideas about designing the new experimental setup. For more information about the old chamber and the results of experiment you may refer to the specified report.

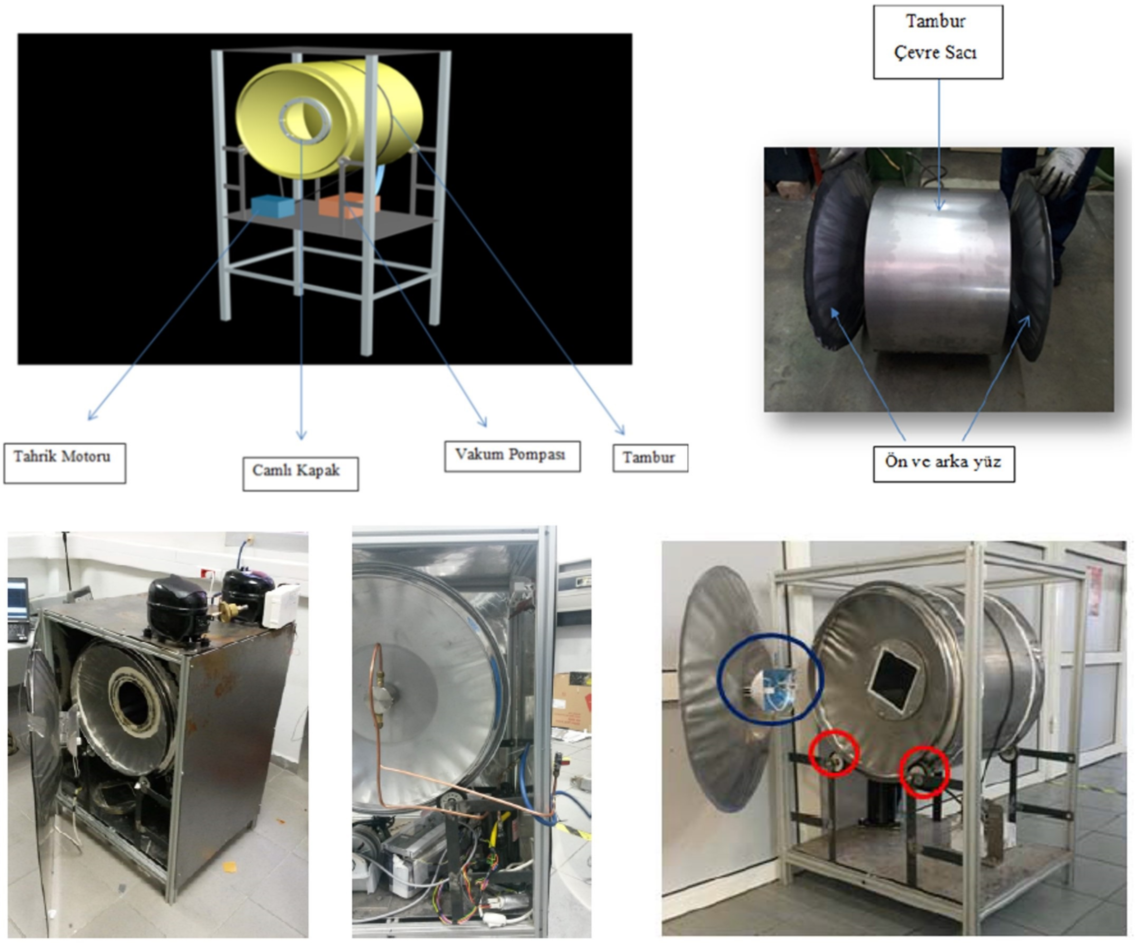

Figure 2.27: Arçelik previous chamber design and setup picture

The rotary distributor

In our quest to create a seamless and reliable connection for our rotating vacuum drum, we explored various solutions and found a remarkable fit in the Festo single and multiple rotary distributors, shown in Figure 2.28. These innovative distributors offer a secure means of transmitting media, including compressed air and vacuum, from stationary sources to rotating machine parts, precisely addressing our project's unique needs.

One of the standout features of the Festo rotary distributor is its flexibility in media supply and return. With both radial and axial inputs and outputs, it enables us to supply and return the medium either from the side or from below, depending on the specific requirements of our system. Moreover, the distributor's sturdy and compact design, equipped with double bearings, ensures that our media supply remains resilient against mechanical loads, guaranteeing reliable and uninterrupted operation of our rotating vacuum drum. This integration not only streamlines our design but also aligns with our commitment to employing reliable and complete solutions that can be trusted to perform consistently.

Figure 2.28: Festo rotary distributor used in the previous setup.

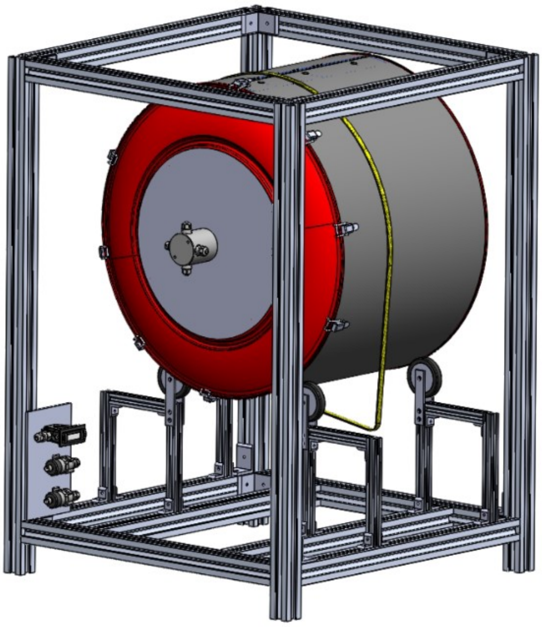

Figure 2.29: 3D CAD model of the experimental setup - version 1

2.11.1 Vacuum Chamber

In the early stages of our experimental setup design, we drew inspiration from a previous configuration, seeking to leverage existing resources to streamline our project. The rendered images shown in Figure 2.29 visually represent our preliminary design, showcasing our creative approach to repurposing Arçelik dryer drums as a central component of our setup. One of the primary challenges we encountered during this phase of our design was ensuring the structural integrity of the repurposed dryer drums under the applied vacuum load. Calculations and assessments were carried out to evaluate the drums' strength and durability, as maintaining the vacuum environment without compromising safety was of paramount importance.

Sealing the drum effectively under vacuum conditions also emerged as a critical consideration. We embarked on an extensive search for vacuum sealing solutions, exploring various options to achieve an airtight seal capable of withstanding the vacuum pressures required for our experiments.

An advantageous aspect of this design approach was the potential to utilize the rotation mechanism already inherent in Arçelik dryers. This not only simplified the

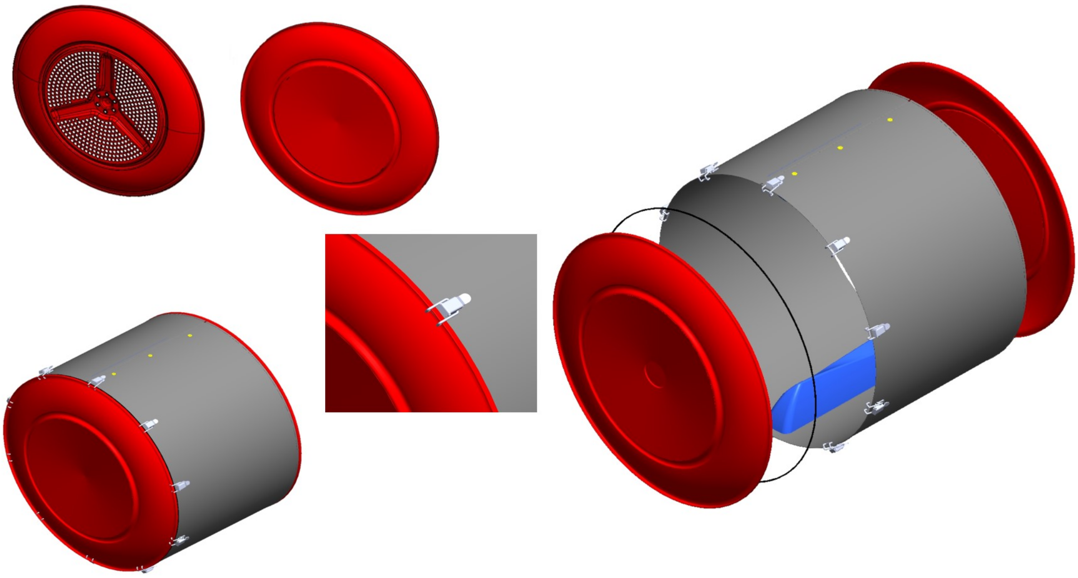

Figure 2.30: Components and details of the design – back view

implementation of the drum's rotational movement but also allowed us to leverage the robust and reliable rotation mechanisms developed by Arçelik for their dryers. In summary, our preliminary design of the experimental setup capitalizes on the ingenuity of repurposing Arçelik dryer drums while addressing key challenges related to structural strength, vacuum sealing, and rotation. This approach, although presenting some initial complexities, holds promise in providing an efficient and cost-effective solution for our vacuum-related experiments while benefiting from the proven mechanisms of Arçelik dryers.

Preliminary Calculations

In the design and construction of our experimental setup, one of the critical considerations was the structural integrity of the chamber under varying pressure conditions. Specifically, we needed to ensure that the chamber could safely withstand a pressure differential of 0.1 bar (10000 Pa) while maintaining its structural integrity. To achieve this, we conducted a thorough calculation to determine the required thickness of the chamber's wall. The calculation was based on the fundamental principles of pressure vessel design, taking into account key parameters such as the pressure differential (ΔP), the chamber's radius (r), the yield strength (σ_y) of the chosen stainless steel material, and a safety factor (SF) to account for uncertainties and safety margins. The formula used for this calculation is derived from the hoop stress equation for cylindrical pressure vessels:

$$\sigma_h = \frac{\Delta P.r}{t} \tag{2.1}$$

Where σ_h represents the hoop stress (Pa), ΔP signifies the pressure differential (Pa), r denotes the radius of the chamber (m), t corresponds to the required thickness of the chamber's wall (m).

Rearranging the formula to solve for thickness (t), we obtained:

$$\begin{aligned} t &= \frac{\Delta P \times r}{\sigma_h} \times SF \\ t &= \frac{90 \times 10^3 \times 0.3}{312 \times 10^6} \times 10 = 0.87mm \end{aligned} \tag{2.2}$$

Upon substituting the values relevant to our design, including the pressure differential of 0.1 bar, a radius of 0.3 meters, and the yield strength of the stainless steel material, our calculation yielded a required wall thickness (t) of approximately 0.87 mm. This calculation ensures that the chamber possesses the structural integrity necessary to contain the specified pressure without exceeding the yield strength of the material. This meticulous evaluation of chamber thickness is indicative of our commitment to safety and precision in our project's design and execution, providing a robust foundation for the successful implementation of our experiments.

The collaborative discussions with the Arçelik team have led to significant refinements in our approach to the design of the drum and its associated components for our experimental setup. Here's a concise overview of the decisions and innovative ideas that emerged from these discussions.

Following consultations with the Arçelik team, we've opted for sheet metals and welding as the primary construction materials and method for the drum. This decision ensures that our drum design meets the necessary structural requirements while benefiting from the expertise of sheet metal fabrication and welding techniques. To facilitate the ease of opening and closing the drum, we've considered implementing latches as a practical and reliable mechanism (see figures 2.31 and 2.30). Latches

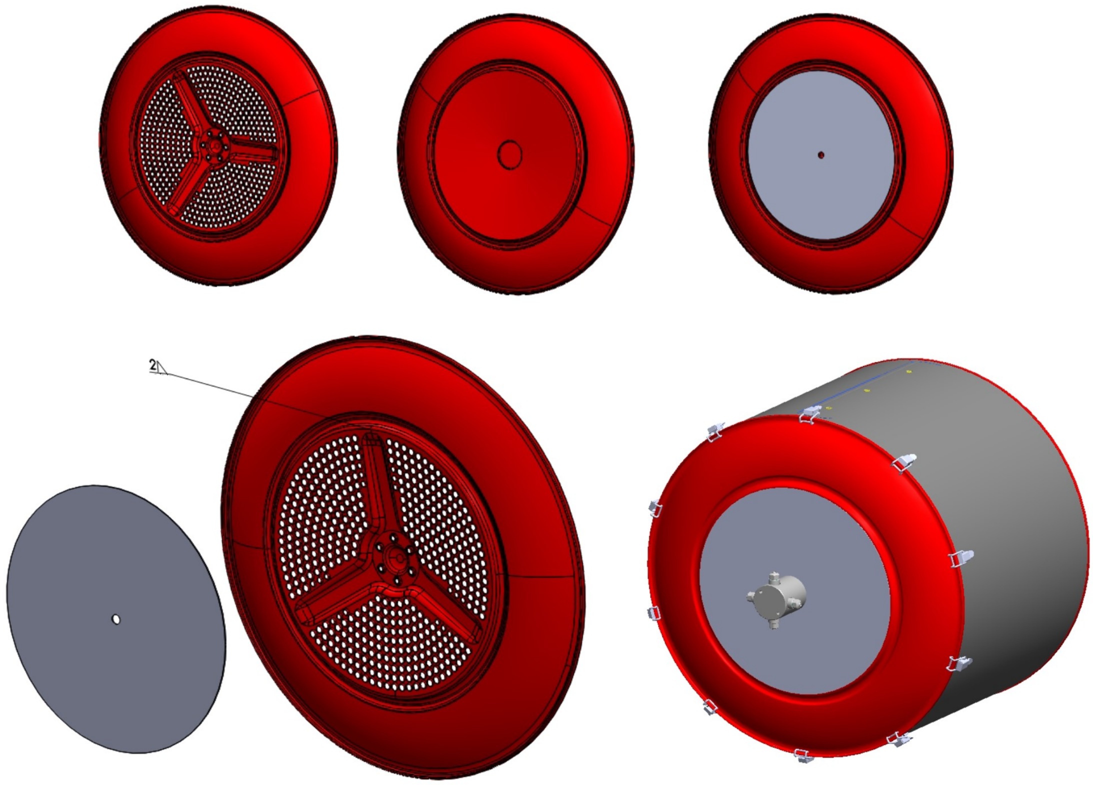

Figure 2.31: Vacuum drum CAD model- how to create sealed drum – front view.

offer user-friendly operation while ensuring the secure closure of the drum during vacuum experiments. This approach simplifies the handling of the drum and enhances the overall user experience. Addressing the critical sealing issue, we have explored innovative sealing solutions. One promising approach involves the utilization of O-rings, known for their effective sealing properties. Additionally, the combination of silicon glue and corn powder presents a creative DIY solution for custom O-rings. This blend provides the versatility to shape and adapt the seals to various applications, offering a cost-effective and adaptable sealing solution tailored to our specific needs. These collaborative decisions and innovative ideas exemplify our commitment to refining our project design while incorporating practical solutions to ensure the success of our vacuum experiments. By drawing on the collective expertise and creativity of our team and the insights from Arçelik, we are poised to achieve our project objectives with efficiency and precision.

Figure 2.32: Picture of the manufactured setup by Arçelik team

Preliminary tests

Upon receiving the setup and vacuum chamber, shown in Figure 2.32, we initiated rigorous testing of the drum under vacuum conditions, seeking to evaluate its structural performance and integrity. The plot of chamber pressure over time, as depicted in the figure 2.33, illuminated a critical observation: the occurrence of buckling at a pressure of 0.15 bar, equivalent to 85% vacuum. This unexpected deformation prompted a comprehensive analysis, which revealed intriguing details. One notable observation was that the buckling predominantly transpired in the regions where welding had been employed 2.34. This observation provides a pivotal clue in understanding the underlying factors contributing to the structural issue. By leveraging our calculations and simulations, we aim to delve deeper into this phenomenon, dissecting the stress distribution, material properties, and weld integrity to pinpoint the precise mechanisms at play. The revelation of six lobes in the buckling pattern further enriches our analysis, offering valuable insights into the underlying dynamics of this structural response. This multifaceted examination, incorporating experimental data, computational simulations, and engineering expertise, positions us to not only address the buckling issue effectively but also to refine our design and construction methodologies. As we proceed, our objective remains unwavering: to rectify the structural vulnerabilities, ensuring that the drum can confidently withstand the rigorous demands of vacuum conditions, thus advancing the success of our experimental endeavors.

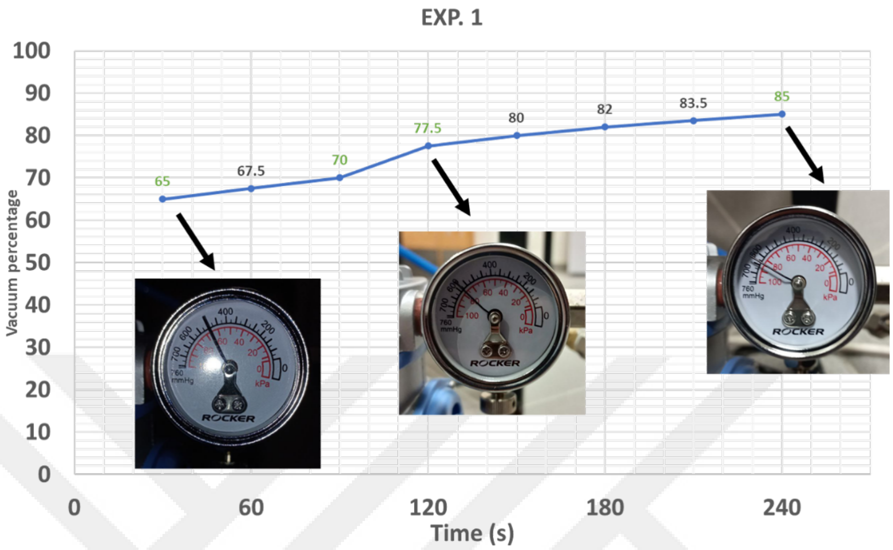

Figure 2.33: Preliminary test results of vacuum drum failure

Empirical Design Approach By NASA

In our pursuit to unravel the causes behind the buckling phenomenon observed in our vacuum drum, we employed a method grounded in empirical engineering expertise, notably NASA's Empirical Design Approach. This approach is renowned for its practicality and effectiveness in evaluating the structural stability of cylindrical vessels subjected to uniform radial and axial pressures.

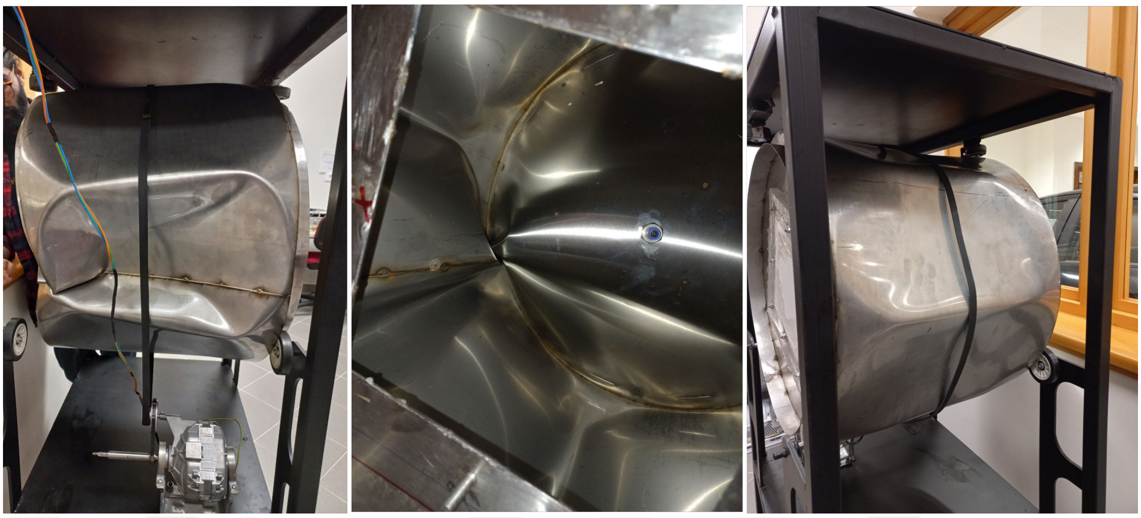

Figure 2.34: Buckled drum pictures.

Our first application of the NASA Empirical Design Approach was directed at calculating the critical pressure threshold at which our drum exhibited buckling behavior. This critical pressure represents the limit beyond which the structural integrity of the drum is compromised. By leveraging the empirical formulae and methodologies provided by NASA, we were able to obtain a precise assessment of this crucial parameter. This calculation formed the foundation for understanding the drum's vulnerability under vacuum conditions.

The critical pressure corresponds to:

$$p_{cr} = \frac{0.855}{(1-\nu^2)^{\frac{3}{4}}} \cdot \frac{E\sqrt{\lambda}}{(\frac{r}{t})^{\frac{3}{4}}(\frac{L}{r})} = 0.82e5Pa = 0.82bar \tag{2.3}$$

Where ν is Poisson's Ratio, E is Modulus of Elasticity, λ is the correction factor (see [43] for details), r is cylinder radius, L is cylinder length, and t is cylinder thickness. In parallel with the critical pressure calculation, the NASA Empirical Design Approach enabled us to ascertain a key structural characteristic—the number of lobes (n), see figure 2.35. The concept of lobes relates to the manner in which a cylindrical vessel may collapse when subjected to external pressures. This insightful determination offers a deeper understanding of the buckling patterns and structural response exhibited by our drum under the influence of uniform radial and axial pressure. By integrating NASA's empirical methodologies into our analysis, we've embarked on

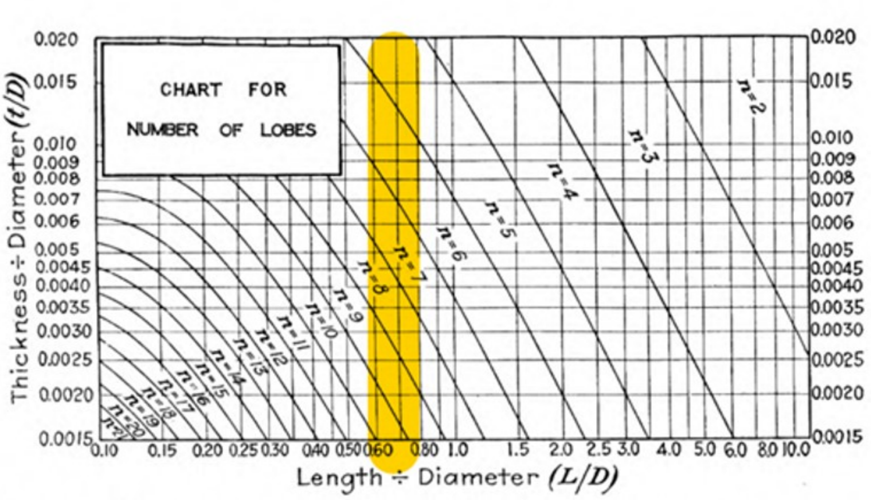

Figure 2.35: Number of lobes (n) in which the cylinder might collapse when subjected to uniform radial and axial pressure [3]

a comprehensive exploration of the structural dynamics of our vacuum drum. This approach not only enhances our ability to diagnose the causes of buckling but also provides essential data for optimizing our design and reinforcing structural integrity, ultimately ensuring the reliability of our drum in demanding vacuum environments [44].

Structural enhancements

The occurrence of failure in our vacuum drum underscored the critical need for structural enhancements and in-depth welding analysis to bolster the integrity of our design. Recognizing the paramount importance of addressing this challenge, we explored several innovative solutions:

1. Structural Supports for the Drum
2. Drum-in-a-Drum Concept for Pressure Gradient
3. Welding Analysis and Critical Points
4. Realistic Sheet Thickness and Weight Optimization

5. FEM Analysis for Structural Assessment

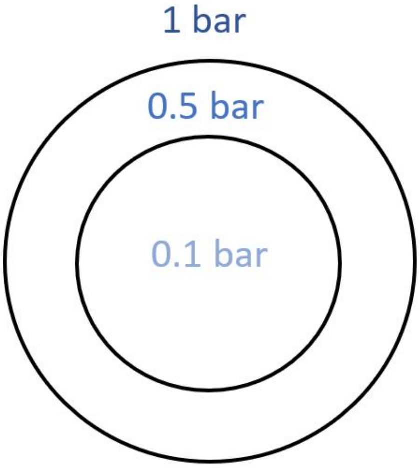

Figure 2.36: Concept of Drum in a drum and creating pressure gradient.

L-Shape Supports: Incorporating L-shaped supports strategically positioned along the drum's circumference can effectively distribute external pressures, mitigating the risk of buckling and deformations. These supports provide crucial reinforcement to maintain the structural integrity of the drum under vacuum conditions.
Circular Supports: Circular supports placed within the drum can further enhance stability. By creating additional points of contact and evenly distributing pressure, these supports contribute to a more robust and resilient drum design.
Leveraging the concept of a "drum within a drum," we aim to create a pressure gradient within the chamber 2.36. This innovative approach involves the installation of an inner drum that can counteract the external vacuum forces by introducing a controlled internal pressure. This pressure differential can significantly alleviate the structural stresses experienced by the outer drum, enhancing its resistance to buckling. These proactive measures and innovative solutions represent our unwavering commitment to rectifying failure model 1 and fortifying our vacuum drum's structural integrity. By integrating these enhancements and leveraging advanced analysis techniques, we aim to not only address past challenges but also set a solid foundation for the success of our vacuum experiments.

Ring-Stiffened Corrugated Cylinders: Ring-Stiffened Corrugated Cylinders represent a transformative structural approach that has emerged as a promising solution in our quest for enhanced structural integrity and performance, see figure 2.37. This innovative design incorporates strategically placed reinforcing rings within corrugated cylindrical structures, amplifying their ability to withstand external pressures significantly. Through rigorous calculations and simulations, we have determined that the strength-to-weight ratio of such structures is four times greater than that of simple cylinders. This remarkable enhancement not only bolsters our confidence in the structural reliability of our vacuum drum but also opens doors to novel design possibilities and operational efficiencies in a wide range of applications. The utilization of Ring-Stiffened Corrugated Cylinders exemplifies our commitment to pushing the boundaries of engineering innovation and achieving unparalleled strength and performance in our project (see [45] for details of the

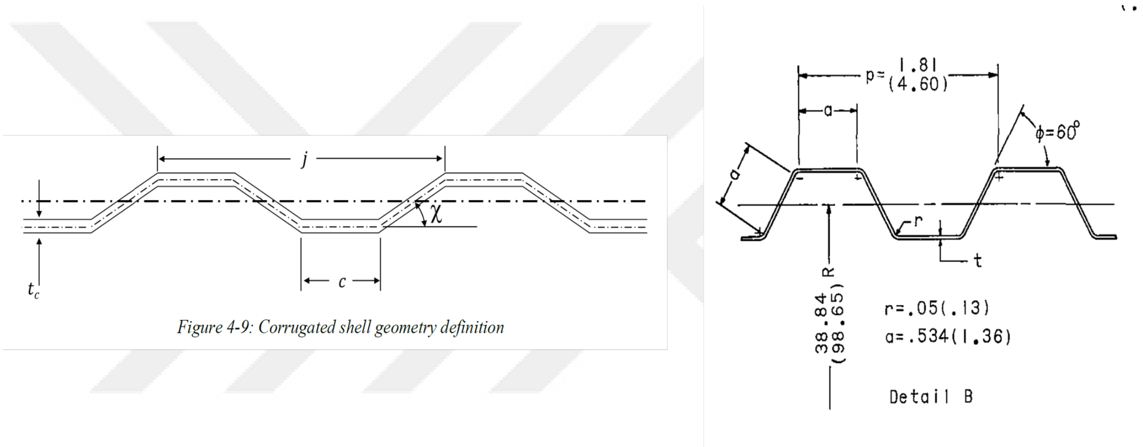

Figure 2.37: Corrugated shell details

calculation).

$$\begin{aligned} p_{cr} &\approx \frac{5.513}{Lr^{\frac{3}{2}}}\left[\frac{\bar{D}_y^3\left(\bar{E}_x\bar{E}_y-\bar{E}_{xy}{}^2\right)}{\bar{E}_y}\right]^{\frac{1}{4}} \\ E_x &= 253.3\text{MPa} \\ E_y &= 405.8\text{kPa} \\ D_y &= 11.9Pa \\ p_{cr} &= 3.8e5Pa = 3.8bar \end{aligned} \tag{2.4}$$

2.11.2 Vacuum Chamber Version 2

Thickness calculation

Determining the realistic sheet thickness is pivotal in achieving an optimal balance between structural strength and weight. Through meticulous calculations and simulations, we strive to ascertain the ideal sheet thickness that not only fortifies the drum but also minimizes unnecessary weight, enhancing the overall efficiency of our setup.

$$\begin{aligned} P_c =& \frac{Et}{r}\left(\frac{1}{n^2+\frac{1}{2}\left(\frac{\pi r}{l}\right)^2}\right)\left(\frac{1}{\left(n^2\left(\frac{l}{\pi r}\right)^2+1\right)^2}\right. \\ &\left.+\frac{t^2}{12\left(1-v^2\right)r^2}\left(n^2+\left(\frac{\pi r}{l}\right)^2\right)^2\right) \end{aligned} \tag{2.5}$$

Von Mises addressed the buckling behavior of cylindrical shells with closed ends when subjected to uniform hydrostatic pressure [46]. The resulting equation, which we have included in our report, reveals that the critical buckling pressure predominantly hinges on the vessel's geometry, particularly the ratio of thickness (t) to radius (r). Moreover, this critical pressure is directly proportional to the material's Young's modulus. The number of lobes (n), which are circumferential half-waves developed by buckling , is another important factor that influences the determination of critical pressure. A chart developed by Windenburg and Trilling [3], as illustrated in Figure 2.35 Number of lobes (n) in which the cylinder might collapse when subjected to uniform radial and axial pressure., offers valuable insights into how the number of lobes (n) varies with vessel geometry. Notably, it becomes apparent from the chart that as the shell's length and thickness decrease, the number of circumferential waves formed during buckling increases. For the geometry employed in our research, we anticipate a value of n to be approximately 8 based on our calculations. This value corresponds to the minimum critical buckling pressure, optimizing the structural performance of the shell under external pressures. Figure 2.38 is created using the critical buckling pressure by Von Mises. It shows critical pressures of a specific thickness (fixed drum radius). According to the Equation 2.5, we can have different critical buckling pressures for different number of lobes. This is also shown in the Figure as the x-axis of the plot refers to the number of lobes.

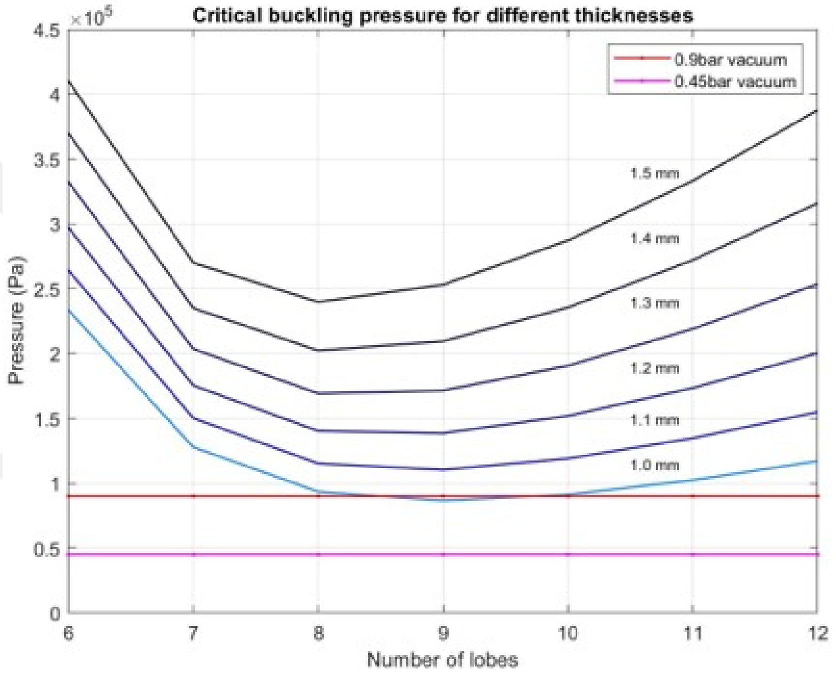

Figure 2.38: Critical buckling pressure as a function of number of lobes and sheet thickness.

It is essential to determine the safety factors for various scenarios to ensure the structural integrity and reliability of our design. These safety factors provide a quantitative measure of how much stronger the structure is compared to the expected loads and pressures it will encounter during its intended use. By conducting

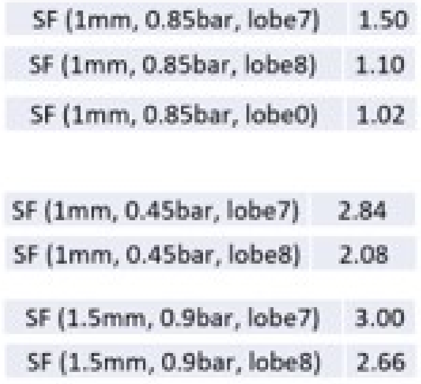

SF (1mm, 0.85bar, lobe7)	1.50
SF (1mm, 0.85bar, lobe8)	1.10
SF (1mm, 0.85bar, lobe0)	1.02

SF (1mm, 0.45bar, lobe7)	2.84
SF (1mm, 0.45bar, lobe8)	2.08

SF (1.5mm, 0.9bar, lobe7)	3.00
SF (1.5mm, 0.9bar, lobe8)	2.66

Figure 2.39: Corrugated shell details

these calculations, we gain valuable insights into the margin of safety and can confidently assess the performance of our design under different conditions. These safety factors are a crucial component of our comprehensive analysis, and they help guide our decisions to optimize the design for enhanced safety and reliability. Figure 2.39 Safety factors of different scenarios. graphically displays the results of our safety factor calculations for various scenarios, providing a clear visualization of the structural safety margins under different conditions.

Longitudinal and Circumferential Welds

Conducting a comprehensive welding analysis is essential to pinpoint critical areas within the drum's construction. By identifying these critical points, we can apply safety factors to reinforce welded edges. This rigorous analysis ensures that welding seams and joints are optimized for strength and durability, effectively reducing the likelihood of structural failure.

Careful management of welds is crucial in vacuum systems to prevent potential contaminants and flaws. Welds, necessary for mechanical resistance, should adhere to construction requirements. Stress levels are calculated with a reduction factor (0.85, 0.7), advising against localizing welds in high-stress areas. Guidelines must be followed in high vacuum chambers to prevent leaks and contamination. Trapped volumes between two welds are not permitted; welding should be done on the vacuum side. It is not advisable to use filler metal, and grooves can aid in later cutting and rewelding while reducing heat spread. Defects, such as bath remelting from crossing welds, can arise if these considerations are not carefully observed.

Simulations

To gain deeper insights into the structural behavior of our drum and validate our design improvements, we have sought assistance from Finite Element Method (FEM) analysis using specialized software. FEM analysis enables us to simulate and assess various stress scenarios, allowing for data-driven refinements to our design, which in turn bolster the drum's structural resilience. In our quest to enhance the structural integrity of our vacuum drum, we rigorously evaluated several design enhancements, each with its own unique characteristics and potential for bolstering performance. The structural configurations we examined included:

1. Simple Cylinder (1 mm Thickness): This represented the baseline design with a relatively thin wall.

2. Simple Cylinder (1.5 mm Thickness): An incremental increase in thickness from the baseline, aimed at reinforcing the structure.

3. Stringer – 74 mm: The introduction of stringers, strategically positioned, with a 74 mm spacing to provide additional support.

4. Stringer – 25 mm: A variation of the stringer design with a narrower spacing of 25 mm, potentially increasing structural rigidity.

5. External Rings (3x20 mm): This design combined the benefits of stringers with the inclusion of external rings, offering a multifaceted approach to structural reinforcement.

By referencing Table 2.1, we gain valuable insights into how each enhancement influences the structural behavior of the vacuum drum under varying conditions,

Table 2.1: Table of properties and results achieved through simulations.

Drum Type	Thickness	Buckling Pressure	Mass of Drum
Simple Cylinder	1.0 mm	0.84 bar	10 kg
Simple Cylinder	1.5 mm	2.5 bar	14.5 kg
Stringer -74 mm	1.0 mm	3.5 bar	11.3 kg
Stringer -25 mm	1.0 mm	10.5 bar	13 kg
External Rings (3 × 20 mm)	1 mm	3.74 bar	11.1 kg

also shown in Figure 2.40. This data-driven approach empowers us to make informed decisions regarding the optimal design configuration to ensure both safety and reliability in our vacuum experiments.

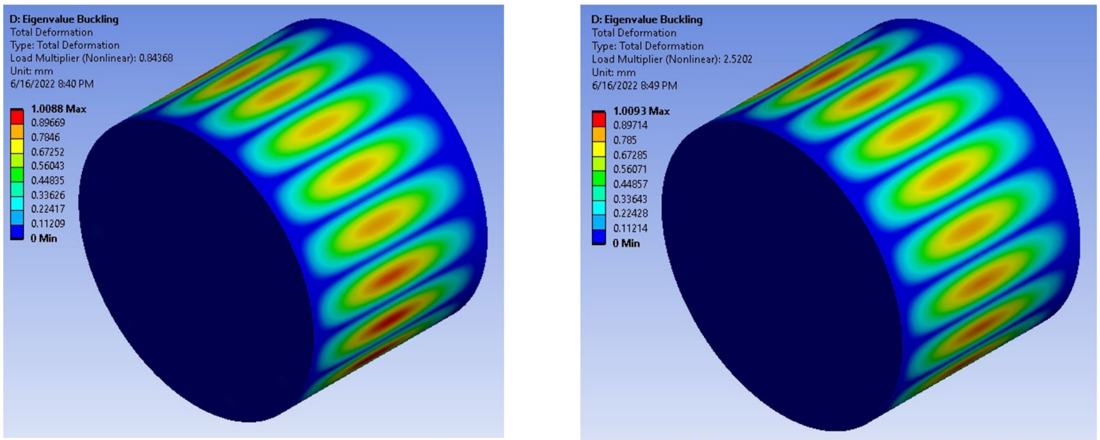

Thickness: 1 mm, mass 10 kg, Buckling load 0.84 bar

Thickness: 1.5 mm, mass 14.5 kg, Buckling load 2.52 bar

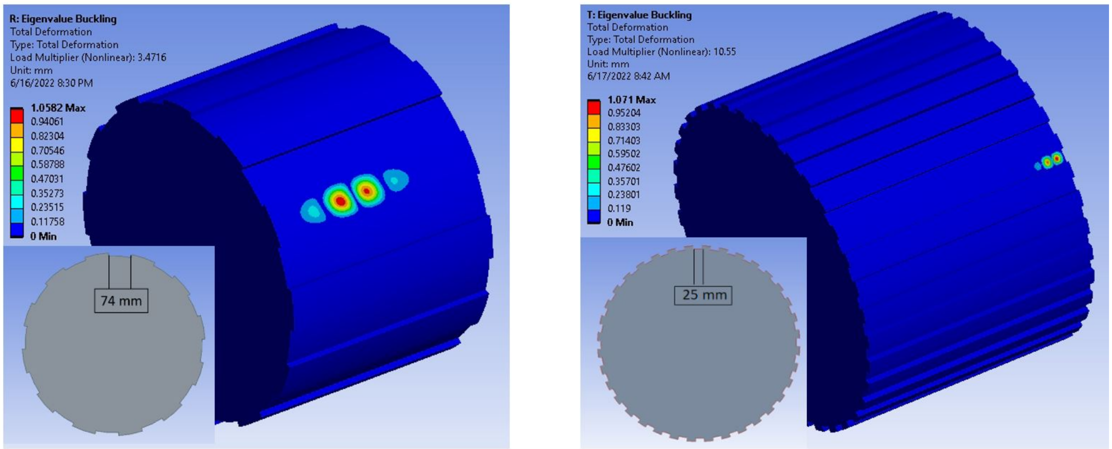

Thickness: 1 mm, mass 11.3 kg, Buckling load 3.5 bar

Thickness: 1 mm, mass 13 kg, Buckling load 10.5bar

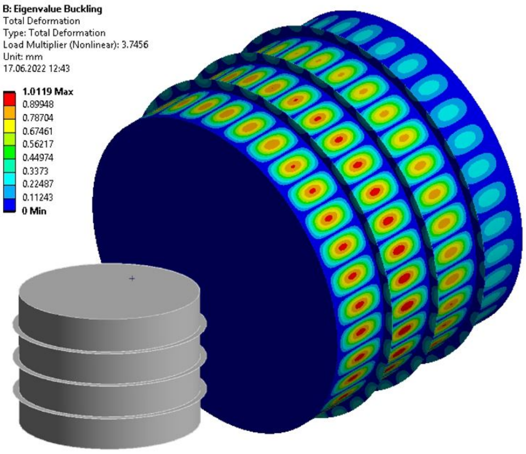

Thickness: 1 mm, mass 11.1 kg, Buckling load 3.7 bar

Figure 2.40: The simulation results for different structural enhancements

2.11.3 Vacuum Chamber Version 3

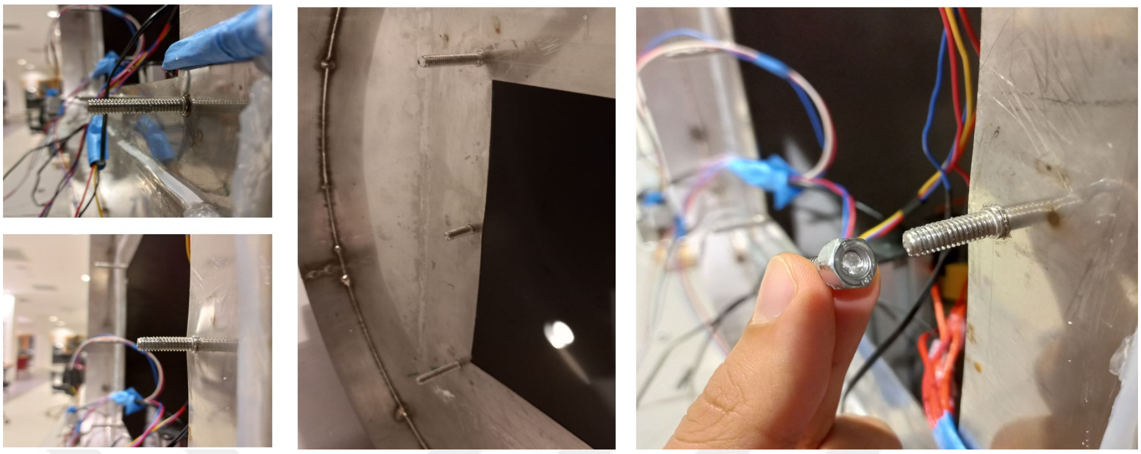

Figure 2.41: Model 2 issues - fracture of bolts welded to the drum.

The decision to revise the opening and closing mechanism for our third model stemmed from valuable insights gained through the experience of the previous designs. In models 1 and 2, we employed a mechanism that involved nuts and bolts, utilizing a thick sheet plate coated with silicon to create a seal. While this approach initially provided a secure seal, it presented challenges over time (see figure 2.41). The time required for opening and closing the drum was considerably high, impacting operational efficiency. Moreover, after a certain number of usage cycles, the bolts exhibited signs of fracture, and the threads became unusable, necessitating frequent maintenance.

To address these issues and streamline the operation, we introduced a novel door mechanism for the third model, shown in figures 2.42 and 2.43. The area of the opening remained consistent with the previous designs to maintain compatibility with existing components. Notably, we implemented twelve latches, strategically spaced at 8.5 cm intervals, to secure the door firmly in place. This latch-based approach significantly reduced the time required for opening and closing, enhancing the overall efficiency of our setup. In addition to the latch system, we incorporated three circular O-rings into the design. These O-rings, made from EPDM (Ethylene Propylene Diene Monomer), were carefully chosen for their sealing properties. Their

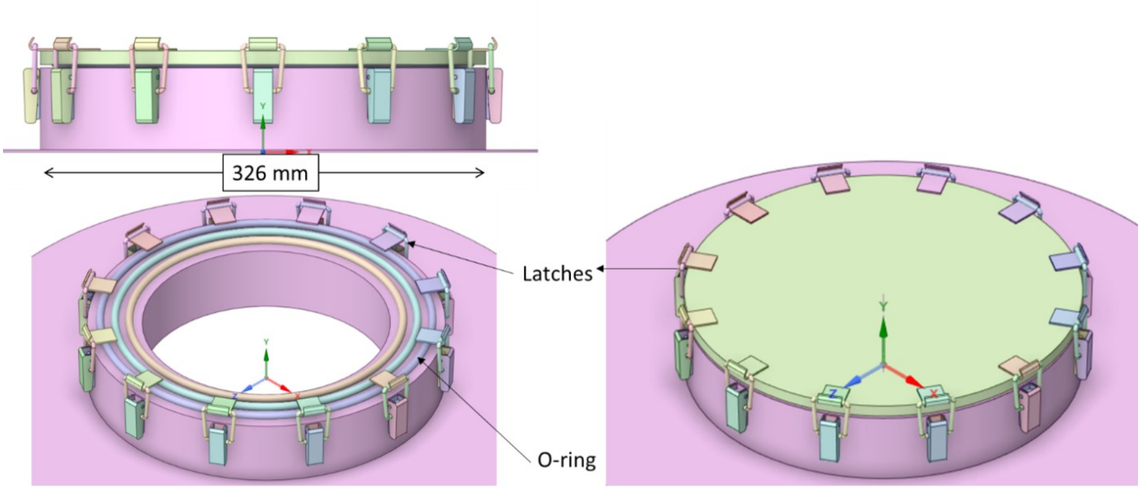

Figure 2.42: New design for the drum opening and closing mechanism.

compression was optimized to be 30% of the diameter of the ring, ensuring a reliable and airtight seal when the door is closed. These thoughtful revisions to the opening and closing mechanism not only enhance the operational efficiency of our vacuum drum but also address the maintenance and durability concerns encountered in earlier models. By implementing these improvements, we are poised to achieve greater reliability and performance in our vacuum experiments, ensuring the success of our research endeavors.

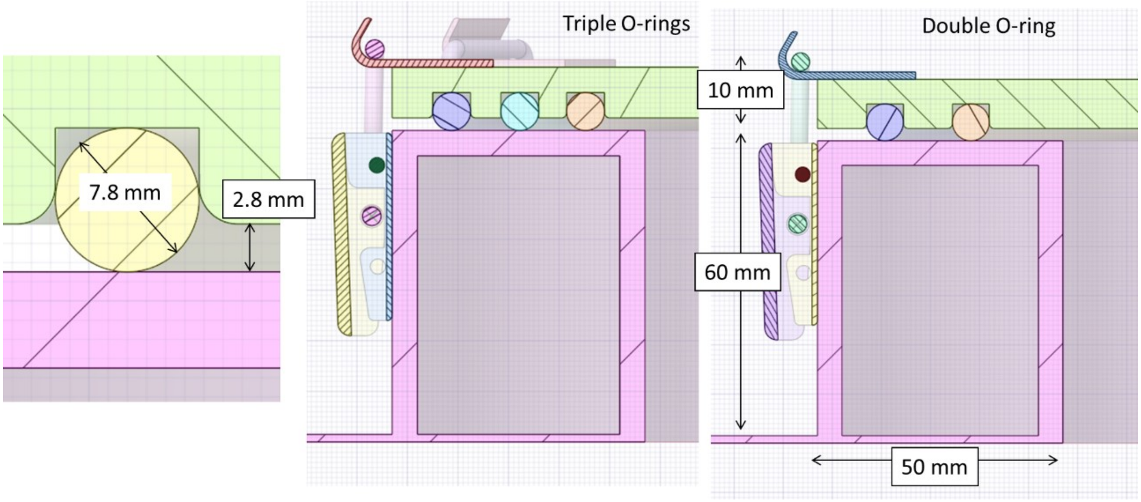

Figure 2.43: Cross section view of the design

2.12 Vacuum dryer experimental setup

In the report, we present a comprehensive overview of the designed experimental setup that forms the core of our research endeavors. The schematic representation of this setup is illustrated in Figure 2.44, highlighting the interplay of three central units that collectively contribute to the successful execution of our experiments: (a) Vacuum Unit, (b) Heating Unit, and (c) Control Board Unit.

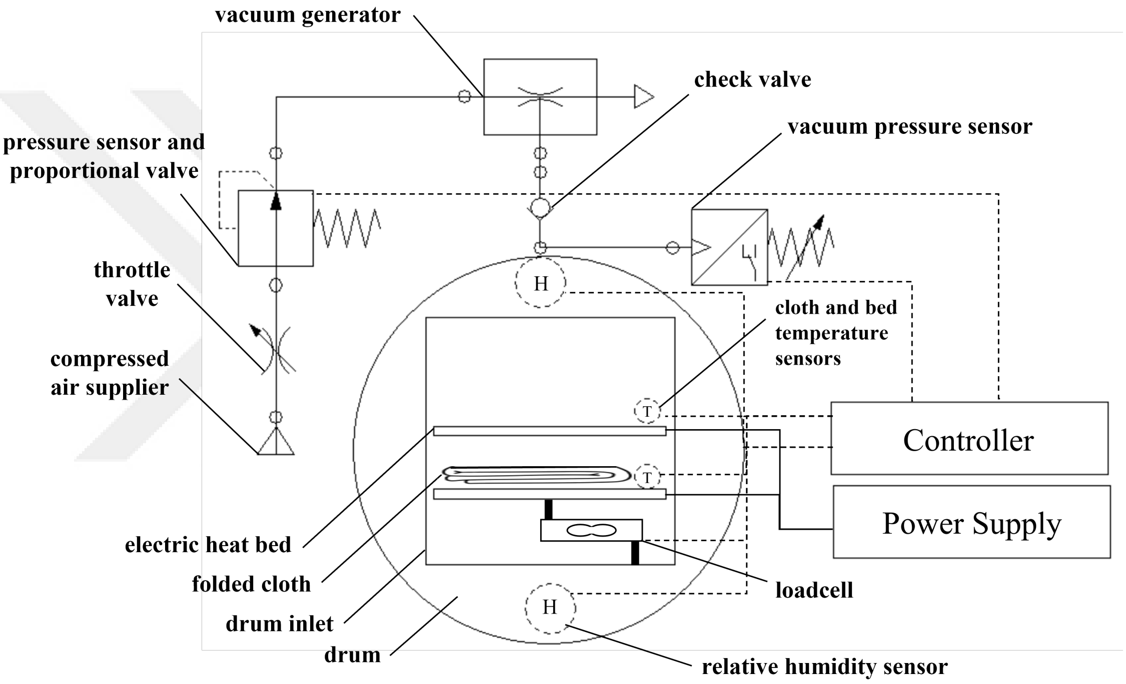

Figure 2.44: Schematic of the vacuum assisted dryer setup.

2.12.1 Vacuum Unit

This critical component of our setup is engineered to withstand vacuum conditions, comprising a vacuum-resistible drum, a vacuum generator, and a proportional valve. The vacuum generator plays a pivotal role in creating and maintaining the desired vacuum levels within the chamber, while the proportional valve ensures precise control over the vacuum process (see figure 2.45).

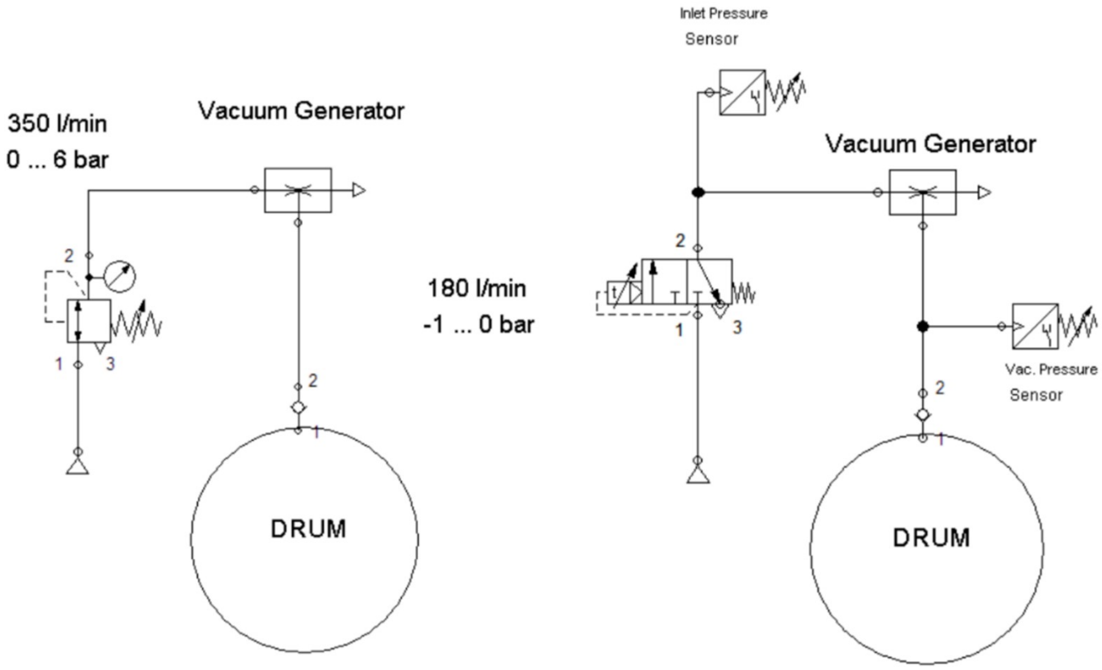

Figure 2.45: Vacuum unit flowchart.

2.12.2 Heating Unit

The heating unit is instrumental in regulating temperature within the vacuum chamber. It features two horizontal heat beds, positioned 70 mm apart, facilitating uniform heat distribution. These beds, with a combined thermal power of 120W and a contact area of 625 mm2, enable precise control over the drying process.

2.12.3 Control board

Our setup incorporates an advanced control system operated by an Arduino Mega microcontroller, figure 2.46. This controller dynamically manages the internal pressure and temperature of the chamber during experiments, ensuring optimal conditions for the drying process. To collect and capture vital data, various sensors, including temperature, humidity, and pressure sensors, interface with the controller.

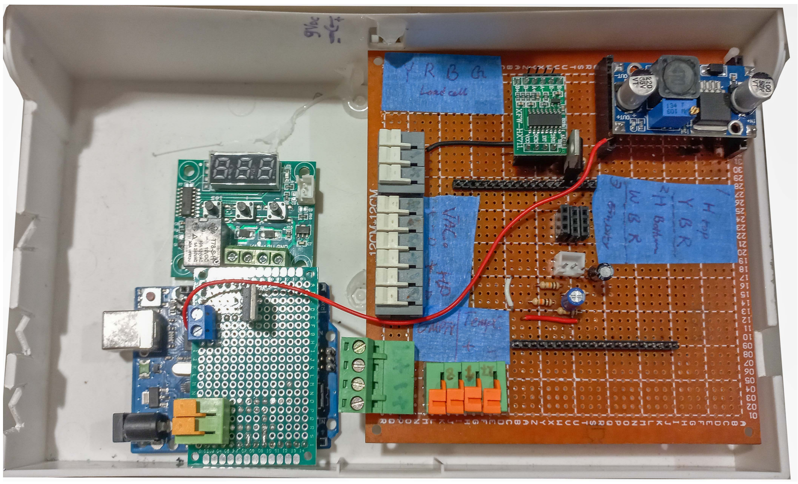

Figure 2.46: The control board of the setup

2.12.4 Data Acquisition

The control system, powered by the Arduino Mega microcontroller, not only orchestrates the setup's operation but also serves as the central hub for data acquisition. It utilizes the wealth of data provided by the integrated sensors to make real-time adjustments, optimizing the drying process and ensuring consistent and reliable experimental outcomes. The Putty software is utilized to record and collect data on a computer connected via USB cable to the control board.

2.12.5 Weight measurement

To monitor the reduction in weight of drying samples with precision, we've incorporated a strain gauge load cell with an accuracy of ±1 g. This load cell (shown in figure 2.47), operating at a rate of 2 Hz, delivers accurate measurements, further enhancing the reliability of our experimental data. Accurate and real-time weight measurement plays a pivotal role in the success of our project, especially when dealing with the drying of textiles. The mass of the wet textile sample is a critical parameter that undergoes continuous change throughout the drying process. Monitoring this mass with precision, uncertainty reduction, and repeatability is of paramount importance. Firstly, it allows us to track the drying progress with the utmost accuracy, ensuring that we capture subtle changes in the textile's moisture content. This precision empowers us to determine the optimal drying point while minimizing energy consumption and processing time.

In our setup, the concept of load cells equipped with strain gauges forms the cornerstone of our weight measurement system. These load cells operate on the principle of the Wheatstone bridge, where strain gauges are employed to detect minute changes in mechanical deformation caused by the weight of the textile sample. By strategically positioning these strain gauges within the load cell's structure, we create a highly sensitive and reliable system capable of translating the mechanical strain into a measurable electrical signal. The Wheatstone bridge configuration allows us to precisely measure the resistance change in the strain gauges, directly correlating it with variations in weight. This innovative approach ensures that our weight measurements are not only accurate but also provide a high degree of repeatability and reliability, allowing us to extract valuable insights into the drying process and optimize our experiments effectively.

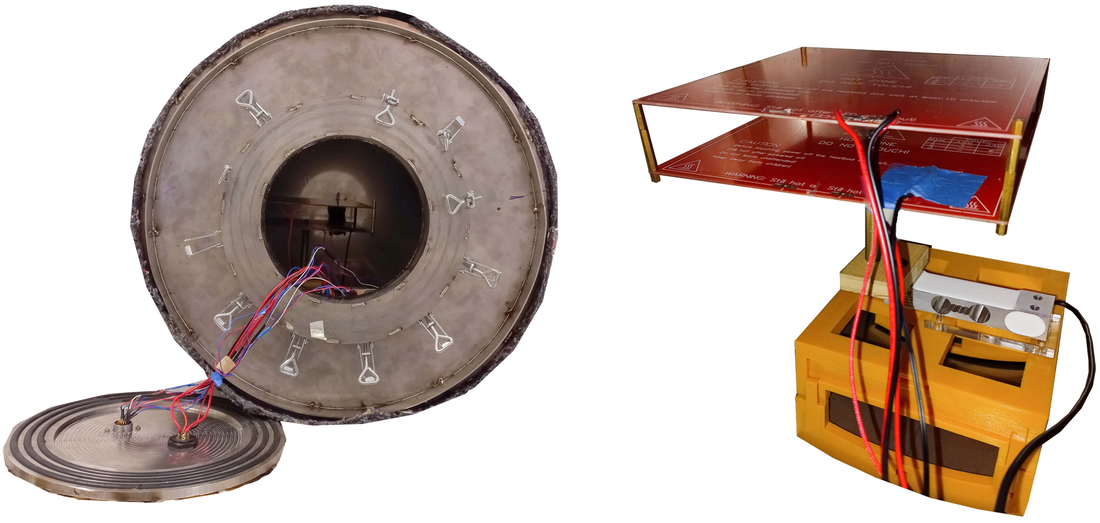

(a) (b)

Figure 2.47: The experimental setup: (a) the vacuum chamber, (b) the heaters and loadcell assembly

The Wheatstone bridge is a fundamental electrical circuit that plays a crucial role in measuring the resistance change in strain gauges, enabling us to convert mechanical deformation into a quantifiable electrical signal. The Wheatstone bridge consists of four resistors arranged in a diamond configuration, with a voltage source applied across the top and bottom nodes and a galvanometer connected between the side nodes. When the bridge is balanced, meaning that the ratio of resistances on one side is equal to the ratio on the other side, no current flows through the galvanometer, and it remains at zero. However, when a strain gauge within the bridge experiences deformation due to a load, its resistance changes, disrupting the balance of the bridge. As a result, a voltage difference emerges across the galvanometer, producing a measurable electrical signal. By precisely measuring this voltage change, we can determine the extent of mechanical strain on the load cell and thus accurately calculate the applied force or load. The Wheatstone bridge configuration provides high sensitivity and accuracy in resistance-based measurements, making it an indispensable tool in load cell technology and a cornerstone of precise force and load measurement systems.

Sensor integration

Our experimental setup is equipped with an array of sensors and heaters, shown in table 2.2, each playing a critical role in ensuring the precision and control of our vacuum drying experiments. These sensors capture essential data, enabling real-time monitoring and data-driven decision-making throughout the experimental process.

Notably, we have pressure sensors that sample data at a remarkable rate of 1 kHz. These sensors are instrumental in monitoring vacuum pressure and inlet pressure within the chamber, offering an exceptionally high-frequency data stream that allows us to capture rapid changes in pressure dynamics. It is important to note that we will delve deeper into the intricacies of pressure sensors in the upcoming section of our report, providing a comprehensive analysis of their significance and operation. Our setup incorporates a relative humidity sensor with a sampling rate of 0.5 Hz (see figure 2.48). This sensor provides valuable insights into the moisture

Table 2.2: Sensors and Heaters in the Experimental Setup.

Sensor	Brand	Model/ Accuracy	Sampling rate	Measurement method	Notes
Vac. pressure	Festo	SPTW-B2R-G14-VD-M12 1 % FS	1 kHz	Piezoresistive	$-1 \sim 1$ bar Relative pressure
Inlet pressure	BAUMER	PBMN-24B27AA ±0.25% FSR	1 kHz	Piezoresistive	$0 \sim 40$ bar stainless steel housing
Relative Humidity	AOSONG	DHT21 ±1.8% AM2301	0.5 Hz	Capacitive sensing	Temp. $-40 \sim 123.8^{\circ}C$
Heater temp.	SZYTF	100k NTC ±1%	1 Hz	thermistor	Waterproof
Sample temp.	SZYTF	10k NTC ±1%	1 Hz	thermistor	Waterproof
Drum temp.	AOSONG	DHT22 ± 2%	0.5 Hz	Polymer capacitor	Temp $-40 \sim 80^{\circ}C$
Heater	MK2A	Reprap Ramps v1.4	120 w	-	Input:12-24v $214 * 214\ mm$ Double-sided Red Mask
Micro controller	Arduino	Mega	150 Hz	-	-

content of the chamber's atmosphere, offering crucial data for assessing the drying process's effectiveness and humidity control. Temperature monitoring is crucial in our experiments, and we have strategically positioned sensors to capture temperature data at a rate of 1 Hz. These sensors track the temperature of various critical components, including the heater, water, and the vacuum drum itself. The data from these sensors allows us to maintain precise temperature control and optimize the drying process for consistent and reliable results.

Our heating unit features a 120W heater, which plays a pivotal role in maintaining the desired temperature within the vacuum chamber. The precise control of this heater ensures that the drying process occurs under controlled and uniform thermal conditions, a critical factor in textile drying experiments. The central control unit of our setup is powered by an Arduino microcontroller, sampling data at a rate of 150 Hz. This Arduino controller acts as the brain of our system, orchestrating sensor data acquisition and making real-time adjustments to chamber pressure and temperature to optimize the drying process. The integration of these sensors and heaters in our setup represents a sophisticated and well-coordinated effort to create a controlled and data-rich environment for our vacuum drying experiments. These components collectively empower us to monitor, adjust, and analyze critical parameters, contributing to the success and precision of our research.

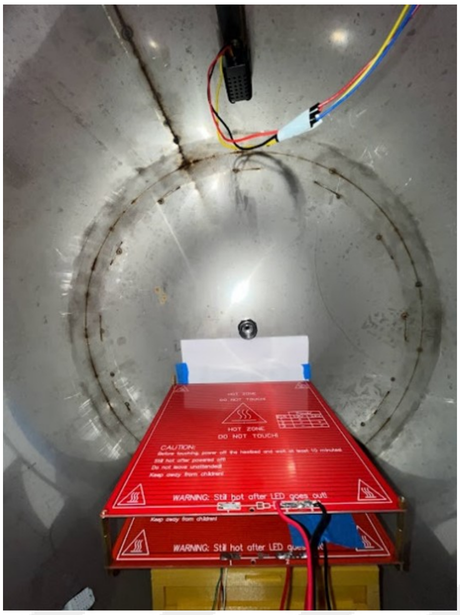

Figure 2.48: The heaters and humidity sensor location inside the vacuum drum.

Pressure transmitter

In our experimental setup, we have employed Festo SPTW-B2 pressure sensors, which prove to be essential components for monitoring and maintaining precise pressure conditions within the vacuum chamber. These pressure sensors come in two versions: piezoresistive pressure sensors and metal thin-film pressure sensors, both designed to measure relative pressure accurately.

One notable feature of the SPTW-B2 pressure sensors is their versatility, as they are suitable for measuring both liquid and gaseous media. This adaptability allows us to utilize these sensors effectively across a range of experimental conditions and applications. The pressure measuring cell and interfaces of these sensors are constructed from stainless steel, rendering them seal-free. This design choice enhances their durability and reliability, as it eliminates the risk of potential leaks or damage to the pressure measuring cell and interfaces.

These pressure sensors boast an IP67 protection rating, which signifies their resistance to dust and moisture ingress. This level of protection is particularly valuable in our setup, where maintaining a controlled environment is crucial for the success of our vacuum experiments. The SPTW-B2 pressure sensors offer a wide pressure measuring range from -1 bar to +1 bar, making them well-suited for our application. They operate on a voltage range of 8 to 30 V DC and feature a pneumatic connection with a G1/4 thread. To facilitate their integration into our setup, these pressure sensors come with a convenient electrical connection in the form of a 4-pin plug with an M12x1 thread, designed to meet EN 60947-5-2 standards. This round design ensures compatibility and ease of installation within our system. The inclusion of SPTW-B2 pressure sensors in our setup is integral to our ability to monitor and control pressure conditions with precision, ensuring the reliability and success of our vacuum experiments

2.13 Initial tests

2.13.1 Testing the Festo Vacuum Generator

In our experimentation to assess the performance of the Festo vacuum generator, shown in figure 2.49, we employed a systematic approach to comprehensively evaluate its functionality. To provide the vacuum generator with an inlet pressure source, we utilized a 6 bar pressurized air supply, readily available within the MARC laboratory. Our objective was to validate the vacuum generator's capabilities and compare its performance with the data provided in its documentation files. To achieve this, we deployed two critical sensors to capture essential data points. Firstly, we employed a vacuum pressure sensor with a specified range of -1 to 1 bar to measure the vacuum generated by the Festo vacuum generator. Secondly, we used a pressure sensor

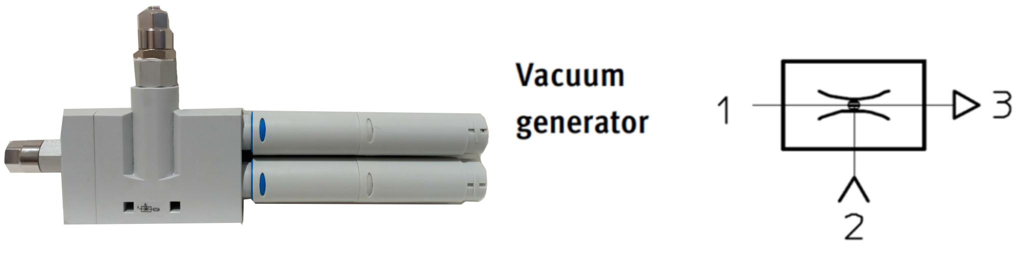

(a) (b)

Figure 2.49: Festo vacuum generator: (a) with noise reducer, (b) schematic of the vacuum generator; 1. inlet, 2. outlet, 3. vacuum.

capable of monitoring pressures within the range of 1 to 10 bar to measure the inlet pressure that we supplied to the vacuum generator. The key focus of our assessment involved plotting the vacuum generated as a function of the inlet pressure. In figure 2.50, which we have included for reference, showcase two sets of data: one derived from the product manual of the Festo vacuum generator and the other representing our test results. It is important to note that during our testing, the vacuum line of the generator was directly connected to the sensor for the sake of measurement. It is crucial to emphasize that the performance of the vacuum generator may vary when connected to the vacuum drum of our experimental setup, as it encounters different operational conditions. By conducting this comprehensive evaluation and providing visual representations of the data, we aim to offer a clear understanding of the Festo vacuum generator's performance characteristics, its response to varying inlet pressures, and how these factors may influence its functionality within the context of our vacuum drying experiments.

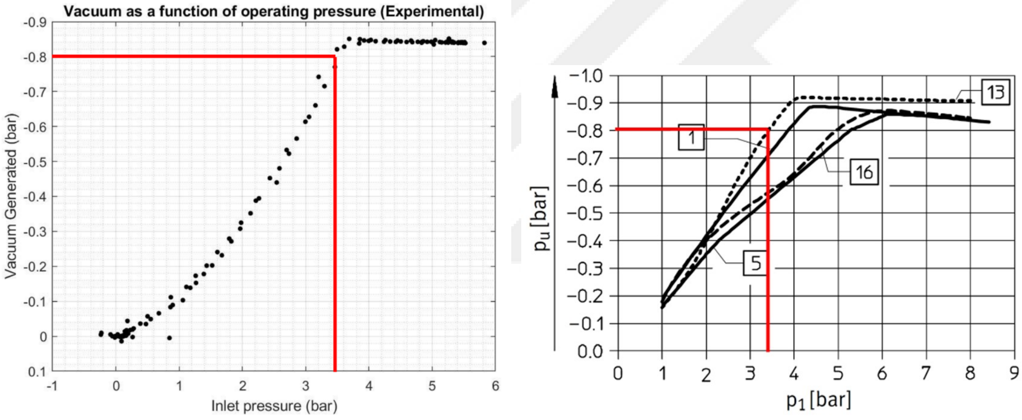

(a) (b)

Figure 2.50: Vacuum generator performance, plot of vacuum over inlet pressure: (a) laboratory test, (b) Festo documentation.

2.13.2 Dew on Walls

During our preliminary tests, a noteworthy observation was made concerning the recondensation of evaporated water from the sample on the internal surface of the drum (see figure 2.51). This phenomenon can be attributed to several contributing factors that we have identified and aim to address for improved experimental results. First, the material composition of the drum, which is constructed from stainless steel, plays a significant role. The temperature differential between the internal surface of the drum and the surrounding environment creates conditions conducive to condensation. To mitigate this effect, we are considering the incorporation of an isolator layer within the drum's design. This additional layer would serve to protect the internal surface, minimizing the temperature differential, and reducing the potential for rewatering. Secondly, an important aspect is the substantial difference in temperature between the internal layer and the environment layer of the drum. This temperature gradient can lead to moisture condensation on the drum walls. To counteract this, we are exploring the implementation of an isolator layer, which would contribute to a more uniform temperature distribution within the drum, reducing the likelihood of recondensation. Another significant contributor to this issue is the increase in absolute internal humidity during constant vacuum drying, see figure 2.52. As the moisture content within the chamber rises, the air within the drum reaches a saturation point, leading to condensation on the walls. To address this, we are actively researching ways to enhance the moisture

Figure 2.51: Water condensation on internal surface of drum

handling capacity of the drum's internal environment, allowing us to better manage and control humidity levels during the drying process. By addressing these factors comprehensively, we aim to minimize the recondensation of evaporated water within the drum, ensuring more accurate and efficient vacuum drying experiments while enhancing the reliability of our results.

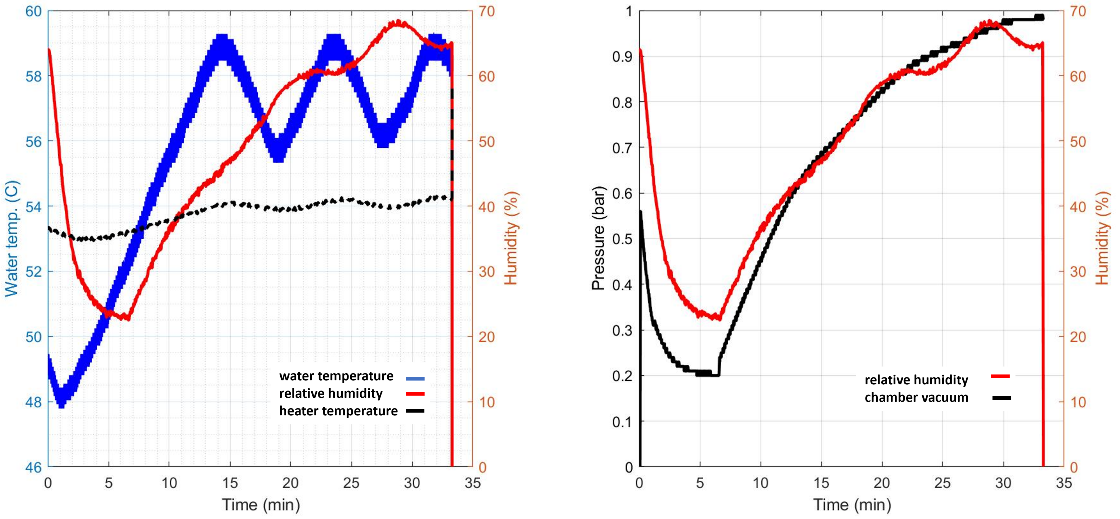

Figure 2.52: Preliminary results - water evaporation inside chamber.

2.13.3 Vacuum Control and Valve Selection

Precise control of vacuum conditions within the chamber is a fundamental requirement for our experiments. Initially, we implemented on-off valves for vacuum control. However, as we progressed and considered factors like leakages and the functionality of our vacuum generator, we made a strategic shift to proportional valves. These proportional valves provide fine-tuned control over the vacuum level, allowing us to maintain the desired pressure with a high degree of accuracy. This decision aligns with our commitment to optimizing the performance and reliability of our vacuum experiments.

2.13.4 Heat Transfer Mechanisms and Heater Selection

In a vacuum environment, traditional heat transfer mechanisms like convection are limited, leaving us primarily with conduction and radiation. To explore these heat transfer modes, we carefully selected our heaters. Heat beds were chosen to test conduction-based heat transfer, ensuring that the temperature within the chamber remains uniform and controlled. Additionally, we are considering the use of infrared heaters to investigate radiation-based heat transfer, offering a versatile approach to managing thermal conditions within the chamber. This thoughtful selection of heat transfer mechanisms and heaters reflects our dedication to achieving optimal drying conditions.

2.13.5 Increasing Evaporation Rate

To enhance the evaporation rate of the drying process, we've adopted a multifaceted approach. Firstly, we are focused on increasing the heat transfer rate within the chamber, as elevated temperatures accelerate the moisture evaporation. Secondly, we're exploring ways to maximize water surface area exposure within the chamber, optimizing the interaction between heat and the textile sample. Finally, we aim to raise the internal temperature of the drum, creating an environment conducive to rapid moisture evaporation. When these aspects are collectively addressed, we aim to achieve significant improvements in the evaporation rate, expediting the drying process, and enhancing its efficiency.

2.13.6 Wire Leakages

An issue we encountered during the course of our experiments was wire leakage, particularly from the sensors' wires coming out of the drum through the opening of the door. This observation has prompted us to consider wire management as a critical aspect in the design of future drum iterations. Finding solutions to mitigate these leakages is essential to ensure the integrity of our experiments and the reliability of our data. This valuable information will guide our efforts to refine the design of the drum for future models, underscoring our commitment to continuous improvement and innovation. These considerations and decisions underscore our dedication to achieving precise control, efficient heat transfer, and reliable data acquisition in our vacuum drying experiments, ultimately contributing to the success of our research.

2.13.7 Energy calculation

The process of textile drying and water evaporation within our experimental setup involves several sources of heat transfer, each contributing to the overall energy requirements of the system. Understanding and quantifying these sources of heat is vital for optimizing our drying process and ensuring efficient resource utilization.

- Sensible Heat: Sensible heat refers to the heat transfer associated with changes in temperature. In the context of textile drying, it accounts for the energy required to elevate the temperature of both the textile sample and the surrounding air within the vacuum chamber. As we heat the air and the textile, they gain thermal energy, which in turn accelerates the moisture evaporation process.

- Latent Heat: Latent heat is the energy absorbed or released during phase transitions, such as the conversion of liquid water into water vapor. In textile drying, this heat source is of paramount importance as it represents the energy consumed during the actual evaporation of water from the textile sample. The latent heat of vaporization is a significant contributor to the overall energy demand, especially when dealing with moisture removal.

- Clothes Heating: Clothes heating accounts for the energy required to raise the temperature of the textile sample itself. As the textile absorbs thermal energy, it reaches a point where moisture begins to evaporate, a process that necessitates the latent heat mentioned earlier. This energy input is crucial for effective drying and moisture removal from the textile.

- Air Heating: Heating the air within the vacuum chamber is another energy-intensive aspect of our drying process. Elevated air temperatures enhance its capacity to hold moisture, facilitating faster evaporation rates. The energy invested in heating the air directly contributes to the drying efficiency.

Mass of wet clothes $= 12.8kg$

$$Q_{total} = \text{Sensible Heat} + \text{Latent Heat} + \text{Clothes Heating} + \text{Air Heating} \tag{2.6}$$

$$= 237.12 + 12408 + 278.72 + 4.85 = 12928.69kJ$$

The calculations shown in the 2.6 are deviated based on the assumptions explained in section 2.4. These values are calculated using thermodynamic properties of moist air based on Psychrometric Chart. In addition to these sources of heat, It is important to consider the energy requirement of the compressor used to create and maintain the vacuum within the chamber. The compressor energy requirement is a crucial component of our energy calculations, as it directly impacts the vacuum generation process and, subsequently, the drying efficiency.

Chapter 3

THEORETICAL BACKGROUND AND SIMULATIONS

Simulation has emerged as an indispensable tool in modern scientific research and engineering, enabling us to explore complex phenomena, optimize processes, and gain deeper insights into intricate systems. In the context of our project, which focuses on vacuum-assisted drying of textile samples, simulation plays a pivotal role in exploring the underlying physics, enhancing our experimental design, and guiding us toward more efficient drying methods. In this chapter, we demonstrate three distinct simulation models developed to connect our experimental work and theoretical knowledge.

3.1 Simulation Objectives and Scope

Our primary goal in utilizing simulations is to gain valuable insights into the complex process of drying, with a specific focus on understanding how moisture content evolves within the sample over time. To achieve this goal, we aim to obtain a comprehensive understanding of the intricate dynamics governing the drying process, particularly the instantaneous rate of evaporation and the changing weight of the wet sample. Simulations provide us with a powerful tool to dissect these phenomena, offering the ability to explore and quantify the moisture content of the sample as a function of time. This detailed information is invaluable for optimizing drying processes, enhancing efficiency, and ultimately achieving the desired drying outcomes while conserving energy and resources. Through our simulation efforts, we bridge the gap between theory and practice, allowing us to make informed decisions and refine our drying techniques for the benefit of various industries and applications. Indeed, determining the moisture content of the sample as it evolves over time during the drying process is a critical aspect of our research. Simulation serves as a valuable tool in this pursuit by enabling us to analyze the instantaneous rate of evaporation and monitor the changing weight of the wet sample, as shown in Figure 3.1. At the heart of our simulation efforts lies COMSOL Multiphysics, a robust finite element analysis software package. COMSOL empowers us to create comprehensive multiphysics models that can capture the intricate interplay of various physical phenomena, a critical requirement for simulating the vacuum-assisted drying process of textile samples. This software's capability to seamlessly integrate multiple physics interfaces, coupled with its user-friendly interface, aligns perfectly with our objectives. Through the course of this chapter, we'll showcase how this software has been instrumental in advancing our understanding of the drying process, optimizing our experimental parameters, and generating valuable insights that drive our research forward.

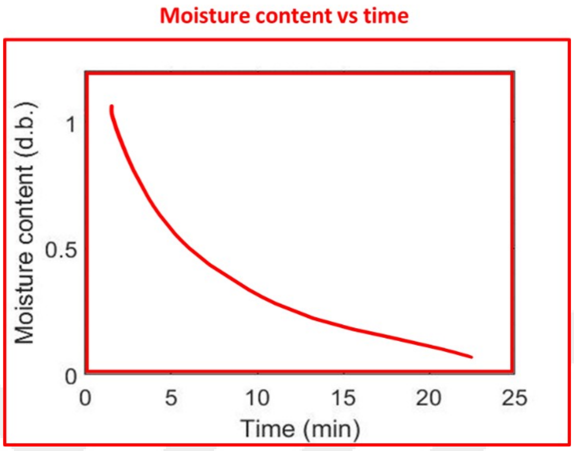

Figure 3.1: Schematic plot of sample moisture content (dry based calculated) over time during the drying.

Our simulations was guided by extensive research and a thorough investigation of existing literature and models related to drying processes. We understood the insights and findings of previous researchers, while also incorporating innovative elements that are specific to our vacuum-assisted drying setup. In this chapter, we'll draw upon this amalgamation of knowledge to outline the foundations of our simulation models and illustrate how they fit seamlessly into the broader context of drying research. As we embark on our exploration of the simulation models, it is essential

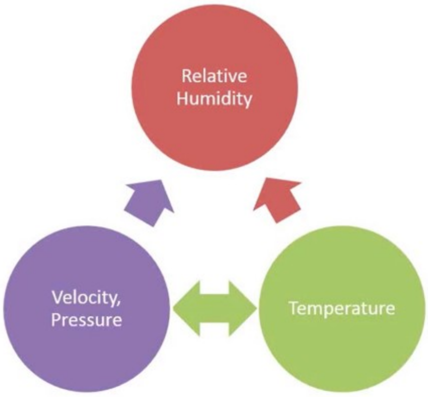

Figure 3.2: Key variables that underpin the dynamics of drying.

to understand the key variables (figure 3.2) that underpin the intricate dynamics of drying, shown in Figure 3.3. These variables encompass relative humidity, velocity and pressure, and temperature. Their interplay dictates the behavior of moisture within the textile sample, influencing evaporation rates, drying times, and overall drying efficiency. Throughout this chapter, we'll dissect these variables and elucidate their roles in shaping our simulation outcomes.

This chapter offers a comprehensive view of the computational efforts that complement our experimental work in vacuum-assisted drying. By combining the power of COMSOL Multiphysics and MATLAB, prior research insights, and an in-depth analysis of key variables, we aim to provide an understanding of the drying process under vacuum.

3.2 Fundamentals of simultaneous heat and mass transfer

Simultaneous heat and mass transfer is a fundamental phenomenon that lies at the core of the drying process. It represents the dynamic interplay between the transfer of thermal energy and the movement of moisture within a material undergoing drying. As a textile sample is exposed to elevated temperatures during the drying process, the heat input initiates the absorption of thermal energy, raising the material's temperature. Concurrently, this increase in temperature induces the evaporation of moisture from the sample. This simultaneous heat and mass transfer

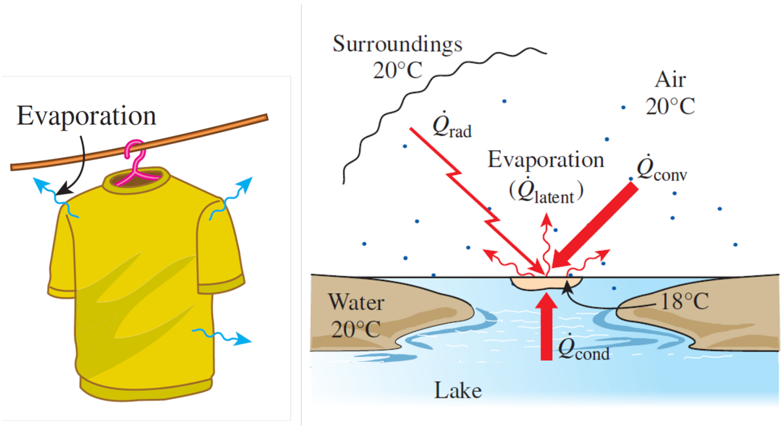

Figure 3.3: Comparison of evaporation heat transfer in wet textile and lake water.

results in a dynamic equilibrium where energy is continually supplied to the material, facilitating the phase change of liquid water to water vapor. Understanding and quantifying this intricate coupling of thermal energy and moisture movement is essential for optimizing drying processes, as it directly influences drying rates, energy consumption, and the final quality of the dried product. In the context of our research, unraveling the complexities of simultaneous heat and mass transfer is a key focus, and our simulation models play a crucial role in elucidating the underlying dynamics for more efficient vacuum-assisted textile drying.

3.2.1 Liquid Vaporization

The vaporization of a liquid, whether occurring under normal convection, forced convection, or within a vacuum environment, presents intriguing variations in the dynamics of phase change. Under normal convection, where a liquid is exposed to ambient conditions, vaporization typically occurs at the liquid's surface as it absorbs thermal energy from the surroundings. This process is influenced by factors such as temperature, pressure, and the properties of the liquid, leading to varying rates of vaporization.

In forced convection, where external forces like airflow or mechanical agitation are applied, the vaporization process gains momentum. Enhanced heat transfer mechanisms accelerate the rate of vaporization, making it more efficient and allowing for

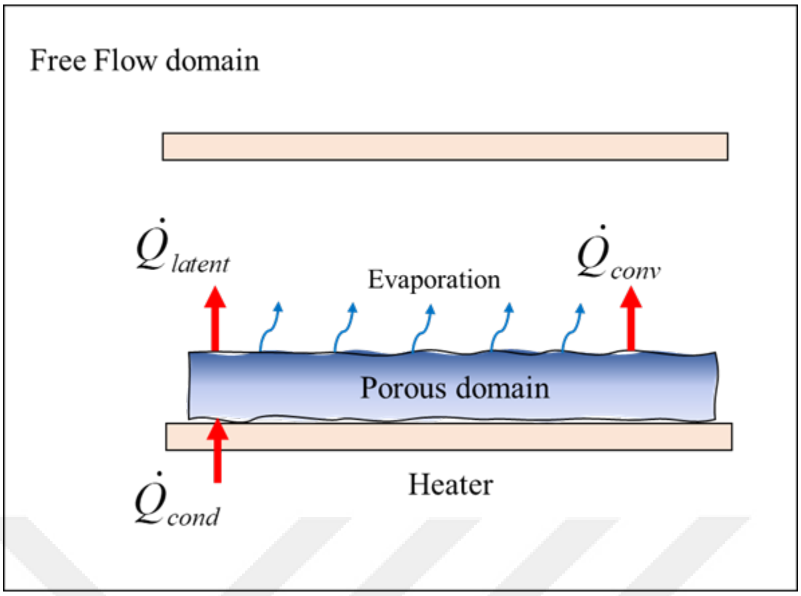

Figure 3.4: Main elements of heat and mass transfer in textile drying simulation.

faster moisture removal. Forced convection is often harnessed in industrial drying processes to expedite the evaporation of liquids. Conversely, the scenario takes a markedly different turn when vaporization transpires under vacuum conditions (see figure 3.4). In this environment, the reduced pressure significantly lowers the boiling point of the liquid, causing it to vaporize even at relatively low temperatures. This is particularly advantageous in processes like vacuum drying, where the goal is to remove moisture from materials without subjecting them to excessive heat, preserving their quality. Understanding these distinct vaporization dynamics in different settings is paramount for tailoring drying processes to specific applications and optimizing their efficiency.

3.2.2 Water vapor diffusion

Water vapor diffusion into the surrounding gas: The saturated air layer above the sample in a drying process is a critical zone where the dynamics of moisture transfer undergo significant transformations, shown in figure 3.5. As moisture evaporates from the sample, it saturates the air immediately above it with water vapor, creating a layer of high humidity. This saturated air layer is characterized by its limited capacity to hold additional moisture, as it approaches the point of relative humidity equal to 100%. Consequently, the process of diffusion comes into play, governing the movement of water vapor from the saturated layer into the surrounding gas. Diffusion is driven by the concentration gradient, as water molecules migrate from regions of higher concentration (saturated air layer) to regions of lower concentration (the surrounding gas). This diffusion process is influenced by factors such as temperature, pressure, and the characteristics of the gas medium. Understanding the interplay between the saturated air layer and the diffusion of water vapor is essential for optimizing drying processes, as it directly impacts drying rates, humidity control, and the overall efficiency of moisture removal from the sample.

Water vapor into air diffusivity: This statement suggests that the movement of water vapor in the air is driven by differences in vapor concentration within a non-homogeneous mixture. When there is variation in the concentration of water vapor in the air, water vapor molecules tend to move from regions of higher concentration to regions of lower concentration. This is a common phenomenon and is often associated with processes like diffusion in gases.

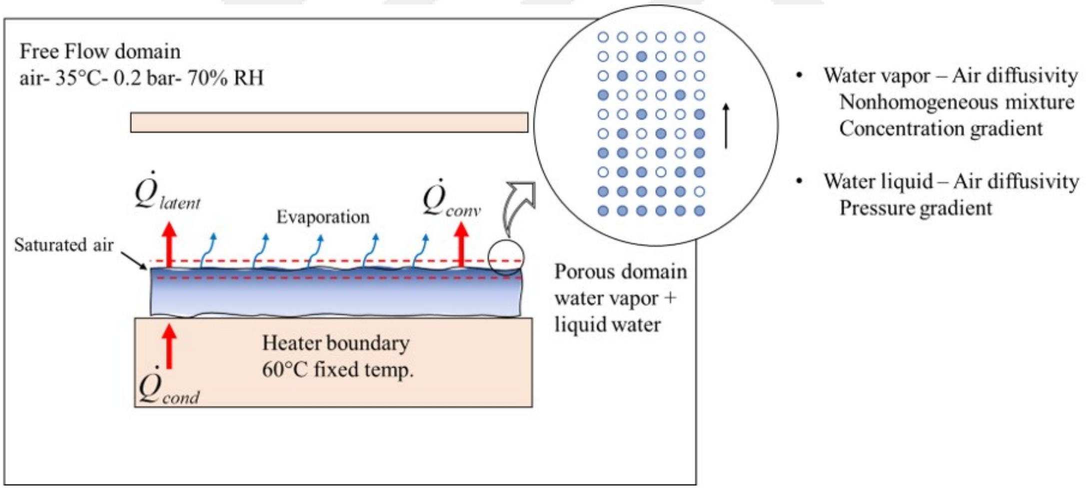

Figure 3.5: Explanation of diffusivity in drying simulations.

Water liquid into air diffusivity: In contrast, this statement implies that the movement of liquid water into the air is driven by differences in pressure. When there is a pressure gradient between a liquid and the surrounding air, it can cause liquid water to flow into the air, particularly if the liquid is under higher pressure than the air. This pressure-driven transport is typically observed in situations such as the release of liquid from a pressurized container. So, while both statements involve moisture transport, they operate on different principles—one is based on vapor concentration differences (diffusion), and the other is based on pressure differences (pressure-driven flow).

3.2.3 Moisture transport inside the porous domain

Moisture transport within the porous domain of a material undergoing drying is a complex and multifaceted phenomenon. It involves the movement of moisture through interconnected pores, capillaries, and void spaces within the material's structure. The driving forces behind this transport can include factors such as thermal gradients, pressure differentials, and concentration gradients. As the material's surface undergoes evaporation, it generates a moisture gradient within its porous structure. This gradient facilitates the transportation of moisture from the material's interior towards the surface, enabling it to evaporate into the surrounding environment, [47].

The rate of moisture transport within the porous media is influenced by several factors, including the material's porosity, permeability, and the presence of barriers or obstacles that may impede or enhance the movement of moisture.

3.2.4 Effective conductivity

Effective conductivity, a key parameter in the realm of porous media, plays a crucial role in dictating heat and mass transfer processes within these materials. It is important to note that moisture content exerts a profound influence on the effective conductivity of porous media. As moisture content within a porous material increases, it significantly alters the thermal conductivity properties of the material. For example, see figure 3.6, a mere 5 percent increase in moisture content can result in a remarkable 25% increase in heat transfer rates. This phenomenon underscores the dynamic nature of porous media, where the presence and movement of moisture within the material can dramatically impact its ability to conduct heat. Understanding and manipulating effective conductivity is essential for optimizing processes like drying, where efficient heat transfer is integral to achieving desired outcomes while conserving energy resources.

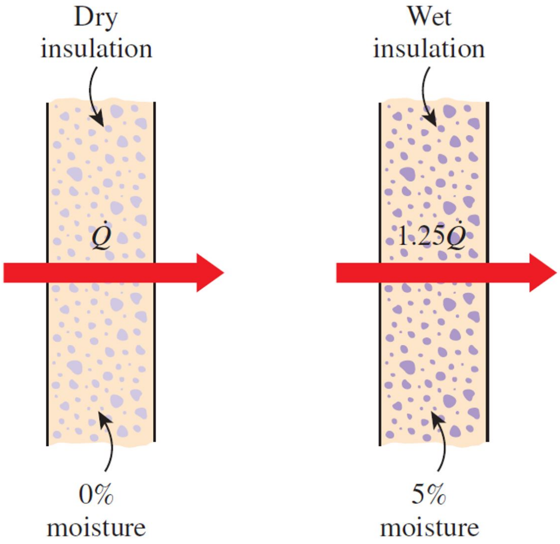

Figure 3.6: 5 percent moisture content can increase heat transfer by 25 percent

3.3 Model development

This section discusses the theoretical physics behind the pulsed vacuum drying (PVD) technique and its effect on drying time. The drying process in PVD involves multiple physical processes, such as heat transfer and mass transfer, which are collectively referred to as multiphysics, shown in Figure 3.7. It also involves multiple phases, including air as a gas, water as a liquid, and the fabric material as a solid phase, which is known as multiphase. Additionally, the drying process occurs at different scales, such as the micro-stage, which refers to the microscopic level of the fabric material [48].

3.3.1 System description and assumptions

To understand the underlying physics of PVD and its impact on drying time, a model is developed that takes into account the multiphysics and multiphase nature of the drying process. This model helps in analyzing the behavior of the moist fabric sample during drying and provides insights into the factors affecting drying time.

Since there are no chemical reactions involved in the drying process, mass and energy conservation equations are used to describe the behavior of the moist fabric sample. These equations ensure that the total mass and energy within the system remain constant during the drying process.

The models are built upon certain assumptions that simplify the analysis of the drying process. These assumptions are based on the understanding that there are no chemical reactions occurring and that the behavior of the fabric sample can be described using mass and energy conservation equations.

- The wet fabric's unit cell comprises three distinct phases: solid, liquid, and gas. These phases are denoted by three volume fractions: θ_S (constant), θ_L and θ_G (see equation 3.4).
- The effective thermal and mass parameters are computed by the model using time-varying volume fractions.
- The sample is considered as a rectangular cube that has identical dimensions, mass, and volume as the experimental sample.
- Throughout the drying process, the sample maintains a consistent and uniform porosity.
- The model calculates a unified temperature value that is applicable to all three phases of the sample.
- The transport of liquid within the sample is simulated using Richards equation, which enables the application of a simplified linear relationship for the apparent diffusion coefficient.

- The sample relies only on evaporation as a means to dissipate volumetric heat and only conduction as heat transfer method.
- The interactions between the liquid and solid are not considered in the model.
- During the drying process, the physical characteristics of all materials remain constant and exhibit uniformity in all dimensions.

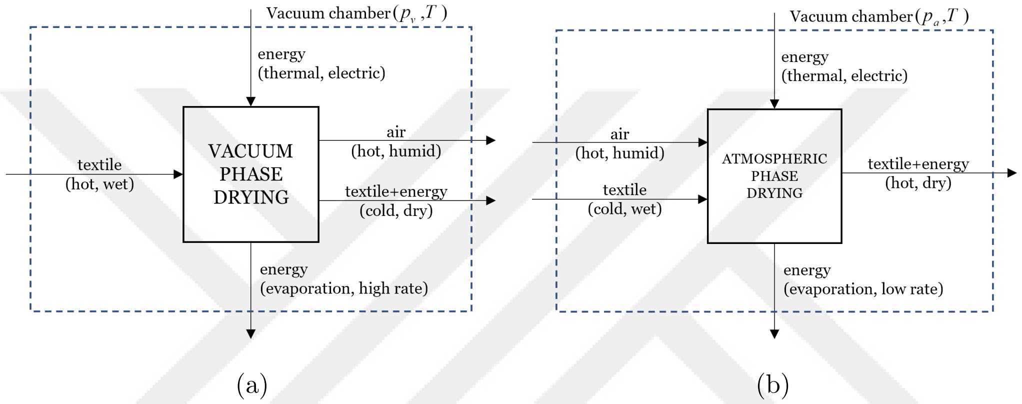

(a) (b)

Figure 3.7: The drying procedure model considering heat and mass flows: (a) the vacuum duration phase, (b) the atmospheric duration phase.

The figure 3.7 provides a schematic comparison of two different drying processes for textiles of Vacuum Phase Drying and Atmospheric Phase Drying. The process starts with a hot, wet textile being introduced into a vacuum chamber, where the pressure and temperature are controlled. Energy, in the form of heat or electricity, is applied to the system. This energy causes the water in the textile to evaporate at a high rate due to the low-pressure environment of the vacuum chamber. The air, now hot and humid due to the evaporation, is removed from the system. The result is a textile that is now cold and dry due to the energy (heat) being used for evaporation. This process also starts with a textile, but in this case, it is cold and wet. Similar to the vacuum process, energy is applied, but the drying occurs at atmospheric pressure, not in a vacuum. The rate of evaporation in atmospheric pressure is lower compared to vacuum drying because the higher pressure does not promote as rapid a phase change from liquid to vapor. The textile, after the application of energy, becomes hot and dry. This is because the ambient air pressure is higher than in the vacuum, which results in a slower evaporation rate and thus requires more energy to dry the textile. In summary, both diagrams show the flow of materials and energy through each drying process. The main difference lies in the pressure conditions under which drying takes place and the consequent rate of evaporation. Vacuum phase drying is typically faster due to lower pressure facilitating rapid evaporation, while atmospheric phase drying is slower due to the higher pressure inhibiting evaporation.

3.3.2 Governing Equations

Taking aforementioned assumptions into account, the model consists of two main partial differential equations [49]. The energy balance Equation (3.1), accounts for medium temperature. The mass balance Equation (3.2) accounts only for the change in the liquid phase (θ_L).

$$(\rho_e C_{p,e})\frac{\partial T}{\partial t} = \nabla.(\lambda_e \nabla T) - \dot{m}_L \Delta H_{vap} \tag{3.1}$$

$$\frac{\partial \theta_L}{\partial t} = \nabla.(D_L \nabla \theta_L) - \frac{\dot{m}_L}{\rho_L} \tag{3.2}$$

3.3.3 Constitutive Laws

The common term in these two equations is the evaporation rate ($\dot{m}_L$), which couples the differential equations.

$$\dot{m}_L = \begin{cases} k_{vap}\rho_L \frac{p_c - p_G}{p_t} & \text{if } p_c > p_G \\ 0 & \text{otherwise} \end{cases} \tag{3.3}$$

$$\theta_S + \theta_L + \theta_G = 1 \tag{3.4}$$

Equation (3.3) demonstrates the water elimination rate, which is proportional to the difference between the partial vapor pressure inside the porous sample p_c and the chamber internal vapor pressure p_G. The water vapor pressure inside the chamber p_G increases due to changes in θ_G, which is caused by the evaporation of water from the sample. p_t is the total pressure of the chamber and is defined based on the pressure phase the system is in, either the vacuum phase or the atmospheric phase. Realistic estimates for k_{vap} are obtained by using this simple multiphase model.

The expression below is utilized to compute p_c value, the partial vapor pressure inside the pores ($kN.m^{-2}$):

$$p_c(T_c, M_c) = p_{sat}(T_c)a(M_c) \tag{3.5}$$

in which p_{sat} is a value that depends on both the temperature of the cloth T_c and the water activity coefficient a.

Water activity coefficient (a)

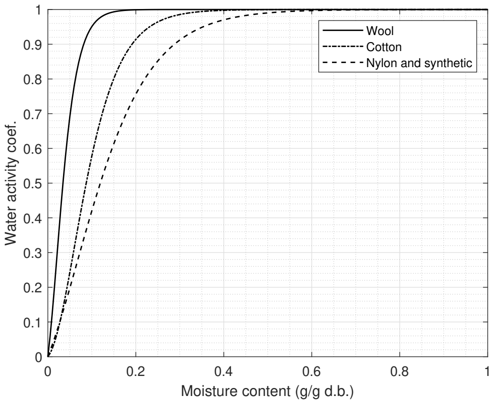

Figure 3.8: Desorption isotherms of 3 main fabric types.

Equation (3.6) estimates the water activity coefficient, which is a mathematical approximation for cotton sample desorption isotherms [50]. The implementation of approximate curves produces satisfactory results, on the micro-scale level of aggregation that is being considered here [51]. For the cotton samples water activity coefficient is independent of the vacuum and atmospheric phase pressures. This coefficient is a function of moisture content. The water activity coefficient holds the maximum value of unity, while the product's level of moisture is comparatively high (> 40%). This is the reason for the constant evaporation rate at the initial drying stages. However, the desorption isotherm of various textiles tends to reduce gradually, as the moisture content becomes less than 40%. Desorption isotherms, depicted in Figure 3.8, play a crucial role in comprehending the microscale mechanics of drying. As stated in the preceding section, the evaporation rate is dependent on the partial vapor pressure within the sample pores [52]. In addition, p_c is related to water activity and desorption-isotherm as shown by Equation (3.5). Thus, the steady drying rate indirectly depends on the desorption isotherm and moisture content.

$$a(M_c) = 1 - \frac{18M_c + 2}{1 + 2^{30M_c}} \tag{3.6}$$

Moisture diffusivity coefficient (D_L)

In this article, we make the presumption that the capillary flow is the dominant mechanism for the concurrent movement of liquid in the wet sample. It is worth mentioning that capillary pressure depends nonlinearly on moisture content. If we use Darcy's law and the definition of capillary pressure as shown in Equations (3.7) and (3.8):

$$j_L = -\frac{\rho_L}{\mu_L}\kappa(\theta_L)\nabla p_L \tag{3.7}$$

$$p_{cap}(\theta_L) = p_G - p_L \tag{3.8}$$

By substitution of liquid phase pressure from Equation (3.8) into Darcy's equation, we can easily find the liquid flux as shown below, that is referred to as Richards equation:

$$j_L = -\frac{\rho_L}{\mu_L}\kappa(\theta_L)\left(\frac{\partial p_{cap}(\theta_L)}{\partial \theta_L}\right)\nabla\theta_L \tag{3.9}$$

Here is where we can define apparent moisture diffusivity that can show the role of both permeability and capillary pressure:

$$D_L(\theta_L) = -\frac{\kappa(\theta_L)}{\mu_L}\left(\frac{\partial p_{cap}(\theta_L)}{\partial \theta_L}\right) \tag{3.10}$$

Several formulations have been developed to explain exactly how the relative permeability and capillary pressure depend on the moisture content. According to the explained procedure to define Equation (3.10), in this work, we employ a simplified and straightforward linear relation of diffusivity for the model:

$$D_L = \begin{cases} \alpha(\theta_L - \theta_L^*) & \text{if } \theta_L \geq \theta_L^* \\ 0 & \text{otherwise} \end{cases} \tag{3.11}$$

where θ_L^* represents the remaining moisture content, the point at which the diffusion begins to drop, and α indicates the scaling constant. We conducted a systematic search using the model to obtain realistic values of these parameters. The goal was to minimize the error between the model drying curve and the experimental result of the same scenario.

3.3.4 Material Properties

As previously stated, the sample consists of a solid matrix and a water-air mixture that occupies the solid matrix cavities. Therefore, the sample material properties must consider the properties of the three phases by their existence portion in the medium. In this model, the effective density and heat capacity are computed from the volume fractions of each phase. For effective thermal conductivity, the linear interpolation between dry and wet conductivity is suggested by Kohout et al. [53] as follows:

$$\rho_e = \theta_S\rho_S + \theta_L\rho_L + \theta_G\rho_G \tag{3.12a}$$

$$C_{p,e} = \frac{1}{\rho_e}(\theta_S\rho_S C_{p,S} + \theta_L\rho_L C_{p,L} + \theta_G\rho_G C_{p,G}) \tag{3.12b}$$

$$\lambda_e = \lambda_{dry} + \frac{\theta_L}{1-\theta_S}(\lambda_{wet} - \lambda_{dry}) \tag{3.12c}$$

3.3.5 Initial and boundary conditions

In this model, we begin with an initial moisture content of 100%, sample dry bone mass of 40 g, sample temperature at 25°C, and gas phase RH at 60%. The bottom boundary edge of the fabric sample is exposed to a constant temperature T_{bed} (predefined according to experimental conditions). This layer is in direct contact with the heat bed in the experimental setup. Other edges of the sample have thermal isolation as the boundary condition for the energy balance Equation (3.1). Furthermore, we define a boundary condition that simulates no liquid phase movement at the sample's edges to address the mass balance Equation (3.2). This implemented boundary condition emulates the absence of liquid phase migration through the sample's boundaries, effectively simulating the scenario where no liquid phase escapes during the drying course.

3.4 COMSOL simulation

In the initial stages of our simulation, it is important to acknowledge that it was not without imperfections and that the results did not perfectly align with the experimental data. However, this served as a starting point for our investigation and highlighted areas where refinement was needed. Over time, we made significant progress in enhancing the accuracy of our simulation model, compare figures 3.9 and 3.10. Through a series of improvements in our underlying assumptions and the rigorous application of parametric sensitivity analyses, the model performance saw a remarkable enhancement. These refinements not only brought us closer to matching the simulation results with real-world experiments but also bolstered the model's overall reliability. In light of the principles and assumptions discussed earlier, the determination of evaporation rates in porous media involved the solution of complex partial differential equations. To tackle this, we utilized numerical solutions to integrate the governing mass and heat equations across a two-dimensional spatial domain. This numerical integration was executed using the COMSOL multiphysics finite element software platform. It is worth emphasizing that we conducted thorough parametric sensitivity analyses on adjustable parameters, affirming the

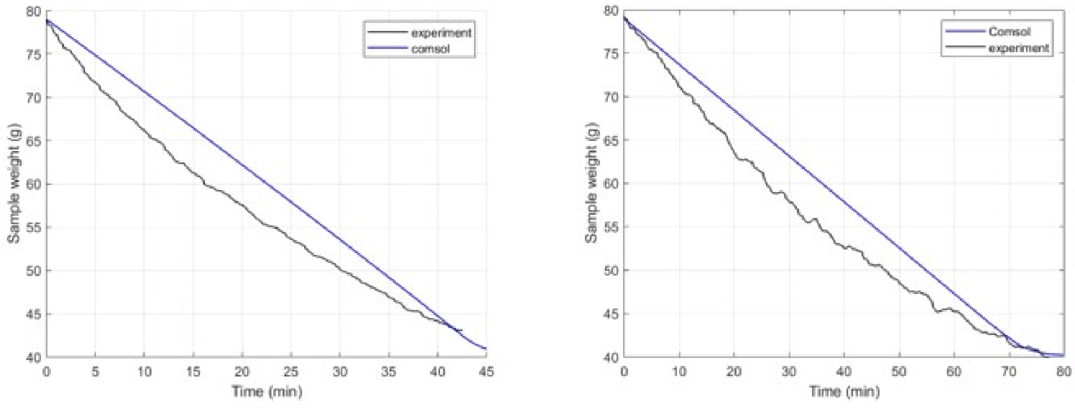

(a) (b)

Figure 3.9: Wet sample weight drying curves; (a) Constant 0.2 bar, 60°C and (b) Constant 1 bar, 60°C

robustness and trustworthiness of the results. Additionally, we carefully selected mesh resolutions, taking into account their significant impact on result accuracy and computational efficiency.

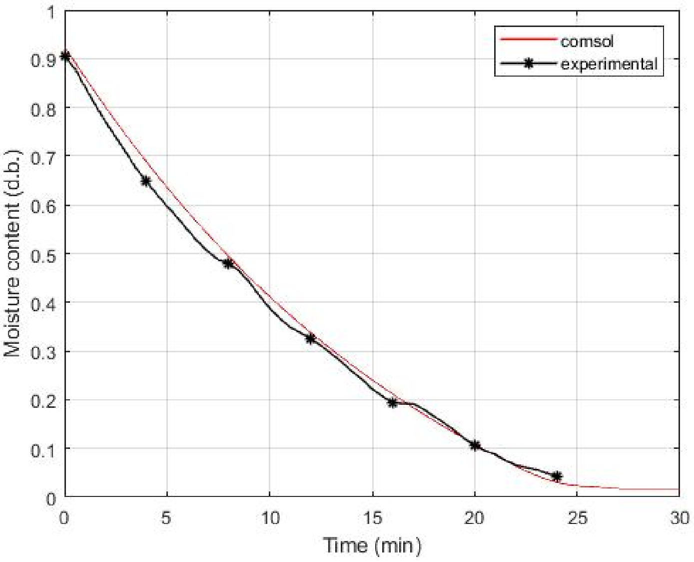

Figure 3.10: Wet sample drying curve at 80°C bed temp. and 8:1 vacuum modulation at 0.2 bar

The evaporation rate in porous media is calculated by solving partial differential equations (PDEs). PDEs are mathematical equations that involve multiple variables and their partial derivatives. They are used to describe various physical phenomena, such as heat transfer, fluid flow, and diffusion, which involve changes in multiple variables over space and time. The PDEs are used to model the evaporation process in porous media, such as textiles. These equations take into account factors like mass and heat transfer to calculate the rate at which moisture evaporates from the material. Numerical Solutions and Integration

The numerical solutions were used to integrate the governing mass and heat equations (3.1) and (3.2) in a 2D spatial domain. Numerical solutions involve approximating the solutions to mathematical equations using computational methods. In this case, numerical methods were used to solve the PDEs that describe the evaporation process. Integration refers to the process of finding the total value of a function over a given domain. In this case, the authors integrated the mass and heat equations over a 2D spatial domain, which means that they calculated the overall effect of these equations within a specific area. The integration was performed using a software platform called COMSOL Multiphysics finite element software. This software is designed to handle complex mathematical models and perform numerical integration of the PDEs. Finite element software is a type of software that uses the finite element method, a numerical technique, to solve complex mathematical models. Multiphysics refers to the ability of the software to handle multiple physical phenomena simultaneously. In this case, the software is capable of solving both the mass and heat equations involved in the evaporation process. The authors chose this software platform because it is specifically designed to handle the type of calculations required for their research.

3.5 MATLAB simulation

In this section, we get into the MATLAB code we've developed to simulate both constant vacuum and pulsed vacuum drying processes within the vacuum prototype setup. The primary aim of this code is to capture the intricate dynamics of air properties inside the drying chamber. These properties encompass essential factors like suction flowrate parameters and the humidity of the air confined within the vacuum drum. Our exploration begins with a comprehensive overview of the parameters and constants that underpin the simulation. We will provide insight into the key variables and values that steer the entire process, giving readers a clear understanding of the foundational elements. Next, we will discuss the algorithm at the heart of our MATLAB code. This algorithm forms the backbone of our simulations, orchestrating the intricate dance of air properties, vacuum dynamics, and material drying. Subsequently, we turn our attention to the equations and how they drive the continuous updates of parameters throughout the simulation. This section elucidates the mathematical foundations upon which our code operates, connecting theory to practice. Finally, we discuss the results generated by our simulations and engage in a meaningful discussion about the implications and insights drawn from these results. Our aim is to provide a comprehensive understanding of our MATLAB code's functionality, its significance in the context of vacuum drying, and the valuable data it produces for our project.

3.5.1 Simulation parameters and constants

The table presented in 3.1 compiles a crucial list of parameters that play an integral role in our simulation of the vacuum drying process. These parameters encompass various facets of the system, from environmental conditions to material properties. For instance, the ambient temperature represents the baseline temperature of the surrounding environment, setting the stage for heat exchange. On the other hand, the vacuum pressure signifies the critical pressure within the drying chamber, which directly impacts the moisture removal rate. The initial and final moisture levels, coupled with initial relative humidity, influence the drying kinetics and endpoints.

Parameters like the suction flowrate and convective heat transfer coefficients and directly dictate the rate at which moisture evaporates and the transfer of heat within the system. The dimensions and porosity of the sample govern the sample's physical characteristics, which impact its drying behavior. The molecular properties, such as the molar mass of water vapor and dry, hold relevance in the calculation of air prop-

Table 3.1: MATLAB simulations parameters and constants.

Parameter	Value	Parameter	Value
T_{ambient}	25°C	P_{vacuum}	0.2 bar
$P_{\text{nonvacuum}}$	1 bar	t_{vacuum}	tbd s
$t_{\text{nonvacuum}}$	tbd s	T_{heater}	60°C
$V_{chamber}$	$3.14 \times \left(\frac{0.46}{2}\right)^2 \times 0.56$ m^3	porosity	0.5
m_{sample}	0.046 kg	sample_dimensions	[20, 20, 0.5] cm
initial moisture content, $M_c(0)$	0.6	final_moisture	0.03
initial relative humidity, ϕ	0.6	$suction\_flowrate$	$10 \times \frac{10^{-3}}{60}$ m^3/s
T_{gas}	35°C	latent_heat	2258 J/kg
R_v	461.5 J/(kg·K)	R_a	287.1 J/(kg·K)
k_{vap}	0.005 s^{-1}	ρ_L	1000 kg/m^3
$h_{\text{conv\_airflow}}$	10 W/(m^2·K)	$h_{\text{cond\_sample}}$	1 W/(m·K)
$h_{\text{cond\_water}}$	0.6 W/(m·K)	$h_{\text{conv\_sample}}$	50 W/(m^2·K)
$h_{\text{conv\_water}}$	1000 W/(m^2·K)	$C_{p,sample}$	1200 J/(kg·K)
$C_{p,water}$	4182 J/(kg·K)	M_{vapor}	0.018 kg/mol
$M_{\text{dry\_air}}$	0.02897 kg/mol	A_{pipe}	$(0.003)^2 \times 3.14$
$D_{\text{capillary}}$	10×10^{-10}	$D_{surface}$	10×10^{-13}

erties. These parameters collectively form the foundation of our simulation, with each one influencing specific aspects of the vacuum drying process. Understanding their significance is crucial for comprehending the dynamics and behavior of our system.

3.5.2 Simulation equations

The equations featured in this section are pivotal for the vacuum drying simulation, as they encapsulate the fundamental processes and transformations taking place within the system. These equations cover a wide array of parameters and phenomena. The moisture content of the sample is a critical parameter for understanding the drying process, as it represents the amount of liquid water in the sample. The water activity coefficient is essential for estimating the sample's water vapor pressure and understanding its behavior in different moisture conditions.

$$
\begin{aligned}
M_c(i) &= \frac{m_{liquid\_water}(i)}{m_{sample}} \\
\text{Water activity} : \alpha(i) &= 1 - \frac{18 \cdot M_c(i) + 2}{1 + 2^{30 \cdot M_c(i)}} \\
p_{\text{sat}}(i) &= XSteam(T_{sample}(i)) \times 10^5 \\
p_c(i) &= p_{\text{sat}}(i) \cdot \alpha(i) \\
\rho_{\text{vapor}}(i) &= \frac{m_{water\_vapor}(i)}{V_{chamber}} \\
d\text{mass}_{evap} &= -k_{evap} \cdot \rho_{vapor}(i) \cdot \ln\left(\frac{p_{chamber}(i) - p_v(i)}{p_{chamber}(i) - p_c(i)}\right) \\
\delta m_{diffusion}(i) &= -A \cdot (D_{\text{capillary}} + D_{\text{surface}}) \cdot \frac{m_{liquid\_water}(i)}{V_{sample}} \cdot \frac{1}{t_{sample}} \\
\delta m_{liquid\_water}(i) &= \delta m_{diffusion}(i) + \delta m_{evap(i)} \\
\delta m_{water\_vapor}(i) &= -\delta m_{liquid\_water}(i) + Q_{suction} \cdot \rho_{\text{vapor}}(i) + \dot{m}_{inlet} \cdot (1 - c_{a_{\text{out}}}) \\
\rho_{\text{dry\_air}}(i) &= \frac{m_{dry\_air}(i)}{V_{chamber}} \\
\delta m_{dry\_air}(i) &= Q_{suction} \cdot \rho_{\text{dry\_air}}(i) + \dot{m}_{inlet} \cdot c_{a_{\text{out}}} \\
C_{\text{eff}}(i) &= m_{liquid\_water}(i) \cdot C_{p,water} + m_{sample} \cdot C_{p,sample} \\
h_{\text{conv\_eff}}(i) &= \frac{m_{liquid\_water}(i) \cdot h_{\text{conv\_water}} + m_{sample} \cdot h_{\text{conv\_sample}}}{m_{liquid\_water}(i) + m_{sample}} \\
h_{\text{conv\_eff2}}(i) &= h_{\text{conv\_eff}}(i) + 1 \cdot h_{\text{conv\_airflow}} \\
dT_{conv} &= \frac{h_{\text{conv\_eff2}}(i) \cdot (T_{\text{gas}} - T_{sample}) \cdot A_{sample}}{C_{\text{eff}}(i)} \\
h_{\text{cond\_eff}}(i) &= \frac{m_{liquid\_water}(i) \cdot h_{\text{cond\_water}} + m_{sample} \cdot h_{\text{cond\_sample}}}{m_{liquid\_water}(i) + m_{sample}} \\
dT_{cond} &= h_{\text{cond\_eff}}(i) \cdot (T_{\text{heater}} - T_{sample}) \cdot \frac{A_{sample}}{t_{sample} \cdot C_{\text{eff}}(i)} \\
dT_{phase\_change} &= \frac{h_{latent\_heat} \cdot \delta m_{liquid\_water}(i)}{C_{\text{eff}}(i)} \\
dT &= dT_{conv} + dT_{cond} + dT_{phase\_change}
\end{aligned}
\tag{3.13}
$$

The saturation pressure of water vapor is intricately related to the temperature, and it helps determine the partial vapor pressure within the sample's pores, which is a crucial boundary condition. Equations for mass transfer rates are integral for tracking the movement of liquid water and water vapor within the system. The effective heat capacity and heat transfer coefficients and are instrumental in determining the heat exchange within the system, which plays a vital role in the drying process. These equations are vital for calculating changes in temperature due to convection, conduction, and phase change. Each equation represents a piece of the intricate puzzle that is vacuum drying simulation, contributing to a holistic understanding of the dynamic processes occurring within the chamber.

$$
\begin{aligned}
\mathrm{time}(i+1) &= \mathrm{time}(i) + dt \\
T_{sample}(i+1) &= T_{sample} + \delta T \times dt \\
m_{liquid\_water}(i+1) &= m_{liquid\_water}(i) + \delta m_{liquid\_water}(i) \times dt \\
m_{water\_vapor}(i+1) &= m_{water\_vapor}(i) + \delta m_{water\_vapor}(i) \times dt \\
m_{dry\_air}(i+1) &= m_{dry\_air}(i) + \delta m_{dry\_air}(i) \times dt \\
p_{dry\_air}(i+1) &= \frac{m_{dry\_air}(i+1) \times R_a \times (T_{\mathrm{gas}} + 273.15)}{V_{chamber}} \\
p_{water\_vapor}(i+1) &= \frac{m_{water\_vapor}(i+1) \times R_v \times (T_{\mathrm{gas}} + 273.15)}{V_{chamber}} \\
p_{chamber}(i+1) &= p_{dry\_air}(i+1) + p_{water\_vapor}(i+1) \\
\omega(i+1) &= \frac{m_{water\_vapor}(i+1)}{m_{dry\_air}(i+1)} \\
c_a(i+1) &= \frac{m_{dry\_air}(i+1)}{m_{dry\_air}(i+1) + m_{water\_vapor}(i+1)} \\
c_v(i+1) &= 1 - c_a(i+1) \\
\omega_{\mathrm{max}}(i) &= 0.622 \times \frac{p_{sat}(T_{gas})}{p_{chamber}(i) - p_{sat}(T_{gas})}
\end{aligned}
\tag{3.14}
$$

The parameters listed in 3.14 are continuously updated at each iteration of the simulation. This real-time updating is essential to capture the dynamic nature of the vacuum drying process and its impact on the chamber's conditions. The simulation uses a time step of 1 second to increment time, allowing for the tracking of changes over the entire 5000 seconds of the drying process. The total number of steps is calculated by dividing the total time by the time step, and this dictates how frequently parameters are updated. Key parameters, such as the sample's temperature and the masses of liquid water, water vapor, and dry air within the chamber, are updated in each iteration based on the results of the preceding equations. This iterative process captures the evolving state of the system as drying progresses. Pressure values for dry air, water vapor, and the chamber itself are recalculated with each iteration to reflect changes in the chamber's conditions. Other important parameters, such as the water vapor fraction, the dry air fraction, and the vapor fraction, are also updated to reflect the evolving mixture within the chamber. The parameter provides a reference point to gauge the relative humidity and potential for saturation within the chamber. The constant updating of these parameters enables a comprehensive understanding of the drying process and how it evolves over time.

3.5.3 Simulation algorithm

The algorithm implemented in the MATLAB simulation for constant vacuum drying and pulsed vacuum drying is designed to replicate the complex dynamics of the vacuum drying process in a systematic and accurate manner, see figure 3.11. At the core of the algorithm is a time-stepping approach where the simulation progresses in small increments of one second over the total simulated time of 5000 seconds. At each step, key parameters are updated to reflect the evolving conditions within the drying chamber. These parameters include the sample's temperature, the masses of liquid water, water vapor, and dry air, and various pressure values within the chamber. This continuous updating captures the dynamic nature of the drying process, providing real-time insights into how the system evolves over time. The primary equations driving the simulation encompass mass transfer processes such as evaporation and diffusion, as well as the associated changes in temperature due to convection, conduction, and phase change. These equations are integrated into the simulation to model the intricate interplay of mass and heat transfer within the porous textile sample and the chamber's air mixture. Additionally, the algorithm incorporates key properties like water activity, water vapor pressure, and effective heat capacity to ensure that the simulation is accurate and representative of real-world drying scenarios. By tracking these parameters and applying the fundamental

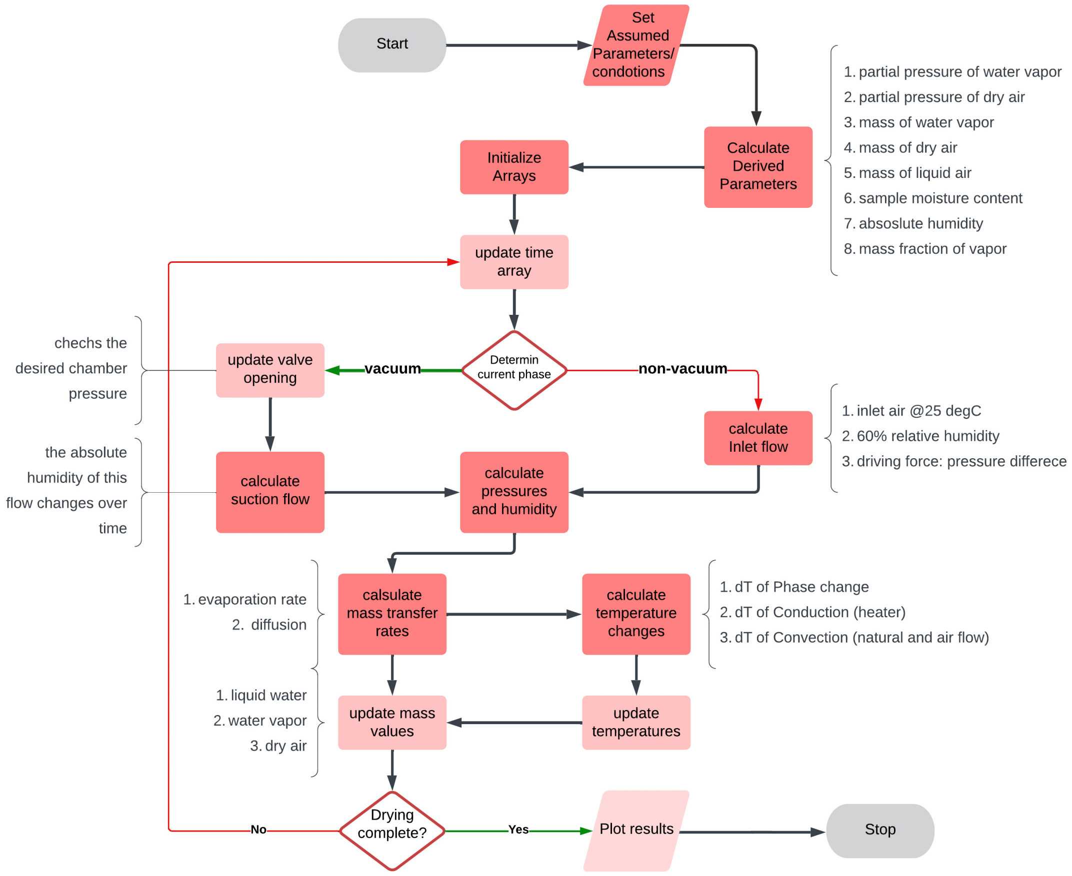

Figure 3.11: MATLAB simulation algorithm.

equations of mass and heat transfer, the algorithm allows us to gain insights into the moisture content of the textile sample, the rate of evaporation, and the temperature changes within the system as drying progresses. This detailed understanding is vital for optimizing the vacuum drying process.

3.5.4 Results and discussions

In the results section, we present a comprehensive overview of our MATLAB simulation for constant vacuum drying and pulsed vacuum drying. The section features critical data and visualizations that help us understand the drying process and its intricate dynamics, see table 3.2. We showcase various plots that provide insights into different aspects of the drying process, figures 3.12 and 3.13. These plots collectively provide a clear and detailed picture of the vacuum drying process, enabling us to assess its performance and make informed decisions for process enhancement.

- Evaporation Rate: This plot offers valuable insights into the initial stages of the drying process, depicting how the rate of moisture removal evolves over time. It helps us understand the efficiency of the drying mechanism during the early minutes, which is crucial for optimizing the overall process.
- Water Vapor Mass Ratio: We analyze the mass of water vapor relative to dry air within the chamber. This plot shows how the air's moisture content changes as the drying process proceeds, helping us understand the transition of air from a humid to a drier state.
- Moisture Content of the Sample: We track the moisture content of the textile sample throughout the simulation. This plot helps us visualize how the sample dries over time and provides valuable information about the progress of drying and the point at which it reaches a desired moisture level.
- Specific Humidity Ratio: In this plot, we monitor the specific humidity ratio inside the chamber. It reflects the moisture-holding capacity of the air mixture within the chamber, providing insights into how effectively the air can absorb and carry away moisture from the sample. Furthermore, we compare the specific humidity ratio (omega) with the calculated maximum humidity capacity (omega max) of the air. This comparison helps us understand when the air reaches its moisture-carrying limit, which can be a critical factor in determining the drying efficiency.

Table 3.2: MATLAB constant vacuum and PVD simulation results.

	Condition	Average rate (g/min)	Total drying time (min)
Simulation	Constant vacuum 0.2bar	0.39	55
Simulation	Pulsed vacuum 210 s/10 s 0.2bar	0.64	40

In the results section for the simulation of constant vacuum drying at 0.2 bar, we present a set of plots that offer a deep understanding of the drying process. This particular simulation resulted in an average evaporation rate of 0.39 g/min, with a total drying time of 55 minutes. One key highlight from the evaporation rate plot is the distinctive peak observed at around 5 minutes into the drying process. At this point, the evaporation rate reaches 1.5 g/min, signifying a rapid moisture removal rate. However, it is crucial to note that after this peak, the rate begins to gradually decline.

The significance of this observation lies in the fact that the decrease in the evaporation rate is primarily due to the air inside the chamber reaching its maximum humidity capacity. Despite the constant vacuum suction rate, there comes a point where the air can no longer absorb additional moisture from the textile sample. This insight is valuable for process optimization, as it highlights the importance of balancing the suction rate with the air's humidity-holding capacity to maximize the efficiency of the drying process. It underscores the complexity of maintaining effective drying rates throughout the process and provides a basis for fine-tuning the vacuum drying system. Indeed, one of the advantages of pulsed vacuum drying becomes evident when we consider the dynamics of specific humidity within the vacuum chamber. By periodically stopping the vacuum generator and allowing air to re-enter the chamber (atmospheric phase duration), we create a valuable opportunity for the system. During this phase, the chamber has a chance to fill its air with dry air from the surroundings.

As a result, the specific humidity within the chamber decreases, indicating a lower concentration of water vapor. This change in system state is highly advantageous for the drying process. It means that for a short duration, the system exits the high-moisture, high-water-vapor state. This temporary shift to a drier environment can significantly boost the drying efficiency. Essentially, pulsed vacuum drying introduces intermittent phases of reduced humidity within the chamber. During these periods, the system can resume the drying process with a fresh supply of dry air, facilitating a more effective removal of moisture from the textile sample. This dynamic approach helps to overcome the limitations associated with constant vacuum

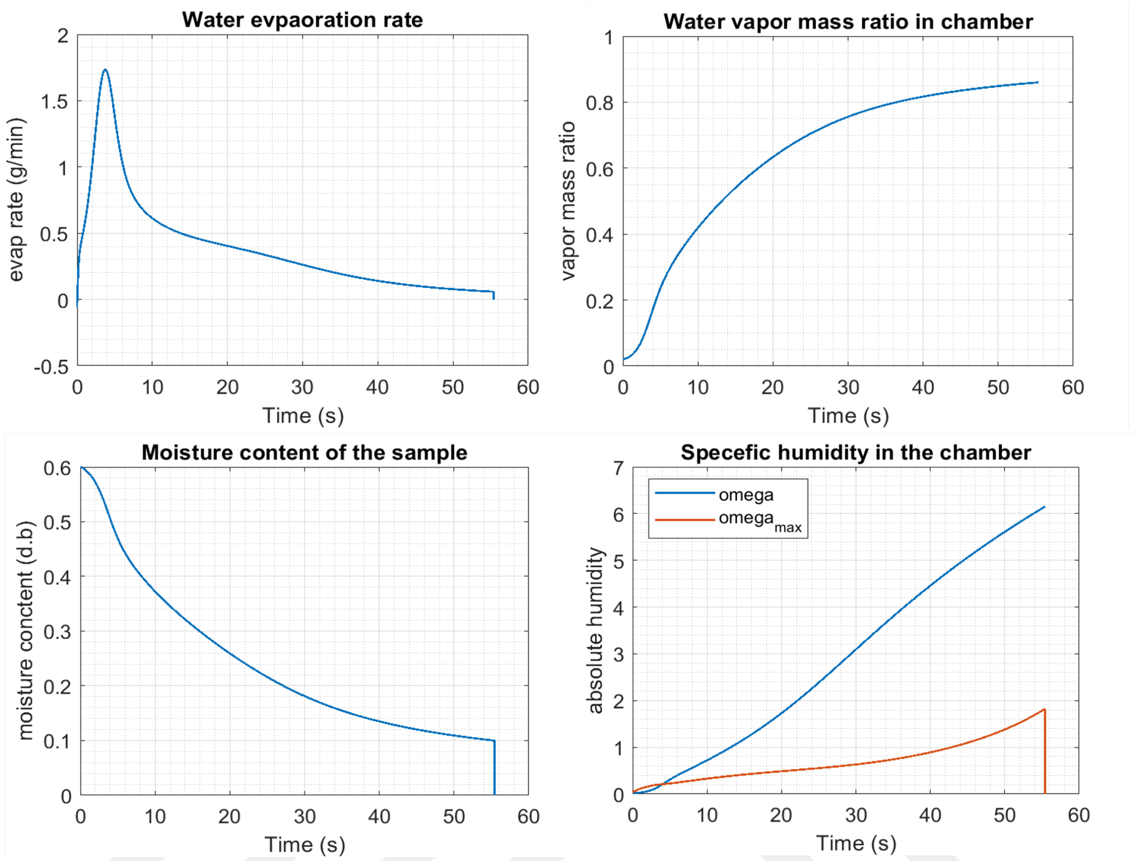

Figure 3.12: Constant vacuum simulation plots, 0.2 bar.

drying, where the air inside the chamber becomes saturated with moisture over time. Pulsed vacuum drying thus offers a way to maintain higher drying rates throughout the process and optimize the overall efficiency of textile drying. In the second set of simulation results, which focused on pulsed vacuum drying (210 seconds vacuum/10 seconds non-vacuum) with a vacuum level of 0.2 bar, we aimed to harness the power of pulsed vacuum to enhance the average drying rate. The average rate, in this case, was calculated to be approximately 0.64 grams per minute, with a total drying time of around 40 minutes.

What's particularly interesting in these results is the way we leveraged the variation in specific humidity, or the water vapor mass ratio, within the chamber. The plots clearly illustrate the impact of the pulsed vacuum strategy on the drying dynamics. During the nonvacuum phase, there's a noticeable reduction in the instantaneous drying rate. However, this is a planned consequence that plays a crucial role in

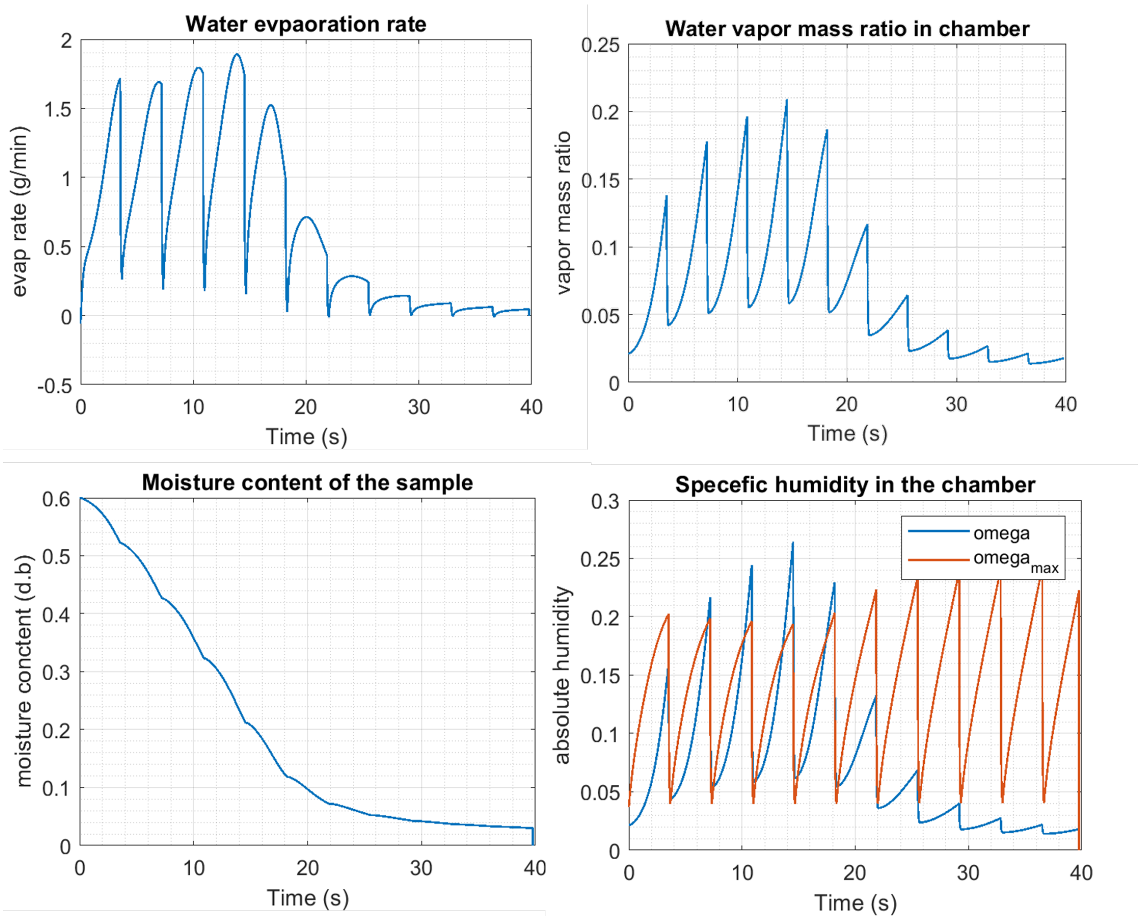

Figure 3.13: Pulsed vacuum simulation results, 0.2 bar and 210s/10s.

enhancing the overall efficiency. By allowing the system to have a brief period of exposure to non-vacuum conditions, we create the conditions for an increase in drying rate in the subsequent vacuum phase. This approach effectively balances the drying process, trading an initial reduction in drying rate for a subsequent boost. When considering the entire drying procedure, the average drying rate is significantly improved compared to a constant vacuum approach. In other words, by strategically utilizing pulsed vacuum, we've harnessed the power of humidity variation within the chamber to enhance the average drying rate and expedite the overall textile drying process.

Chapter 4

CONSTANT AND PULSED VACUUM TEXTILE DRYING

In this section, the preliminary tests conducted to examine the drying properties of our samples are demonstrated. Four plots are presented here, each depicting the dynamic changes in moisture content over time, Figures 4.2 and 4.1. It is important to note that all samples started with a moisture content of 100 percent, serving as a consistent baseline for our experiments. The moisture content measurements were obtained using load cells, which, like any measurement system, introduced some inherent errors, as reflected in the plotted data. These errors are an inherent part of the experimental process and are crucial to consider when interpreting our results.

4.1 Preliminary test

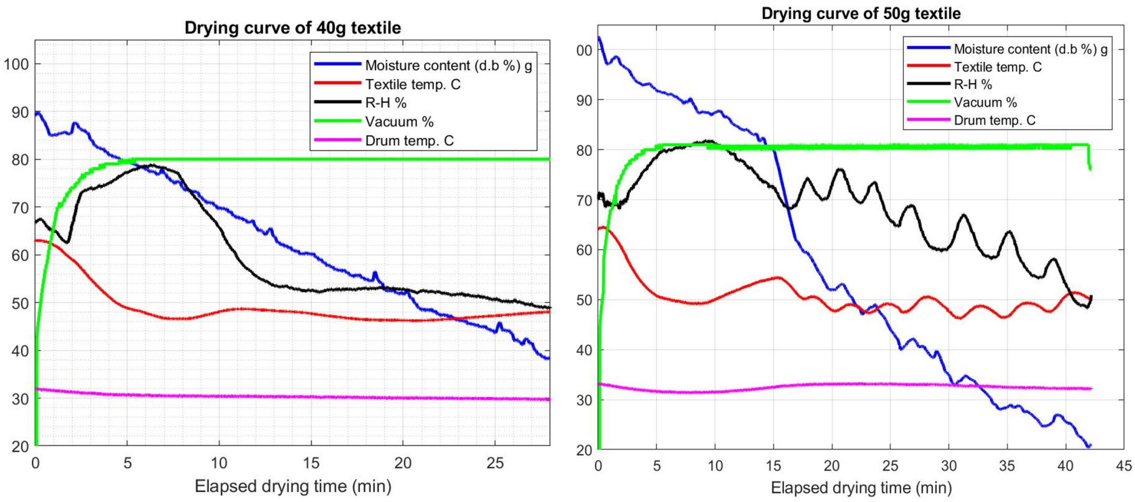

(a) (b)

Figure 4.1: Drying properties at 80% vacuum: (a) 40 gram cloth, (b) 50 gram cloth.

To provide a comprehensive view of our experimental setup, we include additional information in each plot of figures 4.1 and 4.2. The textile temperature was held constant at 60 degrees Celsius for all tests, ensuring a uniform drying environment. We also monitored the drum temperature to capture its impact on the drying process.

Chamber pressure played a critical role in our tests. In each of the four experiments, we maintained chamber pressure at a minimum of 0.2 bar, which corresponds to approximately 80 percent vacuum. This variation in pressure—between constant vacuum and pulsed vacuum—offers valuable insights into how it affects the drying process. Furthermore, we measured and plotted the relative humidity levels inside the chamber for each test. This information is integral to understanding the drying kinetics within our experimental setup. The preliminary tests laid the foundation for our study, helping to understand the initial behavior of the samples as they underwent the drying process. The combination of moisture content measurements, temperature profiles, chamber pressure variations, and relative humidity data provides a comprehensive overview of our experimental conditions and forms the basis for the subsequent analyses and discussions in this chapter. The implementation of

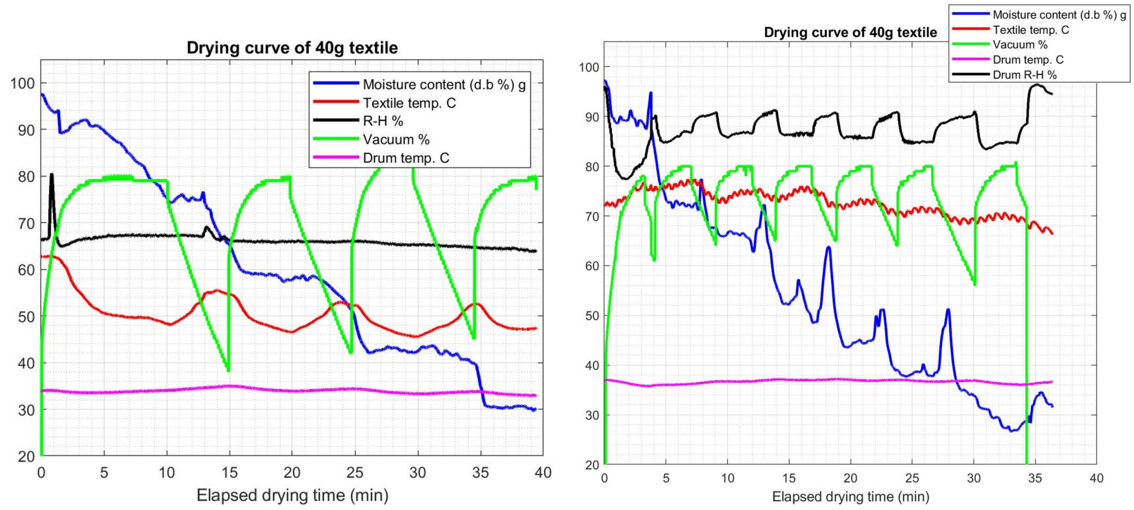

(a) (b)

Figure 4.2: Drying properties at 80% pulsed vacuum: (a) 40 gram cloth- VM 5min:5min, (b) 50 gram cloth-VM 3min:2min.

pulsed vacuum dynamics constitutes a pivotal aspect of our PVD (Pulsed Vacuum Drying) experiments. Within the PVD method, each cycle encompasses four distinct phases, each serving a unique role in our experimental process. Firstly, the vacuum development stage initiates, acting as the phase responsible for gradually decreasing the pressure from atmospheric levels to the desired vacuum point. This phase ensures a controlled reduction in pressure within the chamber. Following this, the steady vacuum phase takes over, maintaining the desired vacuum condition at a constant level. The third phase, termed the vacuum reduction phase, marks the moment when the vacuum generator is deactivated, and atmospheric air is rapidly introduced into the chamber. This transition is key to the pulsatile nature of our method. Finally, the fourth phase, known as the atmospheric pressure phase, sees the vacuum generator remaining inactive, resulting in a zero gradient pressure between the chamber and its surroundings, effectively preventing any further inlet airflow. During the first two phases of this cycle, precise control over the vacuum is

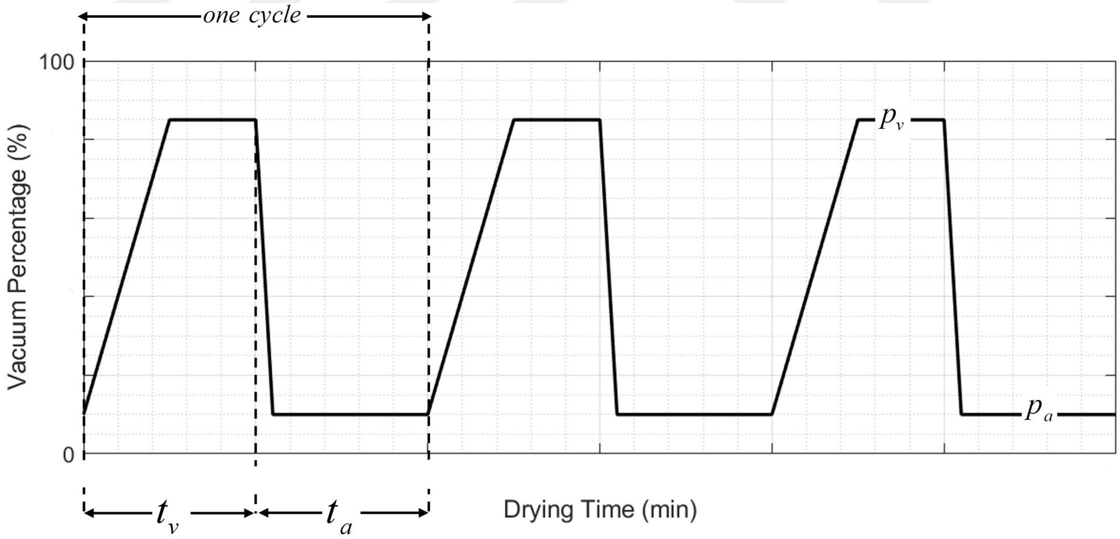

Figure 4.3: Explanation of vacuum modulation.

achieved and maintained at the desired pressure level through the use of a proportional valve. This period of controlled vacuum is referred to as the vacuum pressure duration (t_v). Subsequently, during the third and fourth phases, the chamber inlet valve is opened, and the vacuum generator is no longer part of the pneumatic circuit.

Table 4.1: Atmospheric drying results of 40g textile

Mass of Dry Cloth	40 grams		
Pressure	Atmospheric		
Heating Bed Temp.	70°C		
Time Duration	20 minutes		
	Trial 1	Trial 2	Trial 3
Initial Mass on Scale (g)	85.5	84.3	85.8
Initial Mass on Load Cell (g)	84.0	83.6	84.6
Final Mass on Scale (g)	71.7	71.8	70.9
Final Mass on Load Cell (g)	71.1	70.7	70.0
Evaporation Rate (g/ minute)	**0.69**	**0.62**	**0.74**

This portion of the cycle is designated as the atmospheric pressure duration (t_a). To quantify the vacuum modulation, we define it as the fraction VM, calculated as the ratio of t_v to t_a. This modulation factor (VM) plays a crucial role in our experiments and is further illustrated in Figure 4.3. The implementation of pulsed vacuum, with its distinct phases and careful modulation, is a cornerstone of our experimental approach, allowing us to explore and understand the intricate dynamics of the drying process within our controlled environment.

4.2 Introduction on Drying Conditions

The experimental results presented above provide valuable insights into the drying process under various conditions, including different pressure settings and heating bed temperatures. These findings shed light on the impact of these parameters on the evaporation rates of the samples.

In the first set of experiments conducted at atmospheric pressure and a heating bed temperature of 70°C, we observed an evaporation rate ranging from 0.62 to 0.74 g/minute over a 20-minute duration, see table 4.1. Notably, the samples exhibited relatively consistent evaporation rates within this range, suggesting that

Table 4.2: Constant vacuum (0.2 bar) drying results of 40g textile

Mass of Dry Cloth	40 grams	
Pressure	80% vacuum	
Heating Bed Temp.	70°C	
Time Duration	20 minutes	
	Trial 1	Trial 2
Initial Mass on Scale (g)	84.5	85.2
Initial Mass on Load Cell (g)	85.5	85.0
Final Mass on Scale (g)	56.7	55.8
Final Mass on Load Cell (g)	63.7	66.6
Evaporation Rate (g/minute)	**1.39**	**1.47**

at atmospheric pressure, the temperature had a limited effect on the drying kinetics.

Moving on to the experiments conducted at 80% vacuum and the same heating bed temperature of 70°C, a substantial increase in the evaporation rates was observed, ranging from 1.39 to 1.47 g/minute over the same 20-minute period, see table 4.2. This significant boost in evaporation rates can be attributed to the reduced pressure within the chamber, which facilitates a more efficient drying process.

The third set of experiments (table 4.2), carried out under 80% pulsed vacuum conditions with a higher heating bed temperature of 80°C and a unique 6-minute ON, 2-minute OFF cycle, demonstrated evaporation rates ranging from 1.5 to 1.6 g/minute. This innovative approach, involving pressure pulsations, resulted in enhanced drying rates compared to the constant vacuum conditions. The cyclic alteration between vacuum and atmospheric pressure seems to have a positive impact on the drying kinetics. Overall, these results underscore the significant influence of both pressure and temperature on the drying process of the samples. The transition from atmospheric pressure to vacuum conditions, particularly under pulsed vacuum, has

Table 4.3: pulsed vacuum (0.2 bar) drying results of 40g textile

Mass of Dry Cloth	40 grams	
Pressure	80% Vacuum (pulsed)	
Heating Bed Temp.	80°C	
Time Duration	20 minutes (6 min ON, 2 min OFF)	
	Trial **1**	Trial 2
Initial Mass on Scale (g)	83.8	85.8
Final Mass on Scale (g)	45.2	48.4
Evaporation Rate (g/minute)	**1.6**	**1.5**

a substantial effect on evaporation rates, offering potential avenues for optimizing and fine-tuning the drying process in various applications. These findings provide a solid foundation for further exploration and optimization of drying techniques in porous media.

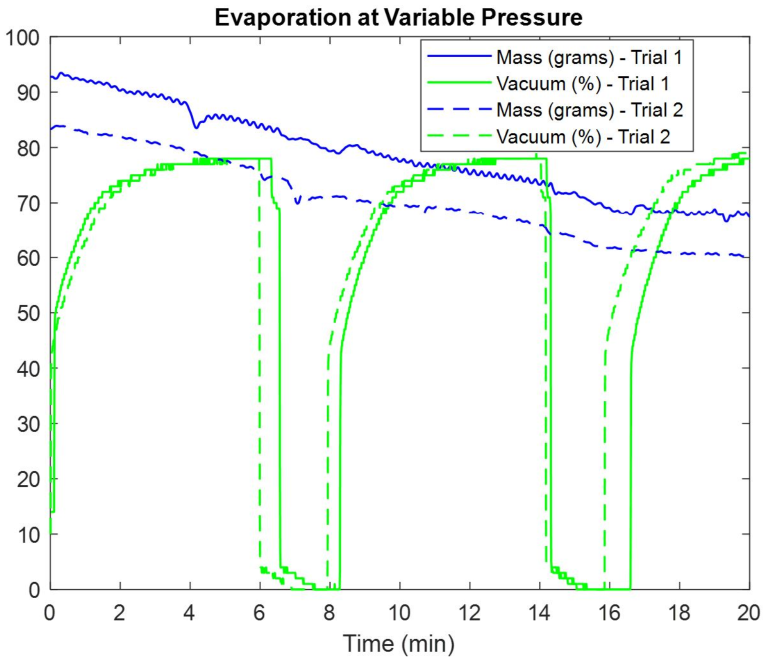

Figure 4.4: Drying properties at 80% pulsed vacuum, 40 gram cloth- VM 6min:2min

4.3 Drying under different conditions

Techniques to speed up drying rate are increasing temperature, decreasing pressure, and changing vacuum modulation. Increasing temperature can provide more energy to the drying process, which helps to evaporate moisture from the textiles more quickly. Decreasing pressure can lower the boiling point of water, allowing it to evaporate at lower temperatures and thus speeding up the drying process. Changing vacuum modulation refers to altering the pressure levels in a pulsating manner, which can enhance the efficiency of moisture removal from the textiles. Comparison of drying methods

4.4 The Effect of Chamber Pressure

Both vacuum drying and pulsed vacuum drying methods reduce drying time compared to normal drying. Figures 4.5 and 4.6 illustrate the drying curves for different drying methods, including vacuum drying, pulsed vacuum drying, and drying under atmospheric pressure. When the bed temperature is set at 60°C and the chamber pressure is maintained at 1 bar under atmospheric conditions, it takes approximately 74 minutes for the textile sample to dry and reach a moisture content of 5When the drying process is carried out under a constant pressure of 0.2 bar, the drying time is decreased by 30%, equivalent to 49 minutes. The technique of pulsed vacuum drying (PVD), utilizing a vacuum modulation (VM) of 6 minutes of operation followed by 1 minute of rest, reduces the drying time by 18% when compared to the constant 0.2 bar vacuum drying method. It is important to mention that the reduced drying time when using PVD is observed at both 60 °C and 80 °C temperatures.

4.5 The Effect of Textile Temperature

In this section, we explore the effects of temperature on the drying kinetics of a 40 grams cotton sample under different conditions, as shown in figures 4.7 and 4.8, also summarized in Table 4.4. It is well-established that temperature plays a crucial role in influencing the rate of water evaporation in drying processes. As we examine the

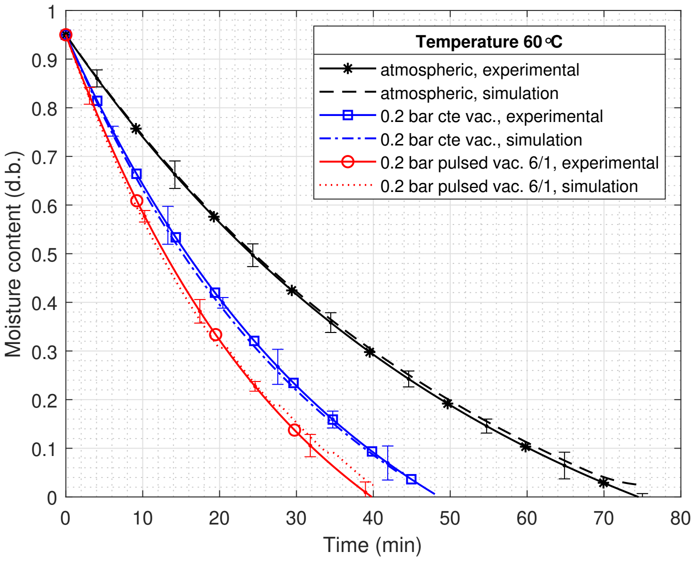

Figure 4.5: Drying curves of 40g textile with bed temperature of 60°C. at different conditions.

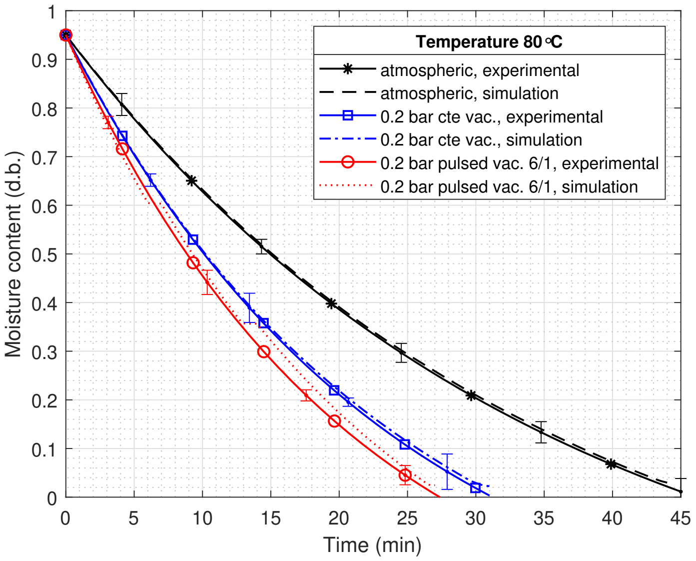

Figure 4.6: Drying curves of 40g textile with bed temperature of 80°C. at different conditions.

experimental results, several notable trends emerge.

First, considering the experiments conducted at a constant chamber pressure of 0.2 bar, we observe that an increase in heating bed temperature from 60°C to 70°C

(Experiments 1 and 4) significantly reduces the total drying time. In Experiment 1, where the temperature was 60°C, the total drying time was 40 minutes, while in Experiment 4, with a temperature of 70°C, the drying time reduced to just 35 minutes. This reduction in drying time can be attributed to the accelerated moisture evaporation at higher temperatures. Similarly, when we compare Experiments 4 and 7, both conducted at 70°C but with different chamber pressures, we notice that the lower pressure (0.2 bar) in Experiment 4 results in a slightly shorter drying time (35 minutes) compared to the higher pressure (1 bar) in Experiment 7 (27 minutes). This underscores the influence of pressure on drying kinetics, with lower pressures favoring faster drying.

Table 4.4: Experimental total drying time for 40g cotton sample under different conditions

Test#	$T_{bed}(^{\circ}C)$	$P_{chamber}$ (bar)	t_v (s)	t_a (s)	τ (s)	t_{total} (min)
1	60	0.2	360	60	33.3	40
2	60	0.2	-	-	37.0	49
3	60	1	-	-	56.8	74
4	70	0.2	360	60	26.6	35
5	70	0.2	-	-	28.6	38
6	70	1	-	-	39.8	52
7	80	0.2	360	60	20.9	27
8	80	0.2	-	-	23.8	31
9	80	1	-	-	35.1	45

Furthermore, as we shift to even higher temperatures (80°C) in Experiments 7, 8, and 9, we consistently observe a notable reduction in the total drying time. The drying time decreases from 27 minutes at 0.2 bar (Experiment 7) to 31 minutes at 0.2 bar (Experiment 8) and further decreases to 45 minutes at 1 bar (Experiment 9). These results clearly highlight the impact of elevated temperatures on expediting the drying process.

In conclusion, the experimental data presented in table 4.4 reaffirms the well-

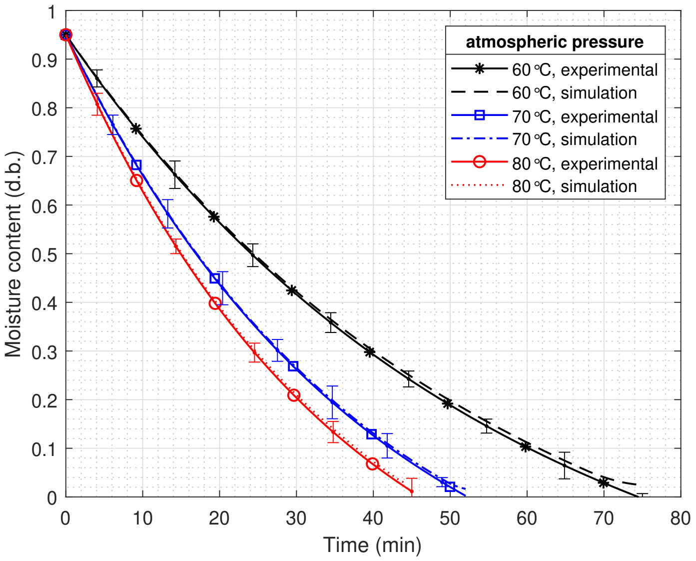

Figure 4.7: Drying curves of 40g textile under atmospheric pressure at different temperatures.

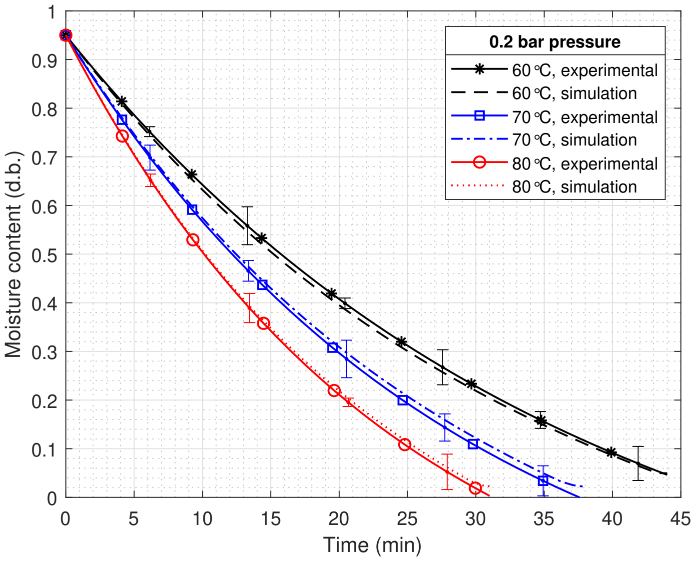

Figure 4.8: Drying curves of 40g textile under 0.2 bar pressure at different temperatures.

established principle that increased temperatures lead to faster drying kinetics. This phenomenon is a critical factor to consider when optimizing drying processes, as it can significantly affect efficiency and throughput in various industrial applications.

Additionally, it underscores the importance of careful temperature control in achieving desired drying outcomes.

4.6 The Effect of Vacuum Modulation

In this section, we investigate the critical factors that affect drying performance within the context of pulsed vacuum drying (PVD). To elucidate the relationship between various parameters and the drying rate, we conducted experiments, the results of which are presented in Table 4.5. Specifically, we focus on the effect of the vacuum phase duration (figures 4.9 and 4.10) and the atmospheric phase duration (figures 4.11 and 4.12), which are integral components of the PVD process.

Table 4.5: Experimental total drying time for 40g cotton sample- effect of vacuum modulation; 60°C bed temperature and 0.2 bar chamber pressure

Test#	$T_{bed}(°C)$	$p_{chamber}$ (bar)	t_v (s)	t_a (s)	τ (s)	t_{total} (min)
10	60	0.2	240	60	29.2	43
1	60	0.2	360	60	30.2	40
11	60	0.2	480	60	32.7	38
12	60	0.2	480	30	35.8	47
13	60	0.2	480	120	32.1	42
2	60	0.2	-	-	37.0	49

The experimental setup, maintained at a heating bed temperature of 60°C and a chamber pressure of 0.2 bar, allowed us to systematically vary the vacuum phase duration (t_v) and the atmospheric phase duration (t_a) while keeping other conditions constant. Upon analyzing the data, several noteworthy trends emerge. Firstly, when we examine the effect of varying the vacuum phase duration, we notice that as t_v increases, there is a slight increase in the total drying time. Experiments 10, 1, and 11, with vacuum durations of 240, 360, and 480 seconds, respectively, exhibit total drying times of 43, 40, and 38 minutes. This suggests that extending the vacuum phase duration marginally impacts the drying process, with longer vacuum durations leading to slightly shorter drying times.

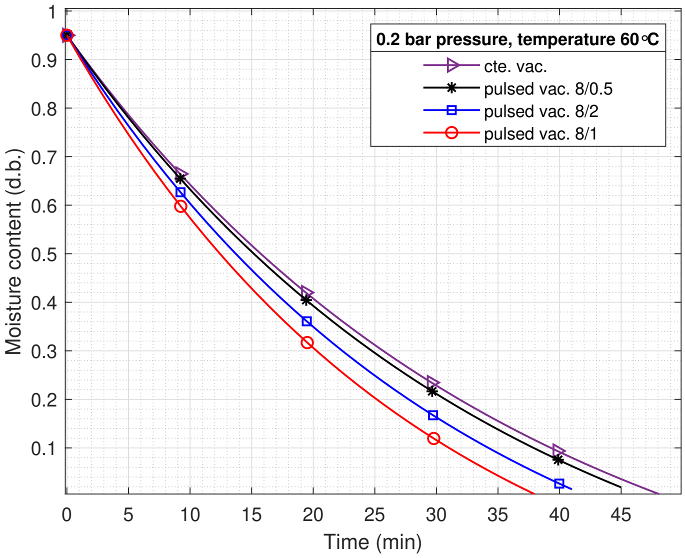

Figure 4.9: Experimental results of drying curve of 40g textile, different atmospheric durations.

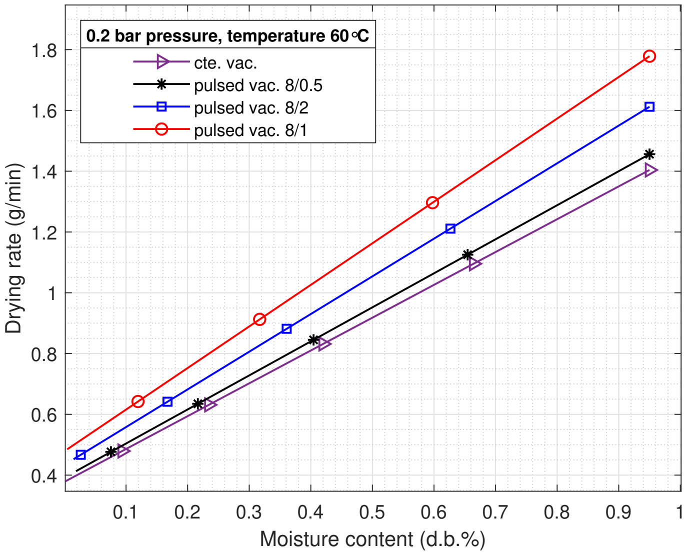

Figure 4.10: Experimental results of drying rate of 40g textile, different atmospheric durations.

Next, we explore the influence of changes in the atmospheric phase duration. As we compare Experiments 12, 13, and 2, where t_a varies between 30, 120, and unspecified (continuous vacuum), we observe that a shorter atmospheric phase duration results in longer total drying times. Experiment 12, with a 30-second atmospheric phase, has a total drying time of 47 minutes, while Experiment 13, with a 120-second atmospheric phase, exhibits a total drying time of 42 minutes. In contrast, Experiment 2, with continuous vacuum, has the longest drying time of 49 minutes.

In conclusion, the results from Table 4.5 provide valuable insights into the effects of vacuum phase duration and atmospheric phase duration on drying performance in PVD. While the influence of vacuum phase duration appears to have a marginal impact on drying times, varying the atmospheric phase duration significantly affects drying rates. These findings underscore the importance of carefully controlling and optimizing the atmospheric phase duration in PVD processes to enhance overall drying performance. The experimental design presented in this study serves as a valuable foundation for further investigations into the interplay of these parameters and their effects on drying kinetics.

The drying curve, often depicted as Moisture Content vs. Time, is a fundamental representation of the drying process. It provides a visual insight into how the moisture content of a material changes over a period of time during drying. This curve typically starts with a high moisture content at the beginning of the process, reflecting the initial state of the material. As time progresses, the moisture content steadily decreases as water evaporates from the material. The shape of the drying curve can vary depending on factors such as temperature, pressure, and airflow. Understanding the drying curve is crucial for assessing the overall progress and efficiency of a drying operation and for determining when the material reaches the desired moisture level.

The drying rate curve shown in figures 4.10 and 4.12, on the other hand, goes beyond the drying curve by providing information about how fast the material is losing moisture at different points in the drying process. It plots the drying rate, typically in units like grams per minute, against time. The drying rate curve often exhibits an initial rapid drying phase, followed by a slower phase as moisture content decreases. The peak of the drying rate curve represents the point at which the material is drying at its maximum rate. Understanding this curve is essential for optimizing drying processes, as it helps identify the most efficient drying conditions

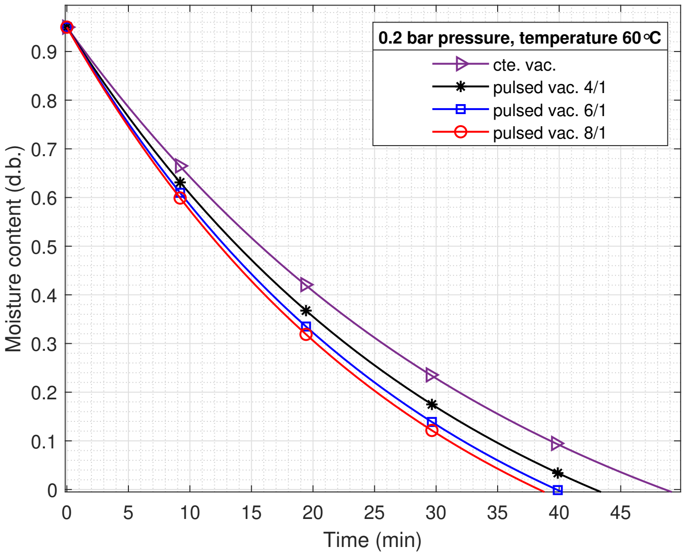

Figure 4.11: Experimental results of drying curves of 40g textile, different vacuum durations.

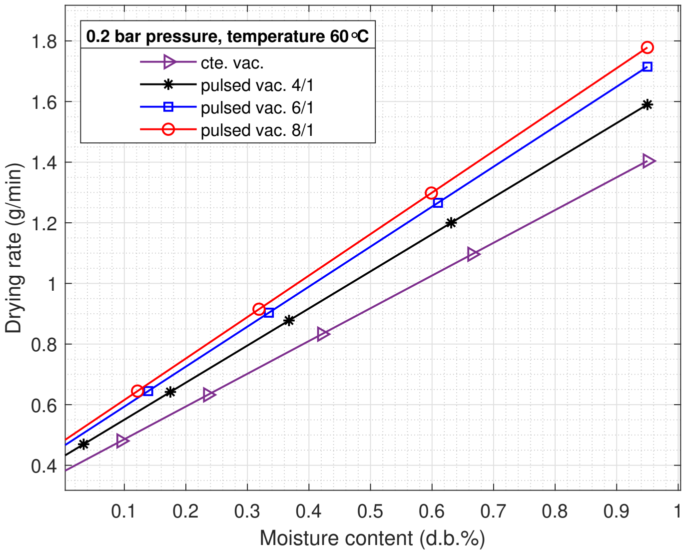

Figure 4.12: Experimental results of drying rate of 40g textile, different vacuum durations.

and allows for better control over drying operations.

Drying curves known as Rate vs. Moisture Content, provides a complementary perspective on the drying process. Instead of time, this curve plots the drying rate against the moisture content of the material. It helps identify how the drying rate changes as the material's moisture content decreases. Typically, this curve shows a gradual decline in drying rate as moisture content decreases, illustrating the diminishing rate of moisture removal as the material approaches its dry state. Understanding this curve aids in pinpointing the critical moisture content levels at which the drying process may need adjustments or where certain drying characteristics, such as the falling-rate period, become prominent. Overall, Drying Rate Curve 2 offers valuable insights into the drying behavior of materials at different stages of the drying process, allowing for more precise control and optimization of drying operations.

4.7 Comparison between Constant Vacuum and Pulsed Vacuum

Pulsed vacuum drying (PVD) achieves a 23% faster reduction to 5% moisture content compared to constant vacuum drying, while maintaining quality. PVD decreases the drying temperature by 20°C, bringing it down from 80 to 60°C, while maintaining the same drying time under atmospheric pressure. indicating a lower energy requirement. Experimental and computational results show that The use of PVD technology increases the speed at which cotton samples dry and reduces the temperatures required for the drying process, indicating improved efficiency compared to constant vacuum drying. The length of the vacuum phase in PVD determines the extent of moisture removal from the material in each cycle, resulting in differences in drying speeds. PVD utilizes pressure pulsation in the drying chamber, which enhances moisture evacuation and improves drying metrics compared to constant vacuum drying. The optimization of vacuum modulation in PVD, including the duration of vacuum and non-vacuum phases, plays a vital role in attaining the fastest overall drying time and increased average drying rates. The overall length of each cycle in PVD plays a crucial role in determining the drying time and efficiency of the process.

4.7.1 Hypothesis on Effects of Vacuum and Pulsed Vacuum

One theory proposes that the disparity in water vapor pressure between the textile sample's surface and the chamber is a critical factor in increasing the rate. As the pressure inside the chamber decreases while undergoing vacuum drying, the partial pressure of water vapor in the chamber also decreases. The decrease in pressure causes the drying rate to rise as the system seeks to achieve a balance in vapor pressure levels between the sample surface and the air in the chamber [29].

Secondly, autovaporization causes an increased drying rate in pulsed vacuum drying with each pressure reduction in the chamber. During each falling pressure stage, the chamber's internal pressure is lower than the partial pressure of water vapor, causing liquid molecules to escape into the air as vapor. This phenomenon contributes to the overall increase in the drying rate [31].

An alternative hypothesis proposes that irreversible adiabatic transformations occur due to temperature variations during instantaneous pressure discharge. These transformations create an imbalanced thermodynamic state that further accelerates the drying process.

The research also takes into account the phenomenon known as the "tunneling effect," which pertains to the movement of moisture from the inner structure of a porous sample to its outer layers. This effect is influenced by pressure variations between the inside and outside of the sample, resulting in channels for moisture to be transported to the surface. This occurrence aids in accelerating the drying process [32].

KMaintaining a constant pressure level results in the formation of a saturated layer of air above the sample, resulting in a decrease in vapor diffusivity. The circulation of air inside the drum also plays a role in the drying rate. In every iteration, the chamber is subjected to blowing and suction, resulting in the generation of turbulence and the circulation of the drying air over the sample. The circulation aids in the replacement of the saturated layer on the sample's surface and enhances the movement of moisture from the textile's outer layer to the internal environment of the drum, thereby reducing the drying time [30].

4.8 *Pulsed Vacuum Drying Optimization*

In this section, we have undertaken a comprehensive grid search analysis to identify the optimal vacuum modulation that yields the highest average drying rate. This set of experiments aimed to determine the most efficient vacuum modulation strategy, which is crucial for optimizing drying processes. It is important to note that all these experiments were conducted under identical initial conditions to ensure a fair comparison.

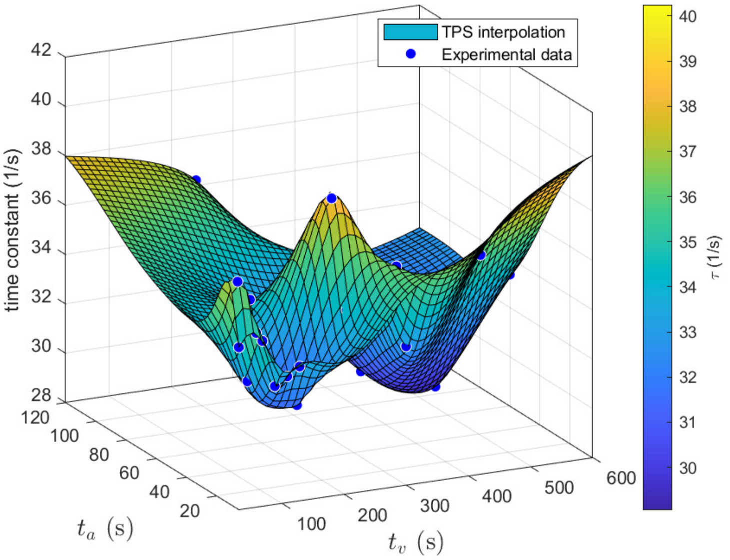

Figure 4.13: The time constant (τ) 3D plot over vacuum atmospheric duration.

These experiments maintained consistent parameters such as heating bed temperature and vacuum chamber pressure for both the vacuum and non-vacuum phases. The only variable that was systematically altered across the experiments was the vacuum modulation. By isolating this parameter as the primary focus of investigation, we sought to pinpoint the vacuum modulation strategy that would result in the fastest total drying time. To visually represent our findings, we have presented 3D plots (figure 4.13) and contour plots (figure 4.14) showcasing the time constant τ as a function of vacuum duration t_v and atmospheric duration ta. These plots provide a clear depiction of the interplay between vacuum modulation parameters and their impact on the drying process. Ultimately, the outcomes of these experiments will significantly contribute to the optimization and enhancement of drying techniques, with the goal of achieving higher drying rates and increased efficiency in various practical applications.

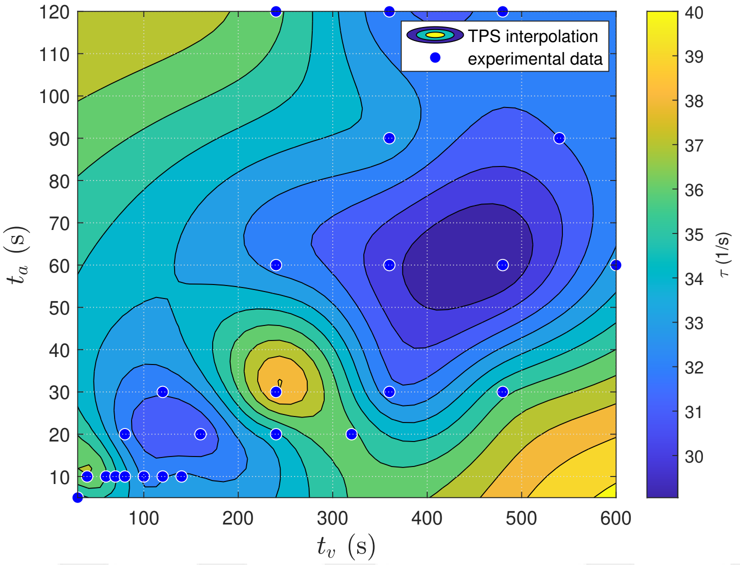

Figure 4.14: The time constant (τ) 2D contour plot over vacuum and atmospheric duration.

4.9 Conventional Dryers and PVD

In our pursuit of evaluating the performance of Pulsed Vacuum Drying (PVD) and Constant Vacuum Drying techniques, we conducted a series of comparative tests with Arçelik's hybrid dryer, which utilizes a combination of heat pump and heater technologies, see figure 4.15. These tests aimed to provide valuable insights into how our innovative drying techniques stack up against commercially available options.

In these comparative experiments, we introduced two new samples (shown in figure 4.17) with an initial moisture content of 60%, a level commonly achieved after the completion of a washing machine cycle. This starting point was chosen to mimic real-world conditions where laundry goes from washing to drying.

Remarkably, the results of these tests demonstrated that Arcelik's hybrid dryer

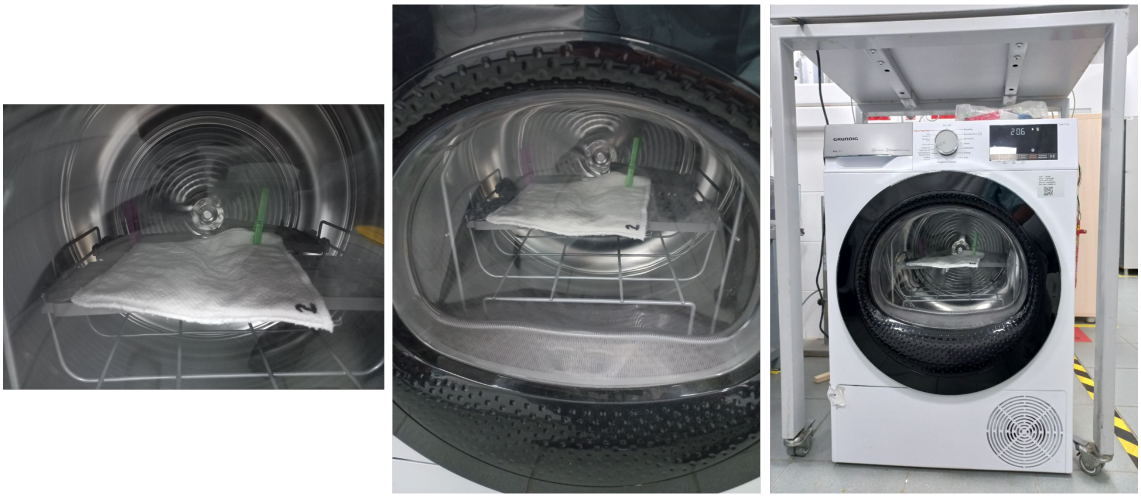

Figure 4.15: Arçelik hybrid HP dryer test setup

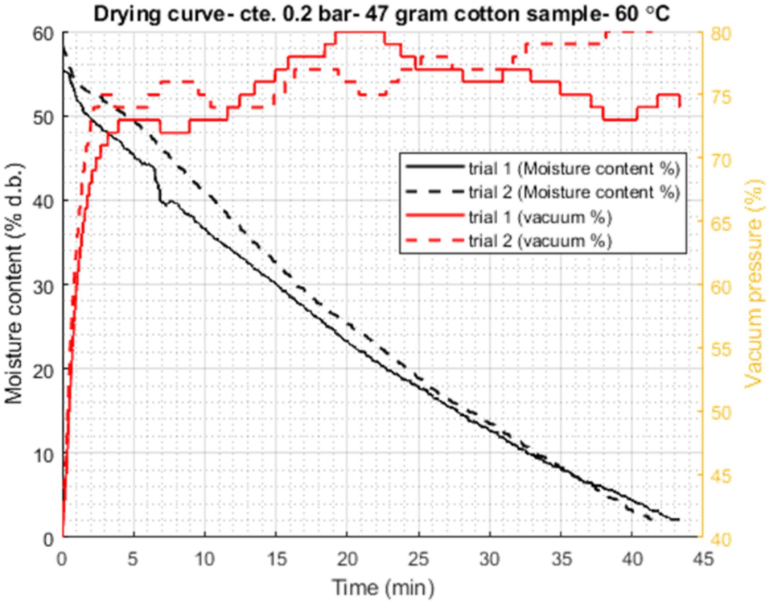

Figure 4.16: Vacuum prototype setup results.

outperformed both our PVD and Constant Vacuum Drying methods in terms of drying rate. The hybrid dryer's ability to combine the efficiency of heat pump technology with the rapid drying capability of a heater yielded superior drying performance.

These findings underscore the importance of not only developing innovative drying techniques but also benchmarking them against existing commercial solutions.

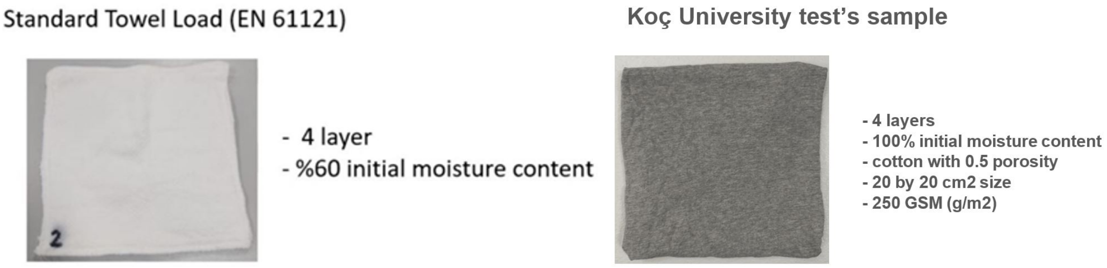

Figure 4.17: Sample prepared by Arçelik team for Çayırova tests and Koç University test's sample.

Table 4.6: Çayırova and Koç University test results- Table 1

Notes	Temp	Pressure	Sample weight (g)	Water weight (g)	Moisture content	Total time (min)	Mean rate (g/min)
Arçelik sample	60	cte 0.2 bar	47	28	60	40	0.7
Arçelik sample	60	cte 0.2 bar	47	28	60	43	0.65
Koç sample Previous results	60	cte 0.2 bar	40	40	100	49	0.81
Arçelik sample Hybrid system	50	Arçelik dryer	47	28	60	30	0.93

While our research has provided valuable insights and potential avenues for improvement in drying processes, it is clear that Arçelik's hybrid dryer, with its advanced technology and optimized design, currently offers a higher drying rate, making it a compelling choice for consumers seeking efficient and effective laundry drying solutions. This comparative approach serves as a valuable reference point for future advancements in drying technology. In the context of drying processes, it is essential to note that the inlet air temperature can vary significantly between different dryer types. In the case of both hybrid heat pump (HP) dryers and standard HP dryers, the inlet air temperature follows distinct patterns compared to the vacuum prototype setup, where a constant temperature of 60°C was maintained, see figure 4.16.

In comparing the performance metrics of different drying processes, shown in tables 4.9 and 4.9, we observe distinctive characteristics in both temperature and drying rate. The Heat Pump Dryer achieves an average textile temperature of 39°C with a drying time of 45 minutes, resulting in a drying rate of 0.61 g/min. The Constant Vacuum process at 0.1 bar elevates the temperature to 59°C while maintaining the same drying time, resulting in a slightly higher drying rate of 0.63 g/min. The Hybrid Heat Pump Dryer strikes a balance between temperature and time, achieving a textile temperature of 50°C, a reduced drying time of 35 minutes, and an enhanced drying rate of 0.80 g/min. Similarly, the Pulse Vacuum process at 0.1 bar mirrors the Hybrid Heat Pump performance in terms of temperature, drying time, and drying rate. Notably, in both heat pump and hybrid heat pump scenarios, temperatures are lower compared to constant vacuum conditions, despite achieving comparable drying rates. This suggests that the hybrid approach optimizes the drying process by efficiently managing temperature, time, and drying rate.

Table 4.7: Çayırova and Koç University test results- Table 2

Drying Process	Average Textile Temperature	Drying Time	Drying Rate
Units	(°C)	(min)	(g/min)
Heat Pump Dryer	39	45	0,61
Constant Vacuum 0.1 bar	59	45	0,63
Hybrid Heat Pump Dryer	50	35	0,80
Pulse Vacuum 0.1 bar	59	35	0,80

In hybrid HP dryers, the inlet air temperature undergoes variations during the drying cycle. Initially, the air temperature may be lower, but after approximately 15 minutes into the drying process, it begins to rise and eventually reaches 60°C for a duration of around 15 minutes. This controlled variation in temperature is designed to optimize the drying process for different materials and ensure efficient moisture removal. On the other hand, in standard HP dryers, the inlet air temperature typically starts at a lower value, such as 20°C, and gradually increases over time. It may take approximately 45 minutes for the inlet air temperature to reach a peak of around 55°C, see figure 4.18. This gradual temperature rise is another strategy to achieve efficient and uniform drying while preventing overheating or over-

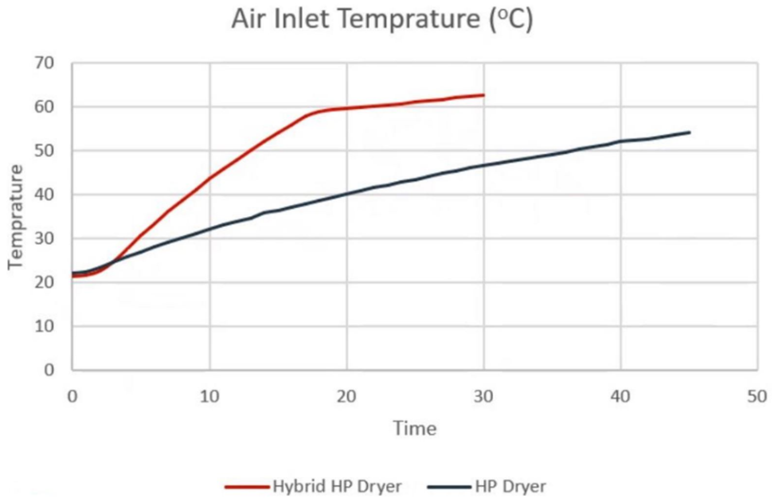

Figure 4.18: Inlet air temperatures of Arçelik dryers

drying of the materials being processed. These variations in inlet air temperature profiles demonstrate the flexibility and adaptability of HP dryers to different drying requirements and materials. By carefully controlling the temperature dynamics, these dryers can achieve optimal drying results while conserving energy and ensuring product quality.

Chapter 5

CONCLUSION

5.1 Overview

In summary, the investigation into vacuum-assisted drying methods as a novel textile drying technique has yielded encouraging results, showcasing its potential to revolutionize the textile drying industry. Through a series of comparative experiments between atmospheric drying, constant vacuum drying, and pulsed vacuum drying, PVD demonstrated a notable reduction of up to 23% in total drying time when compared to constant vacuum drying. Notably, PVD not only enhances the average drying rate but also performs at lower temperatures, ensuring the preservation of fabric quality. The experiments highlighted the significant influence of temperature, chamber pressure, and vacuum modulation on the drying kinetics during PVD. Higher temperatures accelerated drying, emphasizing the role of increased kinetic energy. Moreover, longer vacuum phases were found to boost moisture removal. Optimizing sample temperature, chamber pressure, and the duration of vacuum and non-vacuum phases appeared as critical factors for enhancing drying rates and shortening overall drying times.

Our main goal in this work has been to use mathematical models and experiments to understand the principles of vacuum drying. We now have a thorough knowledge of the critical role suction plays in accelerating the drying process thanks to this dual strategy. Through exploration of the complexities of vacuum-assisted drying, we have learned more about how important variables like temperature, pressure, and modulation periods interact. Although our results provide insightful insights into the underlying mechanisms, it is important to recognize the possibility of further research in the area of scalability. To facilitate the wider use of vacuum-assisted drying, it is still interesting to investigate the practicality and effectiveness of technologies on an industrial scale.

Despite these advances, it is essential to acknowledge the existing challenges associated with PVD. The manufacturing complexity and costs associated with the construction of vacuum chambers pose practical limitations. Additionally, identifying an efficient vacuum creation mechanism that can handle moisture remains a challenge. The study revealed that, while centrifugal vacuum pumps may not be feasible to achieve the desired vacuum levels, pneumatic vacuum generators, utilizing a pressurized air supply, showed practical functionality in an experimental scale setup. Further investigations into the energy efficiency and scalability of pneumatic vacuum generators could open new opportunities for applying PVD in industrial settings or home appliances.

5.2 Future Work

Building on the groundwork this study created, several interesting directions for further investigation are revealed. Above all, it is a compelling opportunity to extend the existing numerical model to include characteristics of the textile solid phase. With this development, a more thorough understanding of the complex dynamics involved in vacuum-assisted drying would be possible. Additionally, investigating the scalability of the developed methods to an industrial setting is a crucial next step. Wider use might be facilitated by addressing issues with vacuum chamber manufacturing complexity and costs. Another important topic for research is investigating alternate vacuum generation mechanisms, especially ones that can handle moisture well and use less energy. Vacuum drying procedures may be more versatile and applicable if vacuum modulation strategies were further improved and optimized while taking into account various textile types. These next projects might progress the industry and help textile drying methods evolve in a way that is both efficient and sustainable.

BIBLIOGRAPHY

[1] Ayyoub M. Momen, Viral K. Patel, Kyle R. Gluesenkamp, Donald Erdman, James Kiggans, and Geoffrey Ormston. Fabric properties and electric efficiency limits of mechanical moisture extraction from fabrics. *Drying Technology*, 0(0):1–17, 2021.

[2] A Farid Ayad, Hamed M Abdalla, and A Abou El-Azm Aly. Effect of semi-open impeller side clearance on the centrifugal pump performance using cfd. *Aerospace Science and Technology*, 47:247–255, 2015.

[3] Dwight F Windenburg and Charles Trilling. Collapse by instability of thin cylindrical shells under external pressure. *Transactions of the American Society of Mechanical Engineers*, 56(8):819–825, 1934.

[4] Weerachai Kaensup, Surachate Chutima, and Somchai Wongwises. Experimental study on drying of chilli in a combined microwave-vacuum-rotary drum dryer. *Drying Technology*, 20(10):2067–2079, 2002.

[5] Ibrahim Dincer Canan Acar and Arun Mujumdar. A comprehensive review of recent advances in renewable-based drying technologies for a sustainable future. *Drying Technology*, 40(6):1029–1050, 2022.

[6] Kyle R. Gluesenkamp, Viral K. Patel, and Ayyoub M. Momen. Efficiency limits of evaporative fabric drying methods. *Drying Technology*, 39(1):104–124, 2021.

[7] Panna Lal Singh. Silk cocoon drying in forced convection type solar dryer. *Applied Energy*, 88(5):1720–1726, 2011.

[8] R Tu. APPLIED Utilization of waste-heat recovery in textile drying. *Applied Energy*, 79:41–49, 2004.

[9] Viral K. Patel, Kyle R. Gluesenkamp, Dakota Goodman, and Anthony Gehl. Experimental evaluation and thermodynamic system modeling of thermoelectric heat pump clothes dryer. *Applied Energy*, 217(February):221–232, 2018.

[10] Lena Stawreberg and Lars Nilsson. Potential energy savings made by using a specific control strategy when tumble drying small loads. *Applied Energy*, 102:484–491, 2013.

[11] Hong Wei Xiao, Chang Le Pang, Li Hong Wang, Jun Wen Bai, Wen Xia Yang, and Zhen Jiang Gao. Drying kinetics and quality of Monukka seedless grapes dried in an air-impingement jet dryer. *Biosystems Engineering*, 105(2):233–240, 2010.

[12] Rasaq O Lamidi, L Jiang, Pankaj B Pathare, Y D Wang, and A P Roskilly. Recent advances in sustainable drying of agricultural produce : A review. *Applied Energy*, 233-234(September 2018):367–385, 2019.

[13] Yucen Xie, Zhenjiang Gao, Yanhong Liu, and Hongwei Xiao. Pulsed vacuum drying of rhizoma dioscoreae slices. *Lwt*, 80:237–249, 2017.

[14] Hao Yu Ju, Chung Lim Law, Xiao Ming Fang, Hong Wei Xiao, Yan Hong Liu, and Zhen Jiang Gao. Drying kinetics and evolution of the sample's core temperature and moisture distribution of yam slices (Dioscorea alata L.) during convective hot-air drying. *Drying Technology*, 34(11):1297–1306, 2016.

[15] Bachir El Fil and Srinivas Garimella. The state of the art in energy saving techniques for garment/textile drying. *Drying Technology*, 40(11):2235–2250, 2022.

[16] Viral K. Patel Kyle R. Gluesenkamp and Ayyoub M. Momen. Efficiency limits of evaporative fabric drying methods. *Drying Technology*, 39(1):104–124, 2020.

[17] Abhay Menon, Valentina Stojceska, and Savvas A. Tassou. A systematic review on the recent advances of the energy efficiency improvements in non-

conventional food drying technologies. *Trends in Food Science and Technology*, 100:67–76, 2020.

[18] Ayyoub M. Momen, Viral K. Pate, Kyle R. Gluesenkamp, Donald Erdman III, James Kiggans Jr, and Geoffrey Ormston. Fabric properties and electric efficiency limits of mechanical moisture extraction from fabrics. *Drying Technology*, 40(15):3160–3176, 2022.

[19] Yonggao Yin, Baojun Zheng, Can Yang, and Xiaosong Zhang. A proposed compressed air drying method using pressurized liquid desiccant and experimental verification. *Applied Energy*, 141:80–89, 2015.

[20] Isaac Duah Boateng, Desy Anggraini Soetanto, Xiao-Ming Yang, Cunshan Zhou, Firibu Kwesi Saalia, and Fengnan Li. Effect of pulsed-vacuum, hot-air, infrared, and freeze-drying on drying kinetics, energy efficiency, and physicochemical properties of ginkgo biloba l. seed. *Journal of Food Process Engineering*, 44(4):e13655, 2021.

[21] Ali Motevali, Saeid Minaei, Ahmad Banakar, Barat Ghobadian, and Mohammad Hadi Khoshtaghaza. Comparison of energy parameters in various dryers. *Energy Conversion and Management*, 87:711–725, 2014.

[22] Abhay Menon, Valentina Stojceska, and Savvas A. Tassou. A systematic review on the recent advances of the energy efficiency improvements in non-conventional food drying technologies. *Trends in Food Science and Technology*, 100(June 2019):67–76, 2020.

[23] William E Asher and Brian Fricke. Experimental Drying Characteristics Of Fabrics Under Vacuum. International Refrigeration and Air Conditioning Conference 2021, 2021.

[24] S. K. Giri and Suresh Prasad. Drying kinetics and rehydration characteristics of microwave-vacuum and convective hot-air dried mushrooms. *Journal of Food Engineering*, 78(2):512–521, 2007.

[25] Zi Liang Liu, Zi Yu Wei, Sriram K. Vidyarthi, Zhongli Pan, Magdalena Zielinska, Li Zhen Deng, Qing Hui Wang, Qing Wei, and Hong Wei Xiao. Pulsed vacuum drying of kiwifruit slices and drying process optimization based on artificial neural network. *Drying Technology*, 39(3):405–417, 2020.

[26] Santiago Plata, William Vicente, Martín Salinas-Vazquez, and Leonardo Urbiola. Analysis of the kinetic parameters of clothes drying in an electric vented dryer. Part I: Validation of a model and influence of power. *Drying Technology*, 40(16):3631–3647, 2022.

[27] Jian Lyu, Jinfeng Bi, Fengzhao Wang, Xin Jin, Xinye Wu, and Jin Xie. Recent developments and trends of instant controlled pressure drop drying-a review. *Drying Technology*, 39(11):1704–1719, 2021.

[28] Dalong Jiang, Hongwei Xiao, Magdalena Zielinska, Guangfei Zhu, Tianyu Bai, and Zhian Zheng. Effect of pulsed vacuum drying on drying kinetics and quality of roots of Panax notoginseng (Burk.) F. H. Chen (Araliaceae). *Drying Technology*, 39(16):2234–2251, 2021.

[29] H. Rakotozafy, N. Louka, M. Thérisod, H. Thérisod, and K. Allaf. Drying of baker's yeast by a new method: Dehydration by Successive Pressure Drops (DDS). Effect on cell survival and enzymatic activities. *Drying Technology*, 18(10):2253–2271, 2000.

[30] S. A. Rezzoug, Z. Maache-Rezzoug, J. Mazoyer, M. Jeannin, and K. Allaf. Effect of instantaneous controlled pressure drop process on the hydration capacity of scleroglucan: Optimisation of operating conditions by response surface methodology. *Carbohydrate Polymers*, 42(1):73–84, 2000.

[31] E. A. Sanya, S. A. Rezzoug, and K. Allaf. A new method for drying waterlogged wooden artefacts: Comparison of cyclical pressure drops with conventional methods. *Chemical Engineering Research and Design*, 81(9):1243–1249, 2003.

[32] K. J. Chua and S. K. Chou. On the experimental study of a pressure regulatory system for bioproducts dehydration. *Journal of Food Engineering*, 62(2):151–158, 2004.

[33] Wafa Hajji, Sihem Bellagha, Carmen Téllez-Pérez, Sabah Mounir, Mohamed Salah Negm, Tamara Allaf, Victor Lefrancois, Colette Besombes, Arun S. Mujumdar, and Karim Allaf. Coupling interval hyper-active drying (ihad) with instant controlled pressure drop (d.i.c.) to define new swell-drying processes. *Drying Technology*, 0(0):1–15, 2023.

[34] Weipeng Zhang, Zhongli Pan, Hongwei Xiao, Zhian Zheng, Chang Chen, and Zhenjiang Gao. Pulsed vacuum drying (PVD) technology improves drying efficiency and quality of Poria cubes. *Drying Technology*, 36(8):908–921, 2018.

[35] Long Xie, Arun S. Mujumdar, Xiao Ming Fang, Jun Wang, Jian Wu Dai, Zhi Long Du, Hong Wei Xiao, Yanhong Liu, and Zhen Jiang Gao. Far-infrared radiation heating assisted pulsed vacuum drying (FIR-PVD) of wolfberry (Lycium barbarum L.): Effects on drying kinetics and quality attributes. *Food and Bioproducts Processing*, 102:320–331, 2017.

[36] Lei Tan, Baoshan Zhu, Shuliang Cao, Hao Bing, and Yuming Wang. Influence of blade wrap angle on centrifugal pump performance by numerical and experimental study. *Chinese journal of mechanical engineering*, 27(1):171–177, 2014.

[37] Ji-Gu Lee and Youn-Jea Kim. Effect of the impeller discharge angle on the performance of a spurt vacuum pump. *Applied Science and Convergenec Technology*, 26(1):1–5, 2017.

[38] Hongchang Ding, Zikang Li, Xiaobin Gong, and Maoshun Li. The influence of blade outlet angle on the performance of centrifugal pump with high specific speed. *Vacuum*, 159:239–246, 2019.

[39] Lei Tan, Shuliang Cao, Yuming Wang, and Baoshan Zhu. Direct and inverse iterative design method for centrifugal pump impellers. *Proceedings of the Institution of Mechanical Engineers, Part A: Journal of power and energy*, 226(6):764–775, 2012.

[40] Gamal RH Abo Elyamin, Magdy A Bassily, Khalil Y Khalil, and Mohamed Sh Gomaa. Effect of impeller blades number on the performance of a centrifugal pump. *Alexandria Engineering Journal*, 58(1):39–48, 2019.

[41] L. Houlin, W. Yong, Y. Shouqi, T. Minggao, and W. Kai. Effects of blade number on characteristics of centrifugal pumps. *Chinese Journal of Mechanical Engineering*, 23:1–6, 2010. cited By 6.

[42] B. Jafarzadeh, A. Hajari, M.M. Alishahi, and M.H. Akbari. The flow simulation of a low-specific-speed high-speed centrifugal pump. *Applied Mathematical Modelling*, 35(1):242–249, 2011.

[43] Mark W Hilburger. Buckling of thin-walled circular cylinders. Technical report, 2020.

[44] C. de Paor, D. Kelliher, K. Cronin, W.M.D. Wright, and S.G. McSweeney. Prediction of vacuum-induced buckling pressures of thin-walled cylinders. *Thin-Walled Structures*, 55:1–10, 2012.

[45] James P Peterson and James Kent Anderson. *Bending tests of large-diameter ring-stiffened corrugated cylinders*, volume 3336. National Aeronautics and Space Administration, 1966.

[46] Howard G Allen and Philip Stanley Bulson. *Background to buckling*. Number Monograph. 1980.

[47] Lisa Yen Wen Chua, Bee Lin Chua, Adam Figiel, Chien Hwa Chong, Aneta Wojdyło, Antoni Szumny, and Krzysztof Lech. Characterisation of the convective hot-air drying and vacuum microwave drying of cassia alata: Antioxidant

activity, essential oil volatile composition and quality studies. *Molecules*, 24(8), 2019.

[48] Jia ao Dai and Yong fa Diao. Numerical analysis of transient coupled heat and moisture transfer in textile drying with porous relative impact jet. *Applied Thermal Engineering*, 212:118613, 2022.

[49] Marcello Murru, Giovanni Giorgio, Sara Montomoli, Francois Ricard, and Frantisek Stepanek. Model-based scale-up of vacuum contact drying of pharmaceutical compounds. *Chemical Engineering Science*, 66(21):5045–5054, 2011.

[50] A. J.D. Lambert, F. P.M. Spruit, and J. Claus. Modelling as a tool for evaluating the effects of energy-saving measures. Case study: A tumbler drier. *Applied Energy*, 38(1):33–47, 1991.

[51] J. Deans. The modelling of a domestic tumbler dryer. *Applied Thermal Engineering*, 21(9):977–990, 2001.

[52] Anwen Zhao, Xiaoting Rui, Bao Rong, and Guoping Wang. Conjugate modeling of flow and simultaneous heat and mass transfer in convective drying of porous substances. *Applied Thermal Engineering*, 199:117571, 2021.

[53] M. Kohout, A.P. Collier, and F. Štěpánek. Effective thermal conductivity of wet particle assemblies. *International Journal of Heat and Mass Transfer*, 47(25):5565–5574, 2004.